Politecnico di Torino

ScuDo
Scuola di Dottorato ~ Doctoral School
WHAT YOU ARE, TAKES YOU FAR

Doctoral Dissertation

Doctoral Program in Mechanical Engineering (35th Cycle)

Ultrasonic Tensile Test Method for Brittle Materials

Ph.D. Thesis

By

Ana Paula Pagnoncelli

Supervisors:
Prof. Lorenzo Peroni
Prof. Davide Salvatore Paolino

Coordinator:
Prof. Luca Goglio

Politecnico di Torino

2023

Acknowledgements

First and foremost, I would like to thank my supervisors, prof. Lorenzo Peroni and prof. Davide Salvatore Paolino, for granting me the possibility of pursuing this PhD program, as well as the coordinator, prof. Luca Goglio.

Special thanks to all who supported me in any way through technical discussions, experimental and numerical setup, and data analysis: Lorenzo Peroni, Davide Salvatore Paolino, Andrea Tridello, Martina Scapin, Carlo Boursier Niutta, and Alberto Morena.

The research used the equipment of J-Tech and DYNLab laboratories at Politecnico di Torino co-funded by POR FESR Piemonte 2014-2020.

Abstract

The difficulties encountered in mechanical testing of brittle materials create the need of developing new procedures to improve the characterization and complement the experimental information on them, which is necessary to increase components design efficiency and reliability. To meet this need, the ultrasonic tensile test was developed, widening the application of the ultrasonic testing machine employed in very high cycle fatigue tests, adapting the experimental control and data acquisition system to cause material failure in less than $200\ cycles$, allowing the acquisition of tensile strength data on brittle materials while avoiding fatigue damage.

The ultrasonic tensile test was shown to be capable of estimating the obtained ultimate strength values to those of a quasi-static test, while eliminating issues caused by mechanical fixtures and tensile testing machine alignment, also allowing a considerable increase in material risk-volume when compared to traditional test methods. Evidence that fatigue failure was indeed avoided was collected through experimental procedures that allow the analysis of facture surfaces and internal defects. The internal defect analysis, through micro-computed tomography, also allowed the definition of criteria to identify the critical defect size in each specimen, as well as general characterization of the defects population.

The ultrasonic tensile test was numerically modeled, with the specimen geometry, test parameters, and the measured displacements being applied to find the optimum material model and properties that best describe its behavior. The optimized numerical model allowed the calculation of the specimen failure strength, which could then be correlated to its critical defect size in the form of empirically formulated stress intensity factors.

The described methodology was successfully implemented through two brittle materials: alumina 99.5% and graphite R4550. Alumina specimens all failed in at most $100\ cycles$, showing a large scatter of fracture strengths, ranging from $79.5\ MPa$ to $322.6\ MPa$, as calculated from an optimized linear-elastic material model, whose elastic modulus was $371.2\ GPa$. The strengths being associated with a wider variety of imperfection types and sizes, broadly classified into pores, cracks and inclusions, with critical sizes ranging from $92\ \mu m$ to $3443\ \mu m$, consequently generating a rather complex empirical formulation for stress intensity factors.

Meanwhile, graphite specimens, having withstood at most $140\ cycles$, showed only pores as defects, with critical sizes ranging from $82\ \mu m$ to $112\ \mu m$, and fracture strengths from

$45.3\ MPa$ to $59.6\ MPa$, generating a simpler empirical formulation for stress intensity factors than that of alumina. However, graphite experimental behavior required a nonlinear material model for optimization, with slightly different elastic moduli in tension and compression, being $11.31\ GPa$ and $11.42\ GPa$, respectively, and added viscoelastic behavior, with shear relaxation modulus of $1.83\ GPa$ and decay constant of $31.38\ ms^{-1}$. The methodology application to alumina and graphite, which present pronounced differences in behavior and results, allowed its validation as a new experimental-based procedure to collect additional data on brittle materials.

Contents

List of Figures

List of Tables

Chapter 1

1. Introduction

Brittle behavior is a terminology that can be used to define a wide variety of materials, like ceramics – the most frequently associated with it –, polymers, composites, glasses, minerals, and metals. They are usually associated with linear-elastic behavior, which is not always the case, since some of them can exhibit viscoelasticity [1], hyperelasticity [2], or even a low degree of plasticity [3], even though the latter is usually incorporated into numerical and analytical material models that emulate ductile materials.

Virtually any material class contains at least a few members that can be classified as brittle and many others that start exhibiting brittle behavior when under certain conditions, such as below their respective ductile-brittle transition temperature [4]. Therefore, the best way to define a brittle material is as those that are capable of absorbing very little strain energy, either in the form of reversible strain (linear-elastic, viscoelastic, hyperelastic) or in the form of irreversible strain (plasticity, delamination, debonding).

These materials lack in capacity to withstand strain often causes an almost instantaneous crack propagation at the failure moment, also called catastrophic failure, which is characterized for not showing indications that the material is approaching its mechanical limit beforehand – such as large elastic strains, elastic-plastic behavior, and other visible or measurable signs of crack growth and propagation. For this reason, a reliable knowledge of the strength these materials can resist is necessary before employing them in any type of structural application.

However, experimental data on mechanical strength of brittle materials shows very wide scatters of data even for the same specimen geometry, risk-volume, and testing configuration. While the theoretical tensile strength ceiling is the one needed to break between their atoms, the presence of material flaws governs their mechanical resistance. Since these flaws – internal pores, inclusions, and cracks, as well as surface irregularities – are impossible to be eliminated even by improving the production process and the purity of the raw components, and they are sources of stress concentration, and possible origins of crack propagation, the experimental nominal strength is always considerably lower than its theoretical ceiling. Consequently, the predictability of the mechanical resistance of a brittle material is directly influenced by the knowledge of its intrinsic flaws, i.e., the discontinuities that are potential weakest links in the material. Indeed, today a common occurrence is to spend more time and resources studying the resulting internal defects originating from a manufacturing process so that the component can be designed considering those defects, rather than improving the material fabrication process itself.

When concerning brittle materials, the knowledge of their respective intrinsic defects is even more crucial to the design of structural components than for ductile materials, since stress concentration within a material that is unable to absorb any significant amount of strain energy means that the local high stress causes the crack to propagate. This mechanism is directly related to fracture toughness, which is generally very low among brittle materials. For this reason, experimental nominal strength of brittle materials should be researched in concomitancy with methods that allow the characterization of the intrinsic defects.

By correlating nominal strength to a quantity such as the size of the critical defect – i.e., the defect that likely generated the largest local stress in the specimen, initiating the fracture – the material can be characterized in a way that can be more reliably applied into the design of the final component. This objective should be accomplished by fulfilling three tasks: i) establishing an experimental procedure to obtain the nominal strength, ii) developing a criterion to consider the presence of internal defects, and, finally, iii) relating the two quantities through a method that can be applied to the design of components. These three tasks will be further detailed in the next sections.

1.1. Nominal Strength of Brittle Materials

The two most common issues encountered during mechanical testing of brittle materials are fixture failures, which produce invalid experimental results, and testing machine alignment, that can, for instance, generate large undesired bending stresses on tensile tests. These two issues prevent the proper application of many test methods. Consequently, most methods performed on brittle materials are designed to avoid the need for mechanical fixtures or a very precise testing machine alignment.

The first step towards establishing an experimental procedure to measure the material strength is to understand the issues and limitations brought by their nature and properties to test methods in general. As previously explained, brittle materials can easily produce a large scatter of experimental nominal strength data, directly related to the randomness of the defect population and its characteristics. Nevertheless, it is still possible to consider a seemingly unreliable quantity such as nominal strength in components design provided it is used in conjunction with an appropriate statistical method that accounts for the presence of discontinuities, such as size effect models, or even an experimental method capable of directly measuring the material defects, like 3D x-ray imaging technology.

However, even if a method is used to correlate the presence of intrinsic defects to each specimen nominal strength, experimentally measuring the latter is also a challenge. Traditional tensile test standards for brittle materials tend to have strict requirements, which, despite being met, do not guarantee reliable results. Test samples are often discarded for breaking near the testing machine mechanical fixtures, like in Fig. 1.1, which shows examples of specimens used in split Hopkinson tension bar tests that failed near the thread, causing the measurements to be disregarded.

Figure 1.1 Direct split Hopkinson tension bar test specimens in silicon carbide and molybdenum.

Another common issue found during these tests is the misalignment of the testing machine, which produces unwanted multiaxial stress states on the specimen. Indeed, tensile test standards in general mention a maximum misalignment level that can be tolerated, measured by strain gauges placed on a dummy specimen used to calibrate the machine [5]. Since brittle materials can withstand very small strains, it is reasonable to assume that the maximum allowable misalignment is also very small, and depending on the specimen defects and geometry, could produce invalid results despite the standards being respected.

Moreover, some materials, especially technical ceramics, have such high mechanical resistance, that the specimen cross-section needs to be small enough so that tensile testing machines can cause its failure. Materials like silicon nitride and zirconia reach mechanical strengths on the order of $1\ GPa$, according to three and four-point bending tests. Therefore, if that would also be the case for tensile tests, a testing machine of over $80\ kN$ of capacity would already be needed to test specimens with a circular cross-section of $10\ mm$ of diameter. Additionally, the mechanical fixtures of the machine would still be an issue, that might be mitigated by a variable cross-section, proportionally larger at the fixtures, which would, however, considerably increase the fabrication costs of the specimens without facilitating the testing machine alignment process, and without guaranteeing the elimination of fixture failures.

Therefore, three and four-point bending tests appear as the most recurring methods for testing brittle materials in the literature, allowing variations in the specimens geometries, for instance bars, plates, rods, tubular samples, and the addition of notches [6-12]. Moreover, these tests can be applied to most brittle materials, e.g., glass, concrete, advanced ceramics, graphene, etc. Similarly, other types of bending tests have the advantage of avoiding fixtures and alignment issues, for instance ASTM C1550, ring-on-ring, and their variations [13,14], which, despite also allowing testing of most brittle materials and specimens geometries of relatively simple fabrication (disc geometry), generate multiaxial stress states on the material that need to accounted for during strength estimation.

Meanwhile, other experimental procedures eliminate the need of grips and alignment by applying a compressive load aiming to generate multiaxial stress due to the specimen's particular geometry. This is the case of the Brazilian splitting test [15] and other methods that use a similar concept, relying on relatively simple geometries, like discs, spheres and rings [16-18], as well as more peculiar shapes [19-21]. Less traditional test methods include wedge splitting [22], the ring hoop tension [23], the Iosipescu method [24] (usually employed to characterize shear strain behavior of composite materials), and a tensile testing apparatus for tubular specimens [25]. Additionally, many of the previously mentioned test configurations were also presented in the literature employing different strain rates [26-29], including impact tests on split Hopkinson pressure bar [30,31].

However, generally, the above-mentioned test methods present two limitations: they often require the calculation of the material tensile strength from multiaxial stress states, and they have relatively low loaded volume (risk-volume), which corresponds to the material volume subjected to a stress close to the maximum applied stress. The strength of brittle materials is strongly affected by defects distribution and size [32,33], with large defects being statistically more likely to occur the larger the material volume, causing the consequent decrease of the experimental strength of specimens having larger loaded volumes [34-36]. Hence the importance of testing specimens of loaded volumes as large as possible, so as to evaluate the material strength even in worst case scenarios.

Furthermore, the high susceptibility to defects encountered in brittle materials implies that the most critical type of stress for these materials is the tensile stress that induces crack opening [37], following Irwin's definition of fracture mode I [38]. To avoid the need of indirectly estimating the material tensile strength from the multiaxial states encountered in the previously mentioned test methods, many authors have proposed procedures to directly measure a brittle material mechanical tensile behavior. However, such methods usually require specific specimen geometries [39], are often only applicable to low strength materials [40,41], or still result in very small risk-volumes when high strength materials are tested [42-45].

Therefore, to improve brittle materials mechanical experimental data, it is important to develop new testing procedures that can cover at least some of the shortcomings of the existent methods. This is why the conception and validation of the Ultrasonic Tensile (UST) test, presented in this work, represents an important contribution to researching brittle materials, since, as detailed later on, its main advantages are completely avoiding alignment and mechanical fixtures issues, while also being capable of testing larger risk-volumes than most of the mentioned types of tests and directly providing a nominal tensile strength value stemming from a uniaxial stress state [46].

Even if the UST test method seemingly avoids or improves all the limitations mentioned for other mechanical tests, this work does not imply that the new procedure will be free of disadvantages of its own. The goal is to provide brittle materials research field with one more option for their mechanical characterization, which could be the most convenient solution depending on the testing limitations that need to be avoided.

1.2. Internal Defects in Brittle Materials

As previously established, the large scatter of experimental tensile strength data of brittle materials is due to the existence of internal defects, which can potentially be characterized according to their geometry (size, shape, spatial orientation), distribution (quantity, position within the specimen and relative to other defects), and origin (presence of impurities in the raw components and fabrication process limitations, that can generate unwanted inclusions, poor bonding between raw components, pores that are often filled with gas, and internal cracks). The ways in which internal defects can be characterized, on one hand, introduce a large number of variables that can influence the material nominal strength, on the other, they enable the use of different methods to correlate the presence of defects to the experimental strength.

Often those methods are statistical and based on size effect, i.e., by increasing the volume of material submitted to stress values close to the maximum stress on the specimen, referred to as risk-volume, the probability of having a larger critical defect also increases [47]. This concept was first hypothesized by Griffith, according to [48], and it is illustrated in Fig. 1.2, where two specimens are obtained from the same material volume, considering a scenario where both specimens are submitted to uniform normal stress σ_N, and assuming that failure will originate on their respective largest defect, in this example referred to as the critical defect, of size a_{cr}. Specimen 2, possessing the largest material volume, presents a higher probability of containing a larger critical defect than Specimen 1. Therefore, assuming that $a_{cr,2} > a_{cr,1}$, the relation between the specimens nominal stress at failure will be $\sigma_{N,0,1} > \sigma_{N,0,2}$. Therefore, larger specimens have, on average, lower mechanical strength than smaller specimens of the same material submitted to the same testing configuration.

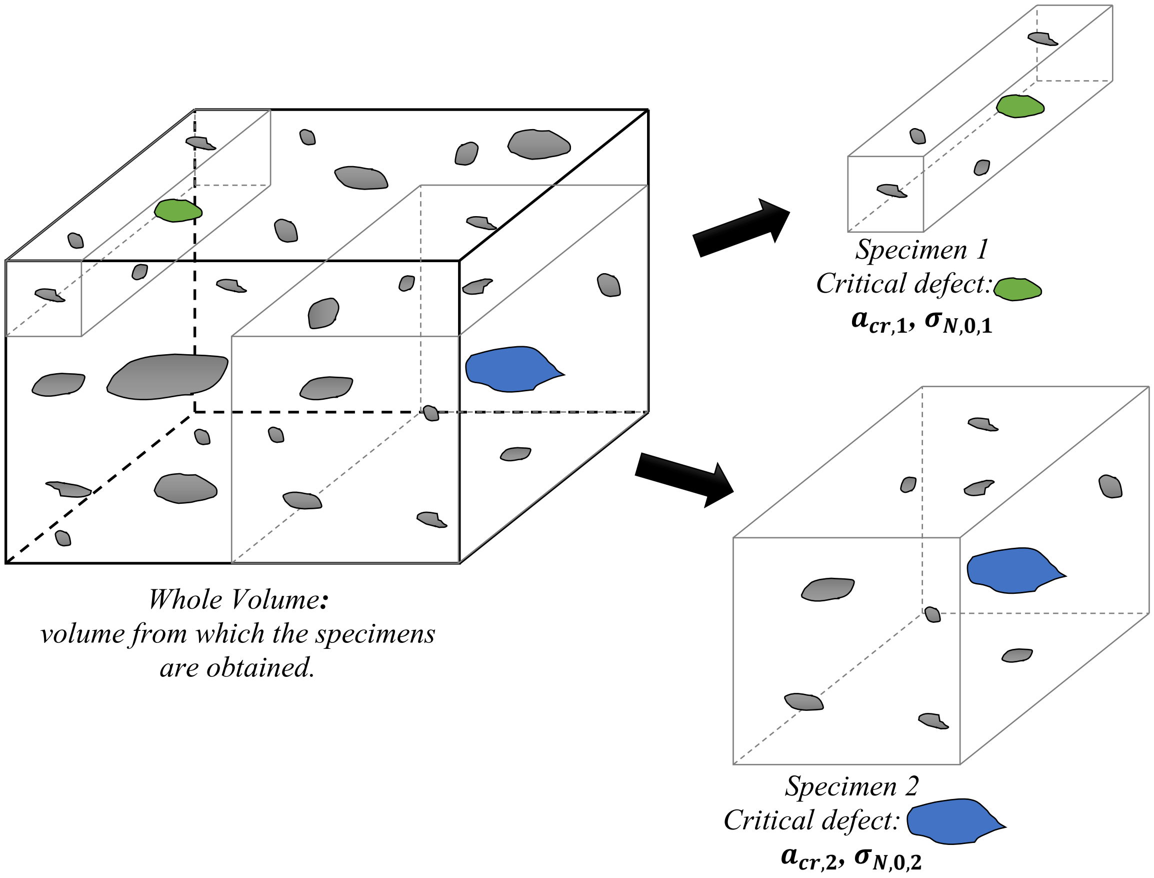

Figure 1.2 Illustration of size effect statistical principle, showing the specimen with largest risk-volume (2) also having the largest critical defect.

This method of correlation does not need to include a direct defect characterization and can be achieved through statistical models based on extreme value statistics, such as Gumbel [49] and Weibull [50], which then have their parameters calculated through the fitting of experimental data from multiple specimens of at least two different risk-volumes, as shown in [35] and [34]. Even though the internal defects are never actually characterized by this method, the statistical model can be applied to the final component design, since it generates a correlation between the risk-volume of material and probability of failure at a determined level of stress. This is illustrated in Fig. 1.3, which shows the fitting of the size effect statistical model based on Gumbel largest extreme value distribution, as presented in [35], applied to the experimental results from [51], who conducted tensile tests on four sets of specimens NBG-18 nuclear grade graphite of different risk-volumes V. Fig. 1.3b shows the cumulative probability of failure P for the respective tensile stress σ_N at failure to each tested risk-volume.

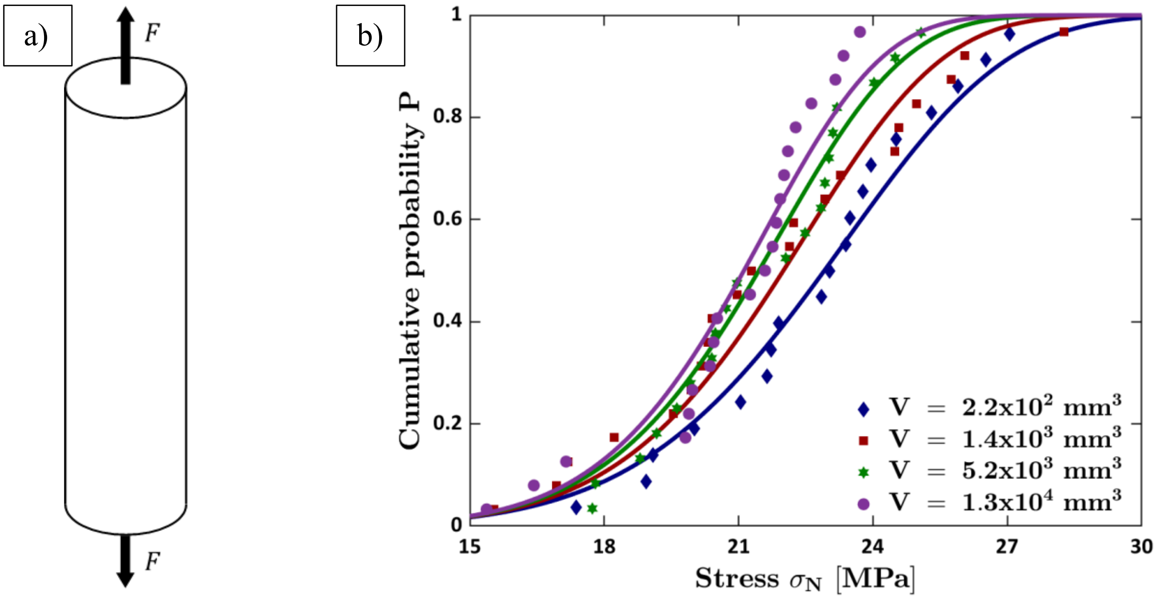

Figure 1.3 Tensile strength of NBG-18 nuclear grade graphite: (a) Schematic of the specimens geometry and test configuration (b) Experimental data and fitting curve for cumulative probability by tensile strength for each risk-volume.

However, experimental methods that do not necessarily focus on evaluating size effect and, hence, do not comprise the testing of sets of specimens of multiple risk-volumes, defect characterization methods that involve the direct observation and measurement of internal flaws should be applied. There are two such methods frequently found in the literature. The first is the observation of the fracture surface through microscopy to identify and measure the crack originating defect, which is commonly used in fatigue tests [52]. The advantage of this method is the fast identification and characterization of the critical defect, which only requires the observation of the fracture surface with enough magnification to produce reliable measurements. However, since fatigue tests usually show clear signs of crack propagation, such as “beach marks” and striations [53], the critical defect can be systematically identified in most, if not all, specimens, which might not be the case for other types of tests.

For instance, brittle materials suffer catastrophic failure when submitted to most types of tests, especially those involving high strain rates, causing an almost instantaneous crack propagation that produces ramifications towards the directions with the least local resistance, in most cases causing the detachment of several small fragments near the fracture zone, meaning that the crack propagation path and its origin are usually unclear, preventing the identification of the critical defect just from *post mortem* fracture surface observation. The contrasting results between the two situations can be noticed in Fig. 1.4 from specimens tested on the ultrasonic machine observed through Field Emission Scanning Electron Microscopy (FESEM), being Fig. 1.4a the fracture surface of Ti-6Al-4V submitted to a Very High Cycle Fatigue (VHCF) tensile test, and Fig. 1.4b the fracture surface of graphite R4550 submitted to the UST test method presented in this work. While the former shows clear signs of crack propagation, with potential characterization of the defect that originated fracture (as encircled in red in Fig. 1.4a), the latter presents no features that might allow the reliable identification of the critical defect.

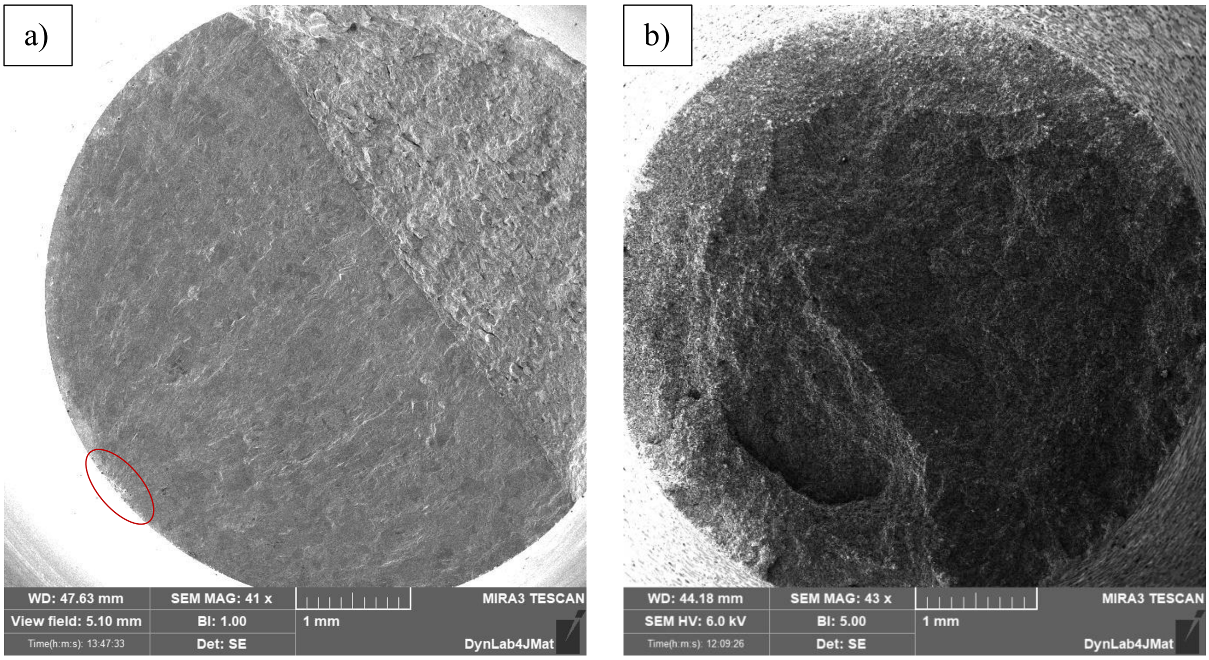

Figure 1.4 Comparison between two fracture surfaces of specimens from the ultrasonic testing machine: (a) VHCF test on Ti-6Al-4V and (b) UST test on graphite R4550.

The second method uses 3D x-ray imaging technology to characterize internal defects in a way that is not dependent on the systematically accurate evaluation of a fracture surface. This translates into conducting micro-Computed Tomography (micro-CT) scans on the specimens before any destructive test is conducted and relying on software for voxel reconstruction, visualization, and analysis [54]. Even though this is a more time demanding method, it allows the identification and characterization of the specimen entire defect population, and not only the critical defect, potentially being able to provide insights for fabrication process improvements. Given the potential contributions to the characterization of brittle materials, the micro-CT scans of all the specimens submitted to UST test should be conducted for defect analysis purposes and a method should be defined to identify the critical defect, or the defect where specimen failure most likely originated, independently of the fracture surface state.

1.3. Brittle Materials Applications

As pointed out before, the brittle definition encapsulates such a wide variety of materials that research on this field could potentially contribute to a number of applications and industries as well. Since this work focuses on validating the proposed experimental method on alumina and graphite, these materials applications are more extensively detailed in this section.

The first materials to be considered as possible experimental subjects to evaluate the method potential applications and limitations were technical ceramics, such as alumina (Al_2O_3), silicon carbide (SiC) and silicon nitride (Si_3N_4). These materials present, generally, isotropic linear-elastic behavior until their failure, along with often desirable characteristics of high hardness, resistance to abrasion, high temperature resistance, very high chemical stability (resistance to corrosion), and electrical and thermal insulation capabilities. Their drawback being their mechanical strength's extremely high dependance on the presence of flaws, often forcing the design of components to employ high safety factor values to compensate both for the possibility of a larger than expected critical defect and the general limitations of fracture mechanics models in predicting stress concentration.

Technical ceramics have a wide variety of applications in the medical field – as biomedical implants –, in the military field – as ballistic protection and vehicle armor –, in aerospace – as coatings of jet engine turbine blades and tiles used in the Space Shuttle Program –, in automotive – as a component of ceramic disc brakes –, in gas burner nozzles, and in ceramic matrix composites of gas turbine parts. Due to the high susceptibility of their internal flaws to tensile stresses, i.e., in the crack opening direction, and the difficulties in thoroughly assessing the tensile strength of these materials, they tend to be applied as an added layer of protection for a ductile material, such is the case of coatings and ballistic armor, or in components that are expected to be usually submitted to compressive loads, such as most prothesis. Nevertheless, extending the knowledge on their tensile behavior will improve their reliability, since many of their applications are expected to generate multiaxial stress states, with tensile loads being the most likely to cause flaw propagation despite their expected smaller magnitude.

Technical ceramics components production commonly involves powder sintering, while machining is usually avoided, if possible, since the latter process is complicated by the high hardness and mechanical resistance of these materials, which is largely the case for alumina, silicon carbide and silicon nitride. However, recent advances in additive manufacturing have allowed some technical ceramics to be 3D-printed in the desired shape through a fine ceramic powder bonded by a polymer, which is then removed during a sintering process. This was found to be the case for alumina, silicon carbide and zirconia, all of which are commercially available. However, the still existing process limitations regarding wall thickness ranges and attainable tolerances can often prevent the design of the required test specimens.

To verify the method potential application to brittle materials with nonlinear behavior, another material selected to be submitted to this experimental procedure was graphite, which already can be of many different varieties and forms, each one having their own microstructure, properties, and applications. Both the naturally occurring forms and the synthetically produced ones present high thermal and electrical conductivity, and high thermal stability, being oxidized only at temperatures above approximately 700 °C if exposed to oxygen-containing atmospheres. Graphite can be used in refractories, - specially in metallurgy, like crucibles, nozzles, throughs, and blast furnace linings, - in electrodes for batteries and electric arc furnaces, in steelmaking, in brake linings, in lubricants, in carbon fibers, in nuclear power plants as neutron moderator, and in scientific research as in Large Hadron Collider (LHC) collimators and beam dump.

Particularly, graphite R4550 is artificially produced by compressing the raw material mixture into rectangular or round blocks using a cold isostatic press, tendentially resulting in the smallest grain sizes amongst graphites, conferring it higher mechanical resistance. As one of the materials employed in LHC collimators, besides the properties found in other graphites, it has high thermal shock resistance and is very easy to machine.

Graphites in general are formed by stacked layers of graphene that are bonded between them through van der Waals forces, which, being relatively weak, are often occupied by gases and can be easily separated or made to glide over each other. One of the consequences from such a mechanism is that graphite tends to be strongly anisotropic, depending on its origin and industrial processing. It can, however, present isostatic properties, such is the case for isostatically pressed synthetic graphites, like R4550.

Furthermore, the possible existence of gases between graphene layers and the ease with which they can be made to slip over each other causes nonlinearities in the macroscopic mechanical behavior of graphite. Indeed, several works in the literature involving numerical modeling of graphite to mimic experimental results incorporate at least one nonlinear type of behavior into their material models, such as viscoelasticity [1], hyperelasticity [55], and plasticity [56], which are further discussed in Chapter 7, when analyzing the results obtained for graphite R4550, found to present not only a viscoelastic behavior, but different elastic moduli when submitted to tension and compression, respectively.

1.4. Objectives of the Thesis

Considering the previously mentioned importance in expanding the knowledge of tensile behavior of brittle materials and the relationship between their flaws and tensile strength, this work proposes an experimental and numerical approach consisting of three major procedures:

1) Defect characterization through micro-CT scanning, followed by identification of the critical defect, whose size is then correlated to the estimated nominal tensile strength through a Stress Intensity Factor (SIF) formulation;
2) Design of a new experimental method, referred to as the ultrasonic tensile test, used to estimate a value for the quasi-static tensile strength of brittle materials, as well as other uniaxial mechanical properties;
3) Application of the experimental data collected through the UST to a numerical Finite Element (FE) model to estimate the above-mentioned properties through an optimization procedure.

The defect characterization, as stated in point 1, comprises the identification of the internal flaw population on the interest zone of each studied specimen, which is scanned through micro-CT before the destructive mechanical test takes place. Moreover, given the tendency of brittle materials to undergo catastrophic failure, preventing the origin of fracture propagation to be pinpointed, the most reliable method to select the critical defect within the flaw population was to reconduct the CT scans on the specimen broken pieces after the destructive test mentioned in point 2. This should allow the formed fracture surfaces to be placed over the original scan, highlighting the flaws initially present in the fracture zone, amongst which the largest one is selected as the critical defect.

Although the above-described procedure does not necessarily identify the defect where fracture originated, it was designated as a reliable and repeatable strategy to quantify the critical defect of each specimen. The critical defect size can then be correlated with the nominal tensile strength through a SIF formulation based on the fitting of empirical data, and on Murakami's definition of fracture toughness for the 3D problem of a crack with arbitrary shape in an infinite body [57]. The general principle of x-ray micro-CT is explained in Section 2.1, while Chapter

3 is dedicated to detailing the instruments (hardware and software), the experimental method, and data analysis procedure concerning defect characterization, as well as the selected approach for SIF formulation.

The second point consists of the configuration and validation of the UST test, used to provide the measurements necessary for the identification of the material uniaxial mechanical properties, e.g., fracture strength and elastic modulus. The UST test is conducted on ultrasonic testing machines, commonly used in uniaxial VHCF tests, with one end of the specimen attached to the machine through butt-joint adhesive and one end remaining free, while a constant frequency vibration causes the specimen to enter longitudinal resonance, potentially generating the strain required for failure. Under these conditions, both the presence of mechanical grips on the specimen and the need for machine alignment are eliminated. Furthermore, the material is submitted only to uniaxial load, directly providing the value for the tensile strength, eliminating the need of estimating it from a multiaxial stress state. Finally, since the resonance condition is responsible for generating the stress field within the material, the specimens can potentially be designed with considerably larger risk-volumes than those of the test methods mentioned in Section 1.1 [58].

Although a number of brittle material components are submitted to cyclic loads during their life, such as biomedical implants (above 10^7 cycles for hip implants [59], and around 10^5 for dental implants [60]), and automotive components (around 10^6 cycles for brake discs [61]), they are usually employed under compressive cyclic loads, or as external layers of protection, such as coatings and ballistic armor, that encapsulate a ductile material with high resistance to fatigue. Hence, the development of the UST has as its main objective the estimation of a material strength value that would be measured in a quasi-static tensile test, despite using an ultrasonic testing device primarily designed for fatigue tests. This should be accomplished by aiming for material failure in a very low number of cycles, e.g., around $100\ cycles$, only necessary for achieving the resonance condition and the required stress, eliminating, or minimizing, the occurrence fatigue damage. The general principle of the UST test is explained in Section 2.2, while Chapter 4 is dedicated to the experimental design of the method adopted in this thesis, including software, hardware, specimens, data acquisition and analysis.

During the UST test, longitudinal displacements on the specimen are acquired to then be used on point 3, i.e., the FE model of the test. By applying the known machine output as boundary conditions, imposing the empirical displacements as objective, and selecting a proper numerical model for the material according to the behavior observed on the experimental curves, the material properties can be estimated through an optimization procedure. The goal of the third point is not only to provide an estimate for the properties, but also for the stress distribution on the moment of failure, more specifically the maximum stress globally achieved on the specimen and the largest local nominal stress generated on the position of the critical defect. Chapter 5 is dedicated to explaining the FE modeling approach adopted in this thesis, including element type, boundary condition, and optimization variables.

Thus, the three combined procedures should provide experimental information to determine a numerical material model, uniaxial mechanical properties, an estimate for the quasi-static tensile strength, internal defects characterization, the identification of the critical defect, and a SIF formulation. The successful completion of these goals means the validation of the described procedures, particularly the novel UST test, potentially providing the brittle materials field with results that could be applied to improve the efficiency and reliability of components design.

1.5. References

[1] L. Peroni, M. Scapin, F. Carra, and N. Mariani, “Investigation of dynamic fracture behavior of graphite,” *Key Eng. Mater.*, 2013, doi: 10.4028/www.scientific.net/KEM.569-570.103.

[2] K. Y. Volokh, “Hyperelasticity with softening for modeling materials failure,” *J. Mech. Phys. Solids*, vol. 55, no. 10, pp. 2237–2264, 2007, doi: 10.1016/j.jmps.2007.02.012.

[3] M. Sakai, K. Urashima, and M. Inagaki, “Energy Principle of Elastic-Plastic Fracture and Its Application to the Fracture Mechanics of a Polycrystalline Graphite,” *J. Am. Ceram. Soc.*, vol. 66, no. 12, 1983, doi: doi.org/10.1111/j.1151-2916.1983.tb11003.x.

[4] M. Scapin, C. Fichera, F. Carra, and L. Peroni, “Experimental investigation of the behaviour of tungsten and molybdenum alloys at high strain-rate and temperature,” *EPJ Web Conf.*, vol. 94, 2015, doi: 10.1051/epjconf/20159401021.

[5] “ASTM C1273 − 18 - Standard Test Method for Tensile Strength of Monolithic Advanced Ceramics at Ambient Temperatures,” *ASTM Int.*, 2019, doi: 10.1520/mnl10913m.

[6] C. Hou, X. Jin, L. Zhao, P. Li, and X. Fan, “Analysis of tensile strength and fracture toughness of ZrB2 – SiC ceramic from three-point bending samples with edge cracks,”

Ceram. Int., vol. 48, no. 20, pp. 30078–30085, 2022, doi: 10.1016/j.ceramint.2022.06.278.

[7] G. Liu *et al.*, "Inverse identification of tensile and compressive damage properties of graphite material based on a single four-point bending test," *J. Nucl. Mater.*, vol. 509, pp. 445–453, 2018, doi: 10.1016/j.jnucmat.2018.07.022.

[8] G. Zi, J. Kim, and Z. P. Bažant, "Size effect on biaxial flexural strength of concrete," *ACI Mater. J.*, vol. 111, no. 3, pp. 319–326, 2014, doi: 10.14359/51686576.

[9] J. Schlacher *et al.*, "Strength of additive manufactured alumina," *J. Eur. Ceram. Soc.*, vol. 40, no. 14, 2020, doi: 10.1016/j.jeurceramsoc.2020.03.073.

[10] Y. Li, C. Zhong, T. Qin, and M. Wang, "Preparation and performance of CaO-MgO-SiO2-Al2O3-CaF2 glass/Al2O3 ceramic with high flexural strength," *J. Non. Cryst. Solids*, vol. 602, 2023, doi: 10.1016/j.jnoncrysol.2022.122088.

[11] K. Kwok, L. Kiesel, H. L. Frandsen, M. Søgaard, and P. V. Hendriksen, "Strength characterization of tubular ceramic materials by flexure of semi-cylindrical specimens," *J. Eur. Ceram. Soc.*, vol. 34, no. 5, pp. 1423–1432, 2014, doi: 10.1016/j.jeurceramsoc.2013.12.005.

[12] H. Salavati, H. Mohammadi, Y. Alizadeh, and M. R. Ayatollahi, "3D fracture behaviour of graphite specimens weakened by V- notches with end holes under mixed mode (I+II) loading," *Eng. Fail. Anal.*, vol. 104, 2019, doi: 10.1016/j.engfailanal.2019.06.050.

[13] T. Fett, G. Rizzi, E. Ernst, R. Müller, and R. Oberacker, "A 3-balls-on-3-balls strength test for ceramic disks," *J. Eur. Ceram. Soc.*, vol. 27, no. 1, pp. 1–12, 2007, doi: 10.1016/j.jeurceramsoc.2006.02.033.

[14] M. Staudacher, P. Supancic, and T. Lube, "The Ball-on-Ring-test: Enhancing an analytical solution by numerical analysis for elastic deformation and small displacements," *J. Eur. Ceram. Soc.*, 2023, doi: 10.1016/j.jeurceramsoc.2023.06.016.

[15] G. Shams, P. Rivard, and O. Moradian, "Observation of fracture process zone and produced fracture surface roughness in granite under Brazilian splitting tests," *Theor. Appl. Fract. Mech.*, vol. 125, 2022, doi: 10.1016/j.tafmec.2022.103680.

[16] C. D. Newton, S. P. Jeffs, L. Gale, S. Pattison, and M. R. Bache, "Determining the interlaminar tensile strength of a SiCf/SiC ceramic matrix composite through diametrical compression testing," *J. Eur. Ceram. Soc.*, vol. 43, no. 7, 2023, doi:

10.1016/j.jeurceramsoc.2022.11.014.

[17] K. Kida, J. Koga, and E. C. Santos, “Crack growth and splitting failure of silicon nitride ceramic balls under cyclic pressure loads,” *Mech. Mater.*, vol. 106, 2017, doi: 10.1016/j.mechmat.2017.01.004.

[18] X. Zhang, Y. Yi, H. Zhu, G. Liu, L. Sun, and L. Shi, “Measurement of tensile strength of nuclear graphite based on ring compression test,” *J. Nucl. Mater.*, vol. 511, pp. 134–140, 2018, doi: 10.1016/j.jnucmat.2018.09.010.

[19] F. Berto, P. Lazzarin, and M. R. Ayatollahi, “Brittle fracture of sharp and blunt V-notches in isostatic graphite under pure compression loading,” *Carbon N. Y.*, vol. 63, pp. 101–116, 2013, doi: 10.1016/j.carbon.2013.06.045.

[20] Y. Xu, F. Dai, and H. Du, “Experimental and numerical studies on compression-shear behaviors of brittle rocks subjected to combined static-dynamic loading,” *Int. J. Mech. Sci.*, vol. 175, 2020, doi: 10.1016/j.ijmecsci.2020.105520.

[21] A. A. Wereszczak, O. M. Jadaan, H.-T. Lin, G. J. Champoux, and D. P. Ryan, “Hoop tensile strength testing of small diameter ceramic particles,” *J. Nucl. Mater.*, vol. 361, 2007, doi: 10.1016/j.jnucmat.2006.11.013.

[22] Y. J. Dai, S. L. Jin, R. Zhou, Y. W. Li, H. Harmuth, and E. K. Tschegg, “Mixed-mode fracture behaviour of refractories with asymmetric wedge splitting test. Part II: Experimental case study,” *Ceram. Int.*, vol. 48, no. 14, pp. 19757–19766, 2022, doi: 10.1016/j.ceramint.2022.03.244.

[23] J. Calaf-Chica, J. Martínez-Peña, P. M. Bravo Díez, and M. Preciado Calzada, “Ring Hoop Tension Test for yield strength estimation: Numerical analysis for a novel correlation method and applicability for mechanical testing of tubes and pipes,” *Mech. Mater.*, vol. 169, 2022, doi: 10.1016/j.mechmat.2022.104295.

[24] J. R. M. D’almeida and S. N. Monteiro, “The Iosipescu test method as a method to evaluate the tensile strength of brittle materials,” *Polym. Test.*, vol. 18, pp. 407–414, 1999, doi: 10.1016/S0142-9418(98)00043-9.

[25] D. J. Guerrero-Miguel, M. I. Alvarez-Fernández, M. B. Prendes-Gero, and C. González-Nicieza, “Determination of uniaxial tensile strength of brittle materials using tubular samples,” in *IOP Conference Series: Earth and Environmental Science*, Sep. 2021, vol. 833, no. 1. doi: 10.1088/1755-1315/833/1/012016.

[26] Z. Wang, D. Ma, T. Suo, Y. Li, and A. Manes, “Investigation into different numerical methods in predicting the response of aluminosilicate glass under quasi-static and impact loading conditions,” *Int. J. Mech. Sci.*, vol. 196, 2021, doi: 10.1016/j.ijmecsci.2021.106286.

[27] J. Y. Huang, J. C. Yuan, T. T. Zhu, T. Zhong, Y. F. Xu, and S. N. Luo, “Dynamic compressive strength of alumina ceramics,” *Ceram. Int.*, vol. 48, 2022, doi: 10.1016/j.ceramint.2022.08.196.

[28] G. Volkov and I. Smirnov, “A probabilistic approach to evaluate dynamic and static strength of quasi-brittle materials through high-rate testing,” *Int. J. Mech. Sci.*, vol. 216, 2022, doi: 10.1016/j.ijmecsci.2021.106960.

[29] Y. Sato and Y. Matsubara, “The fracture of a solid brittle bar due to impact bending,” *Int. J. Mech. Sci.*, vol. 16, 1974.

[30] J. Zheng, H. Li, and J. D. Hogan, “Strain-rate-dependent tensile response of an alumina ceramic: Experiments and modeling,” *Int. J. Impact Eng.*, vol. 173, 2023, doi: 10.1016/j.ijimpeng.2022.104487.

[31] Y. J. Deng, H. Chen, X. W. Chen, and Y. Yao, “Dynamic failure behaviour analysis of TiB2-B4C ceramic composites by split Hopkinson pressure bar testing,” *Ceram. Int.*, vol. 47, no. 15, pp. 22096–22107, 2021, doi: 10.1016/j.ceramint.2021.04.231.

[32] L. F. Friedrich, B. Colpo, L. E. Kosteski, S. Vantadori, and I. Iturrioz, “A novel peridynamic approach for fracture analysis of quasi-brittle materials,” *Int. J. Mech. Sci.*, vol. 227, 2022, doi: 10.1016/j.ijmecsci.2022.107445.

[33] T. C. Triantafillou and L. J. Gibson, “Multiaxial Failure Criteria For Brittle Foams,” *Int. J. Mech. Sci.*, vol. 32, no. 6, pp. 479–496, 1990.

[34] A. P. Pagnoncelli, A. Tridello, and D. S. Paolino, “Static strength of brittle materials under multiaxial nonuniform stress states: A novel statistical model for assessing size effects,” *Fatigue Fract. Eng. Mater. Struct.*, vol. 44, no. 4, pp. 997–1013, Apr. 2021, doi: 10.1111/ffe.13409.

[35] A. P. Pagnoncelli, A. Tridello, and D. S. Paolino, “Modelling size effects for static strength of brittle materials,” *Mater. Des.*, vol. 195, Oct. 2020, doi: 10.1016/j.matdes.2020.109052.

[36] Z. Li, K. F. Wang, B. L. Wang, and J. E. Li, “Size effect on the punch performance of

brittle porous ceramics: Theoretical analysis and numerical simulation," *Int. J. Mech. Sci.*, vol. 207, 2021, doi: 10.1016/j.ijmecsci.2021.106674.

[37] S. Samadi, S. Jin, D. Gruber, and H. Harmuth, "A comparison of two damage models for inverse identification of mode I fracture parameters : Case study of a refractory ceramic," *Int. J. Mech. Sci.*, vol. 197, 2021, doi: 10.1016/j.ijmecsci.2021.106345.

[38] G. R. Irwin, "Analysis of stresses and strains near the end of a crack traversing a plate," *J. Appl. Mech.*, vol. 24, no. 3, pp. 361–364, 1957, doi: 10.1115/1.4011547.

[39] F. Eggers, J. H. S. Almeida, C. B. Azevedo, and S. C. Amico, "Mechanical response of filament wound composite rings under tension and compression," *Polym. Test.*, vol. 78, 2019, doi: 10.1016/j.polymertesting.2019.105951.

[40] A. Sidi, D. Gruber, H. Harmuth, and S. Jin, "Tensile creep measurements of ordinary ceramic refractories at service related loads including setup, creep law, testing and evaluation procedures," *Ceram. Int.*, vol. 42, no. 6, pp. 6791–6799, 2016, doi: 10.1016/j.ceramint.2016.01.056.

[41] J. Zhao, C. Yan, S. Liu, J. Zhang, S. Li, and Y. Yan, "Effect of solid waste ceramic on uniaxial tensile properties and thin plate bending properties of polyvinyl alcohol engineered cementitious composite," *J. Clean. Prod.*, vol. 268, 2020, doi: 10.1016/j.jclepro.2020.122329.

[42] T. Dikova, T. Vasilev, and N. Dolgov, "Failure of ceramic coatings on cast and selective laser melted Co-Cr dental alloys under tensile test: Experiment and finite element analysis," *Eng. Fail. Anal.*, vol. 105, 2019, doi: 10.1016/j.engfailanal.2019.07.018.

[43] V. Mazars *et al.*, "Damage investigation and modeling of 3D woven ceramic matrix composites from X-ray tomography in-situ tensile tests," *Acta Mater.*, vol. 140, 2017, doi: 10.1016/j.actamat.2017.08.034.

[44] J. Bauer *et al.*, "Push-to-pull tensile testing of ultra-strong nanoscale ceramic – polymer composites made by additive manufacturing," *Extrem. Mech. Lett.*, vol. 3, 2015, doi: 10.1016/j.eml.2015.03.006.

[45] E. B. Callaway and F. W. Zok, "Tensile response of unidirectional ceramic minicomposites," *J. Mech. Phys. Solids*, vol. 138, 2020, doi: 10.1016/j.jmps.2020.103903.

[46] A. P. Pagnoncelli, D. S. Paolino, L. Peroni, and A. Tridello, "Innovative tensile test for

brittle materials: Validation on graphite R4550," *Int. J. Mech. Sci.*, 2023, doi: 10.1016/j.ijmecsci.2023.108679.

[47] A. Tridello, "A novel experimental approach for the assessment of size effect in VHCF," Politecnico Di Torino, Torino, TO, Italy, 2016.

[48] S. W. Freiman and J. J. Mecholsky, *The Fracture of Brittle Materials: Testing and Analysis*. 2012. doi: 10.1002/9781118147757.

[49] E. J. Gumbel, "The Return Period of Flood Flows," *Ann. Math. Stat.*, vol. 12, no. 2, pp. 163–190, 1941, doi: 10.1214/aoms/1177731747.

[50] W. Weibull, *A statistical theory of strength of materials*, Handlingar. Stockholm: Generalstabens litografiska anstalts förlag, 1939.

[51] J. H. Yoon, T. S. Byun, J. P. Strizak, and L. L. Snead, "Characterization of tensile strength and fracture toughness of nuclear graphite NBG-18 using subsize specimens," *J. Nucl. Mater.*, vol. 412, no. 3, pp. 315–320, 2011, doi: 10.1016/j.jnucmat.2011.03.019.

[52] A. Tridello *et al.*, "VHCF response of heat-treated SLM Ti6Al4V Gaussian specimens with large loaded volume," in *Procedia Structural Integrity*, 2019, vol. 18, pp. 314–321. doi: 10.1016/j.prostr.2019.08.171.

[53] H. Wang and J. A. J. Wang, "Bending testing and characterization of surrogate nuclear fuel rods made of Zircaloy-4 cladding and aluminum oxide pellets," *J. Nucl. Mater.*, vol. 479, Oct. 2016, doi: 10.1016/j.jnucmat.2016.07.044.

[54] C. Colombo *et al.*, "Efficient experimental methods for rapid fatigue life estimation of additive manufactured elements," *Int. J. Fatigue*, vol. 167, p. 107345, Feb. 2023, doi: 10.1016/J.IJFATIGUE.2022.107345.

[55] P. Jaszak, "Modeling of the elastic properties of compressed expanded graphite - A material used in spiral wound gaskets," *Int. J. Press. Vessel. Pip.*, vol. 187, Nov. 2020, doi: 10.1016/j.ijpvp.2020.104158.

[56] S. Vinod *et al.*, "Strain Rate Dependent Shear Plasticity in Graphite Oxide," *Nano Lett.*, vol. 16, no. 2, pp. 1127–1131, 2016, doi: 10.1021/acs.nanolett.5b04346.

[57] Y. Murakami, *Theory of elasticity and stress concentration*. 2016. doi: 10.1002/9781119274063.

[58] A. Tridello, D. S. Paolino, and M. Rossetto, "Ultrasonic VHCF tests on very large

specimens with risk-volume up to 5000 mm^3," *Appl. Sci.*, vol. 10, no. 7, Apr. 2020, doi: 10.3390/app10072210.

[59] M. G. Stewart and A. O'Connor, "Probabilistic risk assessment and service life performance management of load bearing biomedical implants," *Reliab. Eng. Syst. Saf.*, vol. 108, pp. 49–55, 2012, doi: 10.1016/j.ress.2012.06.012.

[60] L. C. Anami, J. M. C. Lima, L. F. Valandro, C. J. Kleverlaan, A. J. Feilzer, and M. A. Bottino, "Fatigue resistance of Y-TZP/porcelain crowns is not influenced by the conditioning of the intaglio surface," *Oper. Dent.*, vol. 41, no. 1, 2016, doi: 10.2341/14-166-L.

[61] F. Karabudak, "Fatigue analysis of the vehicle brake disc," *Gümüşhane Üniversitesi Fen Bilim. Enstitüsü Derg.*, vol. 11, 2021, doi: 10.17714/gumusfenbil.822064.

Chapter 2

2. Proposed Experimental Methods

In this chapter, the theoretical basis for the two experimental procedures, i.e., the defect analysis through x-ray 3D digital imaging and the theoretical concept of UST test will be detailed.

2.1. X-Ray Micro-Computed Tomography

In the recent decades, the rapid advances in x-ray tomography for medical diagnostics have allowed its expansion into the materials research field, in part thanks to its concurrency with the growth in additive manufacturing, responsible for the development and production of materials with an increase in flaws, both in number and size [1]. Nevertheless, since the advantages of these processes, mainly related to geometrical flexibility and low production cost, often outweigh the resulting materials mechanical disadvantages, they have become widely used over the recent years, and so has the use of micro-CT for non-destructive internal inspection of these materials. These analyses provide not only information on the component reliability but are also used as basis for process improvements and the final product quality control [2].

Micro-CT machines used in the materials research field are usually of the cone-beam type, comprised by an x-ray source (also called x-ray tube), a flat detector panel and a stage that holds the object to be scanned, as shown in a top view schematic in Fig. 2.1. It is important to underline in Fig. 2.1 that the coordinate system, with the z-axis coinciding with the vertical direction, will be the same adopted in all instances of this work, corresponding to its global coordinate system.

The stage and the detector can usually translate in the three axis directions, while the source always remains fixed. The x-rays are generated inside the tube as ionizing radiation, by passing a high voltage current through a tungsten filament, taking the form of a cone after exiting the source.

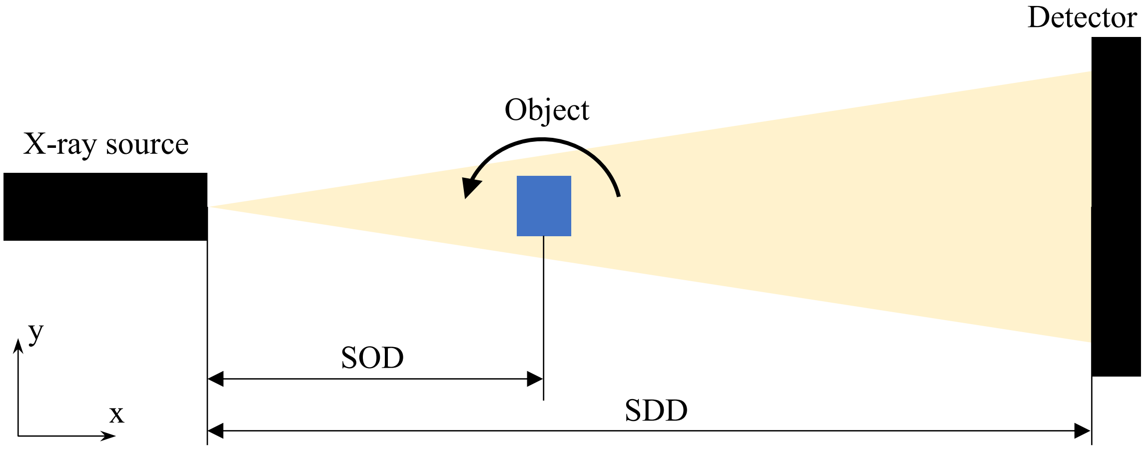

Figure 2.1 Schematic representation of the cone-beam micro-CT scanner.

During the scan, the stage rotates around its vertical axis, z as in Fig. 2.1, stopping in constant angle steps so that the object projections can be acquired. The projections consist of the capture, by the detector, of the remaining x-ray beam intensity that was not absorbed while passing through the scanned object. Once either a stage full rotation (360°) or a half-rotation (180°), depending on the micro-CT scanner configuration, is completed, the projections can be used to digitally reconstruct the scanned object.

The beam conic disposition allows the object magnification up to a micrometrical scale, following the equation for the resolution:

$$r_{CT} = p_p \cdot \frac{SOD}{SDD}, \tag{2.1}$$

being SOD and SDD, respectively the source-object distance and the source-detector distance, as described by Fig. 2.1, and p_p the pixel pitch, i.e., the physical length of the side of detector pixels.

The power passing through the tungsten filament can be set according to the object being scanned. Elements with larger atomic numbers absorb more beam intensity, and so does increasing their quantity, meaning that objects with larger sizes or higher densities require a higher power setting, otherwise the scanned object could almost completely absorb the beam, not letting any intensity be captured by the detector. In the opposite extreme, smaller objects or with lower densities should be scanned with a lower power setting, since their low beam absorption capabilities would let nearly 100% of its original intensity hit the detector. In both cases, the resulting projections would not possess enough contrast within the object, with the former situation being demonstrated in Fig. 2.2a, and the latter in Fig. 2.2b, while Fig. 2.2c shows the adequate power setup to scan this object. While in Fig. 2.2a and Fig. 2.2b, the main crack inside the object is visible even with inadequate contrast, the smaller material imperfections can be best identified in Fig. 2.2c.

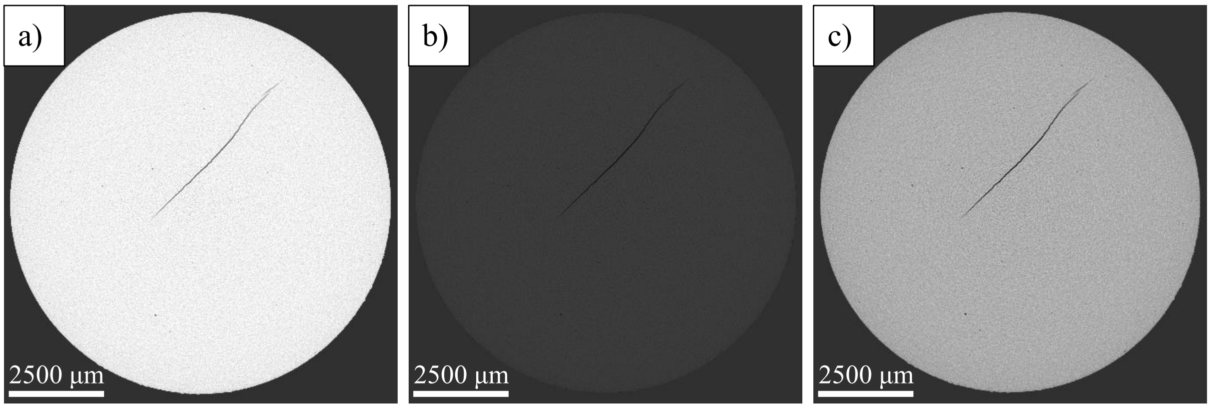

Figure 2.2 Illustration of filament power level effect on the obtained results, with (a) too low, (b) too high, and (c) an adequate level for this object.

Another setup parameter that must be selected accordingly is the filter, which consists of sheets of different thicknesses and materials – most commonly aluminum, copper, tin, and molybdenum –, that should be placed at the tube exit to filter the beam, removing rays below a certain energy level to reduce a phenomenon called beam hardening. This phenomenon is accentuated when objects of higher x-ray attenuation capacity are scanned, and results in the false impression of zones with higher density than their surroundings in the scan that do not exist in the real object. The absorption capacity of the filter should increase in correspondence to the increase in the absorption capacity of the object.

Furthermore, it is highly recommended that the object be fully comprised inside the detector width (in the y-direction from Fig. 2.1) in all projections, i.e., during the whole rotation required by the scan. This is because the x-ray absorption by the parts that are present in some projections but absent in others will cause errors in the resulting reconstruction, such as adding the perception of inexistent flaws or lowering the representation accuracy of actual flaws. Meanwhile, the object does not need to fit completely inside the detector height (in the z-direction), resulting in the parts vertically left out simply never being a part of any of the scan projections, hence, not affecting them.

Once the tomography is completed, software for image reconstruction is employed to convert the 2D projections into the 3D digital image. The reconstruction process converts the 2D pixels from the projections into their 3D counterparts, called voxels. The digital object can be visualized in a 3D format or in 2D by moving through its slices – stacked layers of voxels – on either of the three cartesian planes, as represented in Fig. 2.3, which also shows the respective positions of the slices with respect to the object center, being $1250\ \mu m$ in the xy-plane, $200\ \mu m$ in the yz-plane and $-100\ \mu m$ in the xz-plane.

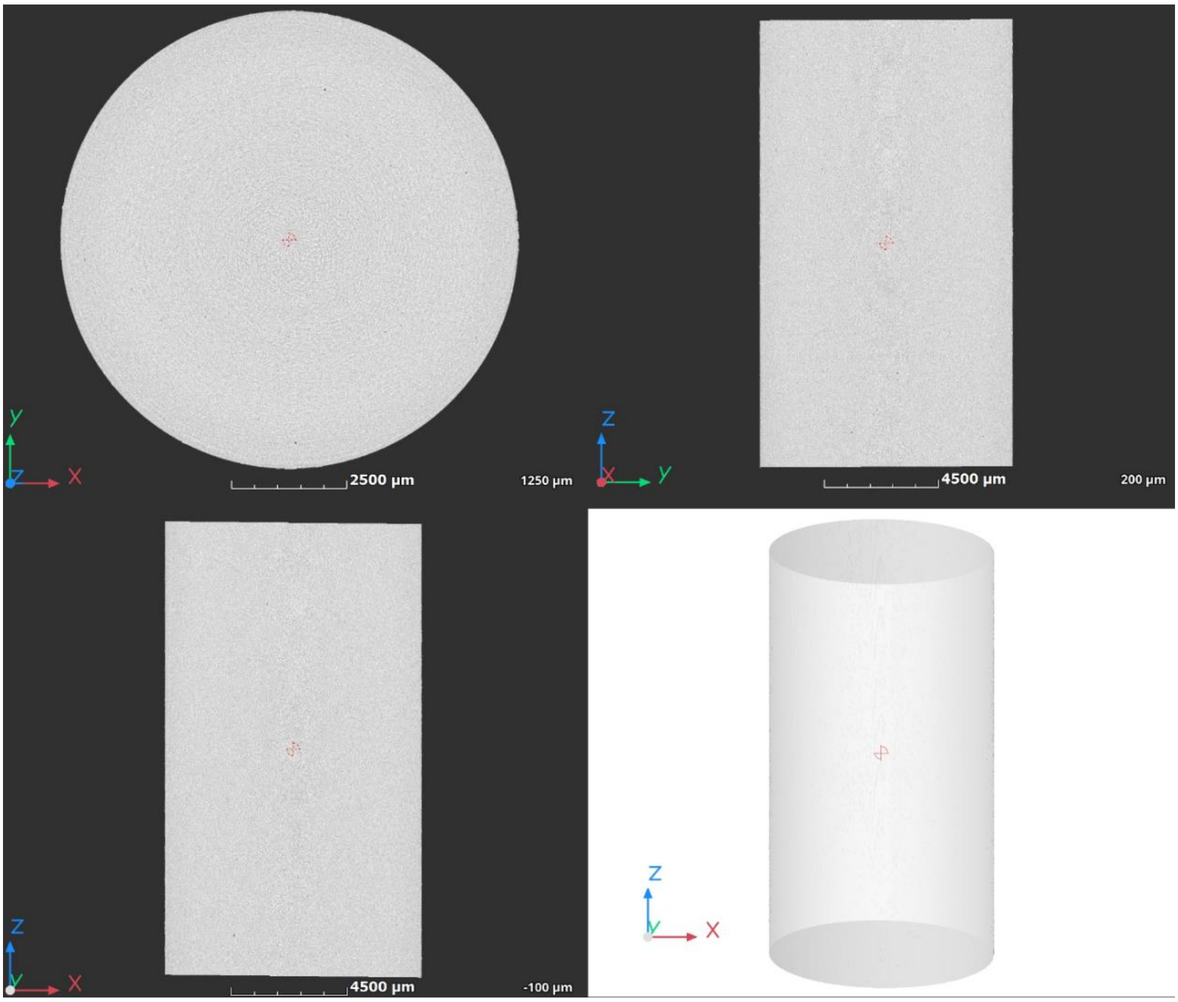

Figure 2.3 Representation of a digitally reconstructed micro-CT scanned volume, showing the slices in the three planes and the 3D representation.

Each voxel is also associated with a value in the grayscale, according to the beam intensity values captured by the detector during the projections acquisition. In the reconstruction shown as example in Fig. 2.3, the voxels with higher grayscale values are brighter and correspond to the object zones of higher absorption of beam intensity. By extension, voxels with lower grayscale values are darker and represent lower absorption regions. The algorithms for defect analysis use these values to identify material flaws, which are usually referred to either as porosities – the darker spots, representing a lack of material – or as inclusions – the brighter spots, potentially containing a higher density constituent.

2.2. Ultrasonic Tensile Testing

VHCF tests were developed to test materials used in structural components requiring very large fatigue lives (up to $10^{10}\ cycles$) [3]. Such experiments commonly use resonance testing machines having a loading frequency of at least $20\ kHz$ (ultrasound), allowing a considerable reduction of testing time. Although this method was initially applied to uniaxial fatigue tests (tension-compression), over the last decade, new configurations for fatigue tests using the ultrasonic machine have seen a rapid increase, including bending, torsion, multiaxial tension-compression and torsion, and in-plane biaxial stress [4].

This flexibility of the ultrasonic equipment has allowed the development of the UST test method proposed and validated in this thesis. By using the same device configuration as the one applied to tension-compression (uniaxial) VHCF, the UST test aims to fracture brittle materials specimens through the stress generated by the longitudinal resonance state, reaching the material ultimate stress in very few cycles – the minimum number allowable by the equipment – avoiding fatigue damage. With negligible influence of cyclic loading, the calculated uniaxial strength should be a close estimate to values attainable in quasi-static uniaxial tests for the same risk-volume.

Additionally, this configuration of the ultrasonic device applies a theoretical mean load equal to zero on the specimen, meaning that the magnitudes of the tension and compression loads have equal values for the same machine output. With brittle materials being known for their considerably lower resistance in tension than in compression, the material is expected to reach its tensile limit much sooner than its compression limit, systematically causing failure of all tested specimens while under tensile load. Under these assumptions, i.e., all specimens breaking under tensile load, and with that load corresponding to a good estimate of a quasi-static tensile strength value, it is reasonable to refer to this experimental method as the ultrasonic tensile test.

In the UST test configuration, an amplifying horn is attached to the machine with a screw, and the specimen is then attached to the horn with an adhesive, as shown in Fig. 2.4. The machine then makes the horn-specimen system vibrate longitudinally (z-direction), putting it under a resonance state, at an ultrasonic frequency, with a predetermined amplitude of vibration at the machine-horn interface.

The horn’s purpose is to work as an amplifier, multiplying the imposed amplitude by a constant factor depending on its own geometric characteristics, resulting in the amplitude of vibration that is transmitted to the specimen at the horn-specimen interface. Meanwhile, the specimen is symmetric, potentially having one of the following geometries: constant section (like a bar or a rod), dog-bone, or hourglass. The latter is represented in Fig. 2.4 together with the horn.

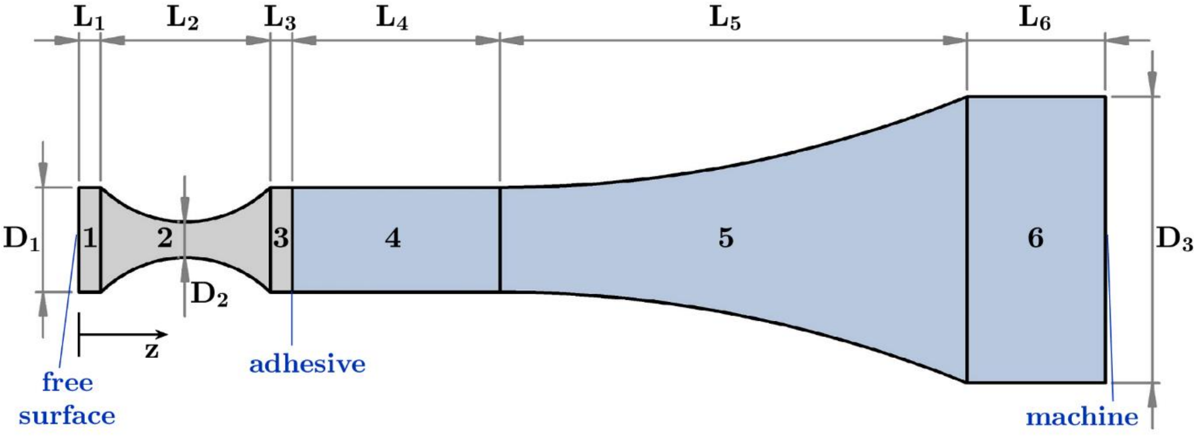

Figure 2.4 Horn-specimen system configuration of the UST test method.

Once in resonance, the system displacement amplitudes can be expressed by Eq. 2.2, according to [3]:

$$\begin{cases} u_1(z_1) = A_1 cos(k_s z_1) + B_1 sin(k_s z_1), & 0 \leq z_1 \leq L_1 \\ u_2(z_2) = \dfrac{A_2 cos\left(z_2\sqrt{k_s^2-\alpha_s^2}\right) + B_2 sin\left(z_2\sqrt{k_s^2-\alpha_s^2}\right)}{cosh\left[\alpha_s\left(z_2-\frac{L_2}{2}\right)\right]}, & 0 \leq z_2 \leq L_2 \\ u_3(z_3) = A_3 cos(k_s z_3) + B_3 sin(k_s z_3), & 0 \leq z_3 \leq L_3 \\ u_4(z_4) = A_4 cos(k_h z_4) + B_4 sin(k_h z_4), & 0 \leq z_4 \leq L_4 \\ u_5(z_5) = \dfrac{A_5 cos\left(z_5\sqrt{k_h^2-\alpha_h^2}\right) + B_5 sin\left(z_5\sqrt{k_h^2-\alpha_h^2}\right)}{cosh[\alpha_h z_5]}, & 0 \leq z_5 \leq L_5 \\ u_6(z_6) = A_6 cos(k_h z_6) + B_6 sin(k_h z_6), & 0 \leq z_6 \leq L_6 \end{cases} \tag{2.2}$$

where u_i $(i = 1, \ldots, 6)$ represents the displacement amplitudes in the i-th part of the horn-specimen system, while $k_s = 2 \cdot \pi \cdot f_{n,s}/\sqrt{E_s/\rho_s}$ (being $f_{n,s}$ the specimen resonance frequency, ρ_s the specimen density and E_s the specimen elastic modulus), $k_h = 2 \cdot \pi \cdot f_{n,h}/\sqrt{E_h/\rho_h}$ (being $f_{n,h}$ the horn resonance frequency, ρ_h the horn density and E_h the horn elastic modulus), $\alpha_s = 2 \cdot acosh(D_1/D_2)/L_2$ and $\alpha_h = acosh(D_3/D_1)/L_5$. The terms A_i and B_i are complex coefficients, which can be determined by the imposition of adequate boundary conditions.

Starting with the specimen free surface at $z = 0$, where the real term of the displacement amplitude is equal to U_f, i.e., the amplitude at the free extremity of the specimen, while its imaginary term and both the real and imaginary terms of the strain amplitude are equal to zero, resulting in the following coefficients:

$$\begin{bmatrix} A_1 \\ B_1 \end{bmatrix} = \begin{bmatrix} U_f \\ 0 \end{bmatrix} \tag{2.3}$$

The remaining coefficients are obtained by imposing the continuity of displacement and strain amplitudes between each pair of adjacent parts in the horn-specimen system (Fig. 2.4), with ε_i $(i = 1, \dots, 6)$ being the strain amplitude in the i-th part of the system and $j = 1, \dots, 5$:

$$\begin{cases} Re[u_j(z_j = L_j)] = Re[u_{j+1}(z_{j+1} = 0)] \\ Im[u_j(z_j = L_j)] = Im[u_{j+1}(z_{j+1} = 0)] \\ Re[\varepsilon_j(z_j = L_j)] = Re[\varepsilon_{j+1}(z_{j+1} = 0)] \\ Im[\varepsilon_j(z_j = L_j)] = Im[\varepsilon_{j+1}(z_{j+1} = 0)] \end{cases} \tag{2.4}$$

Both the specimen and the horn are designed so that, when the machine applies a harmonic longitudinal displacement at the base of the horn with the natural frequency of the horn-specimen system, a longitudinal resonance condition is generated. Under a regime resonance condition, i.e., with a constant amplitude harmonic displacement being applied, Eq. 2.2 results in the longitudinal amplitudes of displacement and strain according to Fig. 2.5. This distribution of amplitudes happens when both the horn and the specimen individually have the exact same first mode of longitudinal natural frequency as the excitation frequency of the ultrasonic device, as well as purely linear-elastic behavior, being the ideal resonance condition.

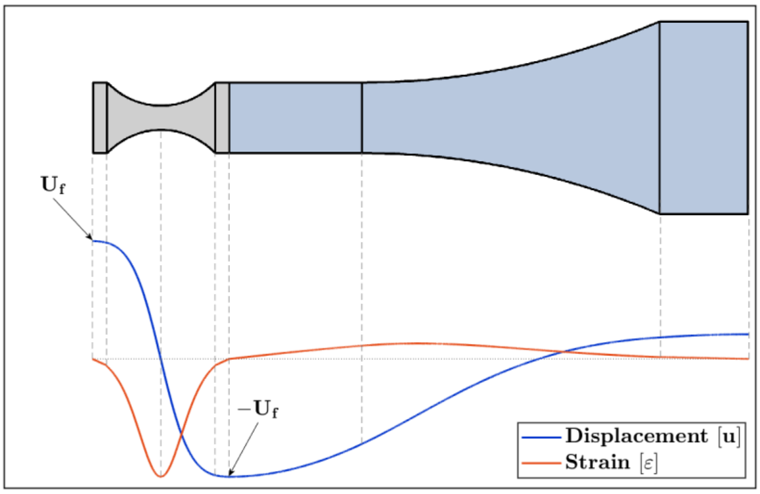

Figure 2.5 Behavior of the longitudinal displacement and strain amplitude curves along the horn-specimen system.

The graphics in Fig. 2.5 show that there are two displacement nodes, i.e., the cross-sections that do not move under resonance condition, and have displacement amplitude equal to zero, being one on the horn and one at the center of the specimen. Although amplitudes are often represented as absolute values, those plotted in Fig. 2.5 show changes in signal to indicate phase inversion. When the displacement amplitude changes signal, from positive to negative, or vice-versa, the phase of the harmonic movement is inverted, with the displacements of the cross-sections on one side of the node being in counterphase with those on the other side.

Moreover, even though it is unusual to use the term “strain nodes” to refer to the cross-sections with strain amplitudes equal to zero, the meaning of the signal change in the strain amplitude curve is analogous to that of the displacement. In the case of the specimen, due to its symmetric geometry, the displacement node also corresponds to its cross-section being submitted to maximum strain amplitude.

The above-mentioned characteristics of the curves in Fig. 2.5 infer that they are not only representative of the amplitudes of the harmonic displacements and strains on each cross-section of the horn-specimen system, but also depict the instantaneous displacement and strain distribution for the time t_k when $u(t = t_k, z = 0) = u_{z,f}(t = t_k) = U_f$. In this instant, the entire specimen is under compression, while the horn is entirely under tension, with the phase inversion of the load happening at the horn-specimen interface. Since the specimen is symmetric, the presented analytical formulation for the resonance state also implies that $u_{z,a}(t) = -u_{z,b}(t)$, being a and b two cross-sections of the specimen symmetrically placed with respect to its central cross-section, for instance, $u_{z,f}(t) = -u_{z,int}(t)$, being $u_{z,f}(t)$ the displacement over time at the free extremity of the specimen, and $u_{z,int}(t)$ the one at the horn-specimen interface.

In the ideal resonance state, i.e., in regime condition, the cross-section located on the interface has constant strain equal to zero. In reality, the specimen and the horn often have slightly different longitudinal natural frequencies from each other, which, in turn, are slightly different from the natural frequency of the vibrating parts of the ultrasonic testing device. However, the ultrasonic device still has an operating range of frequencies, and the horn and specimen need to respect this constraint to generate the resonance condition, which would end up with a similar distribution as the curves in Fig. 2.5 considering linear-elastic materials, but with a slight modification on the location of the displacement node, which is further detailed in Chapter 7.

Therefore, although a small strain level on the horn-specimen interface is expected due to the above-mentioned differences in natural frequencies, as well as the ramp that happens between rest condition and regime state when the machine starts, the strain values on the interface are still expected to be small enough to allow the specimen to be glued to the horn with an adhesive. A common adhesive is usually able to withstand the entirety of the test, while also avoiding the introduction of cracks and local stress like the mechanical fixtures in the traditional tensile tests for ceramics [5]. Furthermore, since one of the specimen extremities remains free, its alignment would not be a concern, so long as it is fixed sufficiently concentrically to the horn.

Moreover, assuming the system respects the design requirements by having its longitudinal resonance frequency comprised within the machine own operating frequency range, then the main restraints for which materials and specimen geometries can be successfully submitted to this method are related to the machine displacement amplitude range. Since the resonance state directly generates the strains on the specimen, independently of its mechanical resistance, this method potentially allows the investigation of materials with high strength, many of which are known for withstanding very small strains.

2.3. References

[1] A. du Plessis, I. Yadroitsava, and I. Yadroitsev, "Effects of defects on mechanical properties in metal additive manufacturing: A review focusing on X-ray tomography insights," *Mater. Des.*, vol. 187, Feb. 2020, doi: 10.1016/j.matdes.2019.108385.

[2] E. Maire and P. J. Withers, "Quantitative X-ray tomography," *Int. Mater. Rev.*, vol. 59, no. 1, pp. 1–43, 2014, doi: 10.1179/1743280413Y.0000000023.

[3] A. Tridello, D. S. Paolino, G. Chiandussi, and M. Rossetto, "Gaussian specimens for VHCF tests: Analytical prediction of damping effects," *Int. J. Fatigue*, vol. 83, May 2016, doi: 10.1016/j.ijfatigue.2015.04.025.

[4] P. R. Costa, D. Montalvão, M. Freitas, R. Baxter, and L. Reis, "Cruciform specimens' experimental analysis in ultrasonic fatigue testing," *Fatigue Fract. Eng. Mater. Struct.*, vol. 42, no. 11, pp. 2496–2508, 2019, doi: 10.1111/ffe.13041.

[5] "ASTM C1273 − 18 - Standard Test Method for Tensile Strength of Monolithic Advanced Ceramics at Ambient Temperatures," *ASTM Int.*, 2019, doi: 10.1520/mnl10913m.

Chapter 3

3. Defect Characterization

In this chapter, the equipment used for the specimen defect characterization is detailed, comprising the micro-CT scanner and the software for reconstruction, visualization, and analysis of tomography data, as well as the methods used in the selection of test parameters and algorithms for analysis of experimental data.

3.1. Micro-CT Scanner

The machine used in this experiment is custom-made with cone x-ray beam and flat detector panel. The device was designed and built by Fraunhofer Institute IKTS, and its interior is shown in Fig. 3.1, also indicating its main components, as well as identifying SOD and SDD.

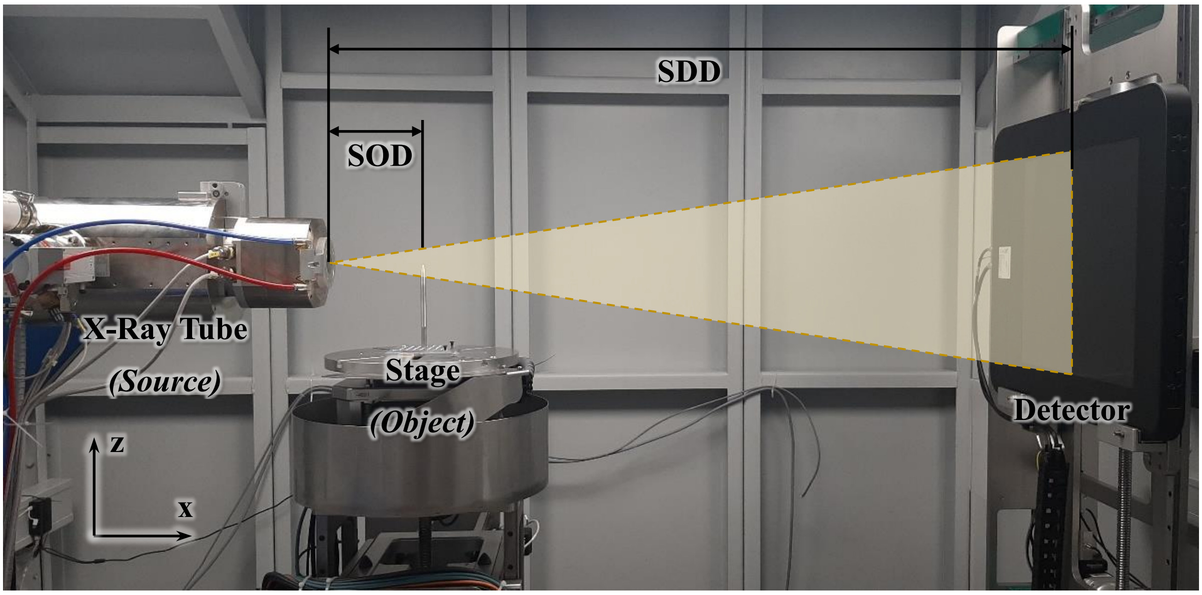

Figure 3.1 Micro-CT scanner used in the experiments.

This machine allows a maximum value of SDD of $1900\ mm$, and a minimum value of SOD of $25\ mm$, requiring a minimum difference between SDD and SOD of $400\ mm$, to avoid collision between detector and stage. The detector has a pixel pitch $p_p = 200\ \mu m$, being comprised of $2048 \times 2048\ pixels$. The stage does a full 360° counterclockwise rotation around z-axis during the scan, stopping at constant steps for the projections acquisition.

A full scan in this machine can contain from 400 to 6400 projections. The minimum recommended number of projections for an object that occupies the entire width of the detector (in the y-direction as per Fig. 3.1) is 1600, so as to avoid quality loss and reconstruction errors due to low sampling of projections. The minimum sampling $n_{proj,min}$ can be calculated as in Eq. 3.1, valid for a cone beam CT with 360° of scanning rotation.

$$n_{proj,min} = \frac{\pi}{4} \cdot \frac{w_{obj}}{r_{CT}} \tag{3.1}$$

where r_{CT} is the scan resolution as explained in Section 2.1, and w_{obj} is the object width, corresponding to the diameter occupied during a complete scan, as represented in Fig. 3.2, with w_{det} showing the physical width captured by the detector, corresponding to the space around the object that is acquired in the projections during that scan. For this machine, $w_{det}/r_{CT} = 2048\ pixels$.

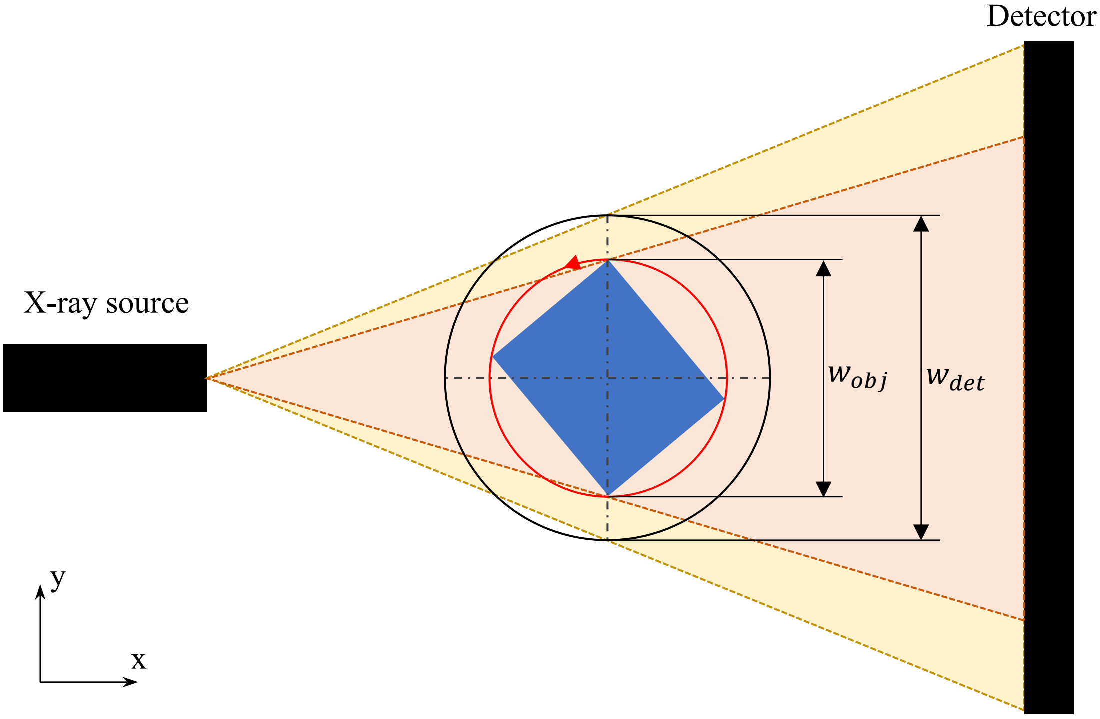

Figure 3.2 Schematic representation of the top view of the CT scanner, indicating the physical diameter occupied by the object (in blue) during a scan and the diameter captured by the detector.

As per Fig. 3.2, the better the object is placed concentrically to the stage axis of ration, the smaller w_{obj} will be, reducing the minimum required number of projections. Moreover, the ideal sampling for micro-CT scans intended for defect analysis should be twice the calculated minimum, which corresponds to the maximum achievable image quality. Any values above that would not necessarily improve the accuracy of the results, while requiring proportionally more time to complete the scan and the 3D image reconstruction.

The x-rays are produced through ionizing radiation, generated by a current passing through a tungsten filament. The voltage and the current can be altered according to the required power to properly scan the desired material and geometry. The x-ray tube is provided by X-Ray Worx, model XWT-300-THE Plus, whose technical data can be found in Table 3.1:

Table 3.1 Technical data of the x-ray source.

Maximum voltage $[kV]$	300
Minimum voltage $[kV]$	50
Maximum current $[\mu A]$	1000
Minimum current $[\mu A]$	50

Maximum power, target $[W]$	50
JIMA resolution $[\mu m]$	3.0
Tube type	Transmission
Target type	High energy
Target material	Tungsten

Table 3.1 shows the ranges for the voltage and current that can be set for the scan, while the theoretical resulting power should be the multiplication of those values. The target power, however, is the measured power actually leaving the tube, after accounting for losses. Meanwhile, the JIMA (Japan Inspection Instruments Manufacturer's Association) resolution is the maximum achievable resolution by the tube.

3.2. 3D Digital Image Reconstruction and Analysis

Once the projections have all been acquired, the software VGSTUDIO MAX 3.5 is used for digital image reconstruction and defect analysis. Since the software controlling the micro-CT scanner does not provide any preprocessing of the acquired projections, they are imported into VGSTUDIO CT-reconstruction module in their original form. The raw projections have their grayscale values reversed with respect to the reconstructed image, meaning that the projection background is bright while darker regions signify larger material thicknesses and/or densities.

The raw projections are preprocessed and then the reconstruction is calculated using Feldkamp's algorithm [1] for cone-beam CT scanners, resulting in the grayscale as explained in Section 2.1, with dark background and brighter pixels in correspondence to the most x-ray attenuating regions in the object. The reconstruction module only requires the projections themselves and information on the scanning setup – such as the scanner type, SOD and SDD – to generate the 3D digital image. The user can, however, configure several filter options, such as prioritizing algorithm quality over performance; specifying the type of high-pass filter focusing either on image sharpness or noise reduction; smoothing for reducing general noise; corrections for beam hardening, bad pixels, and artifacts.

The reconstructions conducted for the specimens tested in this work were all generated with the options prioritizing quality and sharpness, while avoiding all filters for noise reduction and other corrections, unless retained necessary. Since corrections and filtering of already acquired experimental data can potentially cause the loss of some information, by taking advantage of the non-destructive nature of the micro-CT, the scans can be redone adjusting the machine parameters and recalibrating it if necessary to improve the quality of the projections, i.e., to improve the accuracy of the raw experimental data, rather than trying to filter it through post-processing.

Fig. 3.3 shows the parameters defining the reconstruction algorithm and the information it requires, containing the options selected for all the scans presented in this work, with exception of the two distances – source-object (SOD) and source-detector (SDD) – that are compiled accordingly for each specimen. The projection handling should be chosen as logarithmization and filtered reconstruction (back projection), required by the use of raw projections from the scanner, and the FBP (filtered back projection) mode is ramp, which prioritizes sharpness rather than noise reduction.

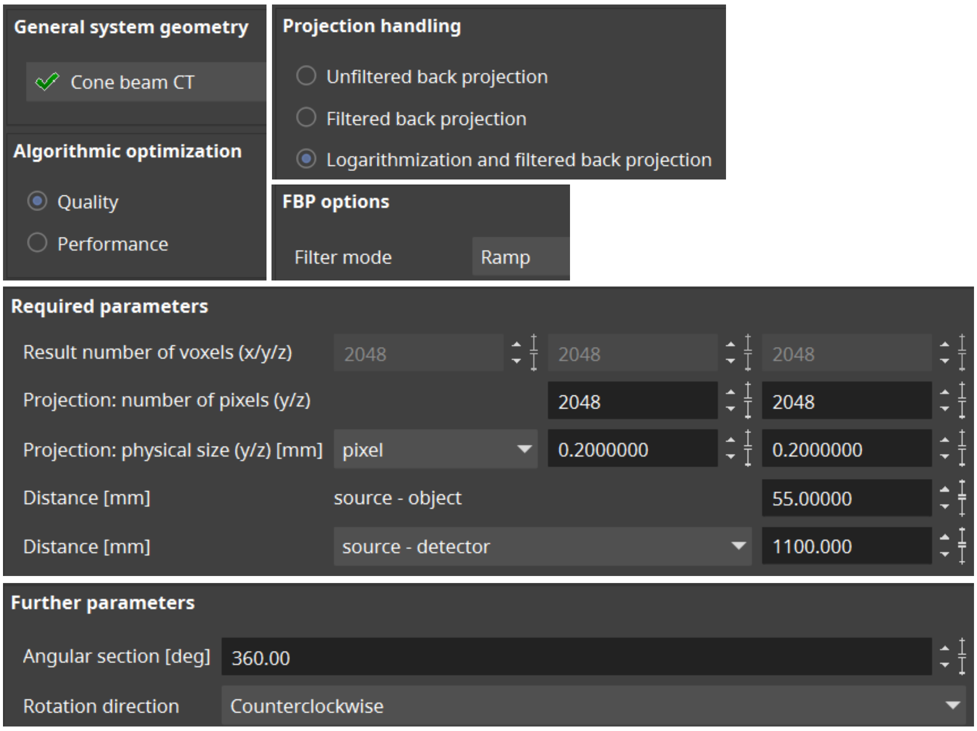

General system geometry
✓ Cone beam CT

Algorithmic optimization
● Quality
○ Performance

Projection handling
○ Unfiltered back projection
○ Filtered back projection
● Logarithmization and filtered back projection

FBP options
Filter mode: Ramp

Required parameters
Result number of voxels (x/y/z): 2048 / 2048 / 2048
Projection: number of pixels (y/z): 2048 / 2048
Projection: physical size (y/z) [mm]: pixel / 0.2000000 / 0.2000000
Distance [mm]: source - object: 55.00000
Distance [mm]: source - detector: 1100.000

Further parameters
Angular section [deg]: 360.00
Rotation direction: Counterclockwise

Figure 3.3 CT reconstruction module main required parameters.

Once the image is reconstructed, the object should be properly oriented according to the software cartesian axes, referred to as object registration by the software. In this case, the longitudinal axis of all specimens is made to coincide with VGSTUDIO z-axis, to keep the consistency with the adopted global coordinate system. Afterwards, the object surface is determined through the function surface determination, which serves the purpose of defining the boundary between object and background, used later to establish the region of interest (ROI) to be analyzed for defects.

Finally, the porosity/inclusion analysis module is used to search for internal imperfections, treated as either voids or inclusions, and to calculate analysis results providing information on the individual defects and on overall statistical data. The generated report, in the form of a datasheet, will contain information such as size (volume, surface area, projected area on each of the three planes of the defined coordinate system, maximum diameter, equivalent diameter, and projected length on each cartesian axis), position, and its composing voxels statistics (minimum, maximum, mean gray values and their deviation).

This module algorithm works by checking whether each voxel is part of a defect, creating groups of connected voxels (or clusters). Each of these groups is then evaluated to verify if they meet the analysis criteria specified by the user. Specifically, the algorithm VGDefX is applied in this work due to its capacity of accurately evaluating the presence of imperfections situated within noisy regions or connected to the surrounding air (in proximity to the determined surface). Moreover, this algorithm allows the specification of several additional probability criteria used in the defects detection.

The analysis mode can be set as either void – to search for clusters of voxels with lower grey values – or inclusion – to search for those with higher grey values. The material definition options define the ROI and the gray values maximum threshold, in case of void mode, that should be included in the analysis, so as to exclude the voxels that have too high gray values to be voids, reducing calculation time.

The analysis parameters define how the algorithm will decide if each cluster of voxels is a material imperfection. The noise reduction option inside the defect analysis module does not alter the raw data but affects how each cluster seed point is chosen. For all the analyses conducted in this work, the option median filtering is selected, which means that the grey value of each voxel is replaced with the median of the neighboring values, to avoid picking voxels that differ too much from the median as seed points, which should help avoid the influence of pixel errors in the defects detection.

The probability criterion specifies the method according to which the defects will be grown from their seed points, and a positive probability value, indicating the certainty of that cluster of voxels being an actual defect, will be calculated. In this work, the custom criterion is adopted, since it enables the application of probability factors, which give different weights to a list of aspects and can be adapted to improve the results accuracy for each specific scan.

Meanwhile, the options defining analysis area and surface sealing decide on whether and how to consider the defects found in the vicinity of the material boundary. In the case of the specimens in this work, these options are chosen to consider even the imperfections connected to the surrounding air or cut by the ROI boundary, while avoiding the inaccurate detection of "defects" along the surface that are caused by partial voxel effect.

On the other hand, the options related to ignoring defects caused by CT artifacts are only able to change the probability values associated with each defect and not its shape or size like the previously explained parameters. In this case, it is highly recommended to activate the check neighborhood option, which will make the algorithm verify the similarity between the defect pattern with the vicinity, lowering the probability values for the imperfections that resemble the material. Finally, the filter result options do not affect the algorithm, they just serve the purpose of eliminating defects that have low probability and/or small size from the final report.

Once the calculation is finished, the module automatically generates the report datasheet and color-codes the defects according to the user desired configuration. For the analyzed specimens, the results of interest should be the defects positions, as calculated for their respective geometrical center, and the projected area on the xy-plane, corresponding to the specimens cross-section, as defined by Murakami [2] for a 3D crack of arbitrary shape.

3.3. Critical Defect Identification and Analysis

After the population of defects in the specimen interest volume is characterized, the UST test, of destructive nature, is conducted. As also pointed out in Section 1.2, the fracture surface of brittle materials is expected to show no evidence of which defect originated failure. Therefore, a different method to define the specimen critical defect was devised, requiring the rescan of the broken specimen after the ultrasonic test, specifically of its fracture surfaces and their vicinity.

These scans are then reconstructed and overlapped with the scan collected before the ultrasonic test, referred to as the original scan, allowing the identification of the defects present in the fracture zone, both those that were split by the fracture surface, and those contained in eventual missing fragments from the surface. Among these defects, the one with the largest projected area on the xy-plane, will be selected as the critical defect, used to define A_c. This procedure is illustrated by Fig. 3.4, showing the defect analysis on the original specimen 3D image, while indicating the identified critical defect, in this case an inclusion, on a 2D slice of the fracture surfaces.

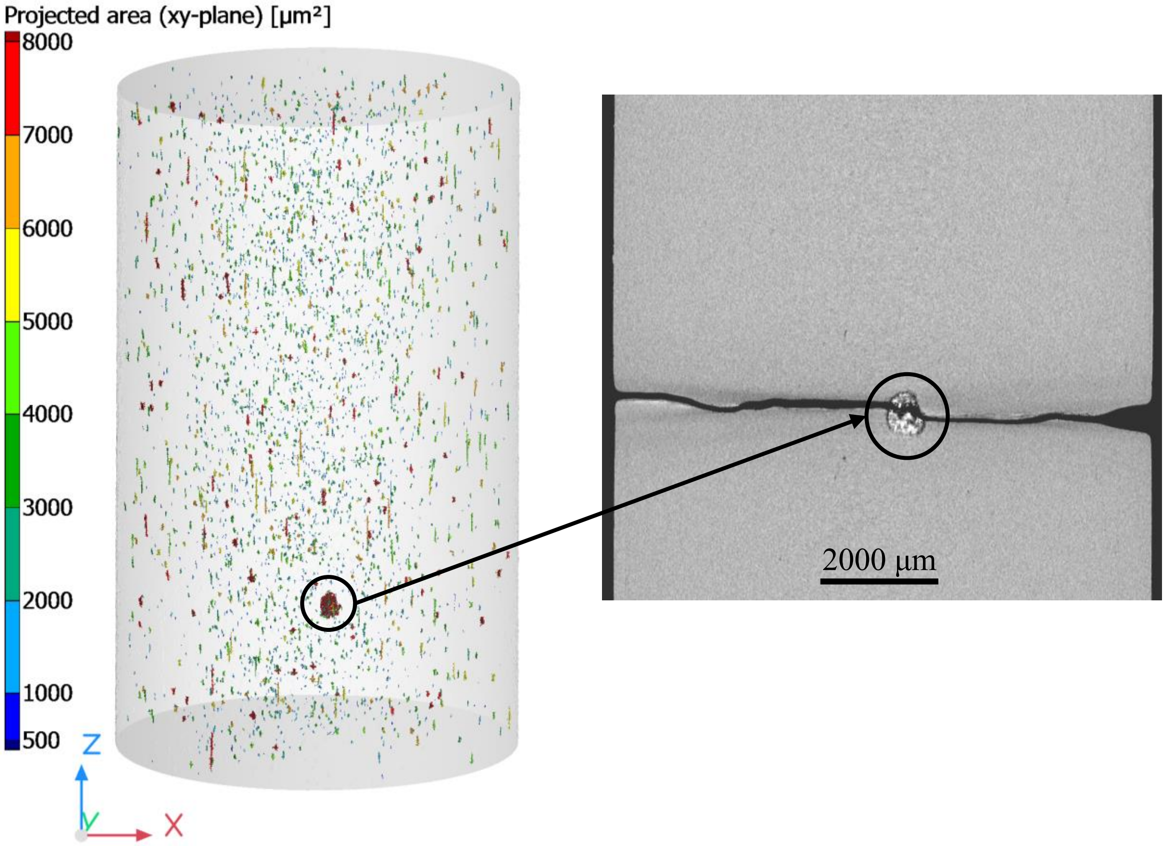

Figure 3.4 Alumina specimen illustrating the identified defects population and highlighting the critical defect on its fracture surface.

Once both quantities, i.e., the critical defect size and the specimen nominal tensile strength, are identified, a method to correlate them should be defined. In the literature, among the first formulations to depict the relation between flaw size and strength, there are Griffith's fracture energy, and Irwin's strain energy release rate, used to define the relation between crack size and fracture strength, culminating in the concept of stress intensity factor (SIF), or K [3]. In the study of brittle materials, formulations for SIFs predominantly refer to Irwin's mode I loading [4], called K_I, and follow the definition as in Eq. 3.2:

$$K_I = \mathrm{Y}\sigma\sqrt{a}, \tag{3.2}$$

with σ being the stress in the crack opening direction, a being a length value defining the crack size, and Y being a geometrical factor representing either a constant or a geometry function.

For instance, Murakami [2] defines the critical SIF as K_{Ic}, also called fracture toughness, for the 3D problem of a crack with arbitrary shape in an infinite body as:

$$K_{Ic} = 0.5 \cdot \sigma_f \sqrt{\pi \sqrt{A_c}}, \tag{3.3}$$

being A_c the area of the critical defect projected on the cross section, perpendicular to the crack opening direction and the normal fracture stress σ_f. The main advantage of Eq. 3.3 is its applicability to randomly shaped material flaws through its definition for the defect size as $a = \sqrt{A}$.

Furthermore, the geometrical factor Y introduces a flexibility to the calculation of K_{Ic}, in the sense that the same Y formulation could, within the same material, take into consideration the behavior of flaws with different shapes and sizes. Since Y can be empirically determined through the fitting of experimental data, K_{Ic}, in this case, is also applicable in the design of components, provided that the design values of the latter are kept consistent with the former respective empirical formulation.

Following these definitions, A_c is then used to calculate the stress intensity factors $K_{I,d}$ at failure for each tested specimen, defined according to Eq. 3.4:

$$K_{I,d} = \mathrm{C} \cdot \mathrm{Y} \cdot \sigma_f \sqrt{\sqrt{A_c}} \tag{3.4}$$

with Y calculated empirically through the data fitting of the experimental results for the entire set of specimens, as in Eq. 3.5:

$$\frac{1}{Y} = h\left(\frac{\sqrt{A_c}}{\emptyset}\right) = \sigma_f \sqrt{\sqrt{A_c}} \tag{3.5}$$

being $h\left(\frac{\sqrt{A_c}}{\emptyset}\right)$ a function of the critical defect size $\sqrt{A_c}$, and the specimen cross-section size $\emptyset$, corresponding to the diameter in circular cross-sections. Finally, the constant C is calculated as the mean of C_i, i.e., the stress intensity factor obtained according to Murakami's definition [2], being i the specimen number:

$$C_i = 0.5 \cdot \sigma_{f,i} \sqrt{\pi \sqrt{A_{c,i}}} \tag{3.6}$$

However, since Eq. 3.4 is only applicable to situations where the material body is infinite compared to the critical defect size, i.e., $\emptyset \gg \sqrt{A_c}$, the only specimens from the set whose C_i values are considered in the calculation of the mean are those that respect this condition.

With the empirical definition of C and Y, achieved through the analysis of the critical defects on each specimen as described, the formulation for $K_{I,d}$ can also be used to calculate and analyze the stress intensity factors of the whole population of defects identified through the CT-scans, only substituting $\sqrt{A_c}$ with the respective defect size $\sqrt{A}$, and σ_f with the nominal tensile stress σ at fracture on its position.

Since the accuracy of defect detection from micro-CT data can be influenced by several factors, e.g., the scanning parameters, the object geometry, the material, and the resolution, other studies in the literature compare results for porosity detection using microscopy, the Archimedes method, and micro-CT scanning [5-7]. According to these studies, it is reasonable to assume that internal defects from micro-CT data can be accurately identified if $\sqrt{A} \geq 4 \cdot r_{CT}$, with r_{CT} being the scanning resolution as defined by Eq. 2.1 in Section 2.1. However, considering the scanning resolution, the relative error on the measurement of smaller defects is expected to be considerably larger.

Furthermore, experimental results in [5] indicate that micro-CT porosity analysis data can produce slightly different results for the same material sample but with different geometries, since the particularities of the scanned geometry will increase or decrease the effect of phenomena such as x-ray beam hardening and scattering. Although the present work does conduct scans a second time on the same material with a different geometry, i.e., after the specimen is broken by the UST test and new fracture surfaces are generated, the resulting differences are not expected to be enough to prevent a reliable overlap of the fracture surfaces over the original specimen to identify the critical defect.

3.4. References

[1] L. A. Feldkamp, L. C. Davis, and J. W. Kress, “Practical cone-beam algorithm,” *J. Opt. Soc. Am.*, vol. 1, no. 6, pp. 612–619, 1984.

[2] Y. Murakami, *Theory of elasticity and stress concentration*. 2016. doi: 10.1002/9781119274063.

[3] S. W. Freiman and J. J. Mecholsky, *The Fracture of Brittle Materials: Testing and Analysis*. 2012. doi: 10.1002/9781118147757.

[4] G. R. Irwin, “Analysis of stresses and strains near the end of a crack traversing a plate,” *J. Appl. Mech.*, vol. 24, no. 3, pp. 361–364, 1957, doi: 10.1115/1.4011547.

[5] W. W. Wits, S. Carmignato, F. Zanini, and T. H. J. Vaneker, “Porosity testing methods for the quality assessment of selective laser melted parts,” *CIRP Ann. - Manuf. Technol.*, vol. 65, no. 1, pp. 201–204, 2016, doi: 10.1016/j.cirp.2016.04.054.

[6] L. Schild, L. Weiser, K. Höger, and G. Lanza, “Analyzing the error of Computed Tomography-based pore detection by using microscope images of matched cross-sections,” *Precis. Eng.*, vol. 81, pp. 192–206, 2023, doi: 10.1016/j.precisioneng.2023.01.013.

[7] J. A. Slotwinski, E. J. Garboczi, and K. M. Hebenstreit, “Porosity measurements and analysis for metal additive manufacturing process control,” *J. Res. Natl. Inst. Stand. Technol.*, vol. 119, pp. 494–528, 2014, doi: 10.6028/jres.119.019.

Chapter 4

4. Ultrasonic Tensile Test

In this chapter, the equipment, the testing configuration, and the data collection and analysis relative to the UST test are explained, including all the steps between the specimen design and the selection of test parameters, as well as the analysis of the raw experimental data.

4.1. Ultrasonic Testing Equipment

The ultrasonic testing machine is capable of operating with output frequencies f_{out} between $19.5\,kHz$ and $20.5\,kHz$, and it is composed by an ultrasonic generator, a piezoelectric transducer, and a booster, all provided by Branson Ultrasonics, as indicated in the schematics in Fig. 4.1a and presented in Fig. 4.1b through a picture. Fig. 4.1a also indicates the horn, to which the specimen is attached with adhesive, and the instruments used for data acquisition, the laser, the camera, and strain gauges placed on the horn, which will be further detailed in Section 4.1.

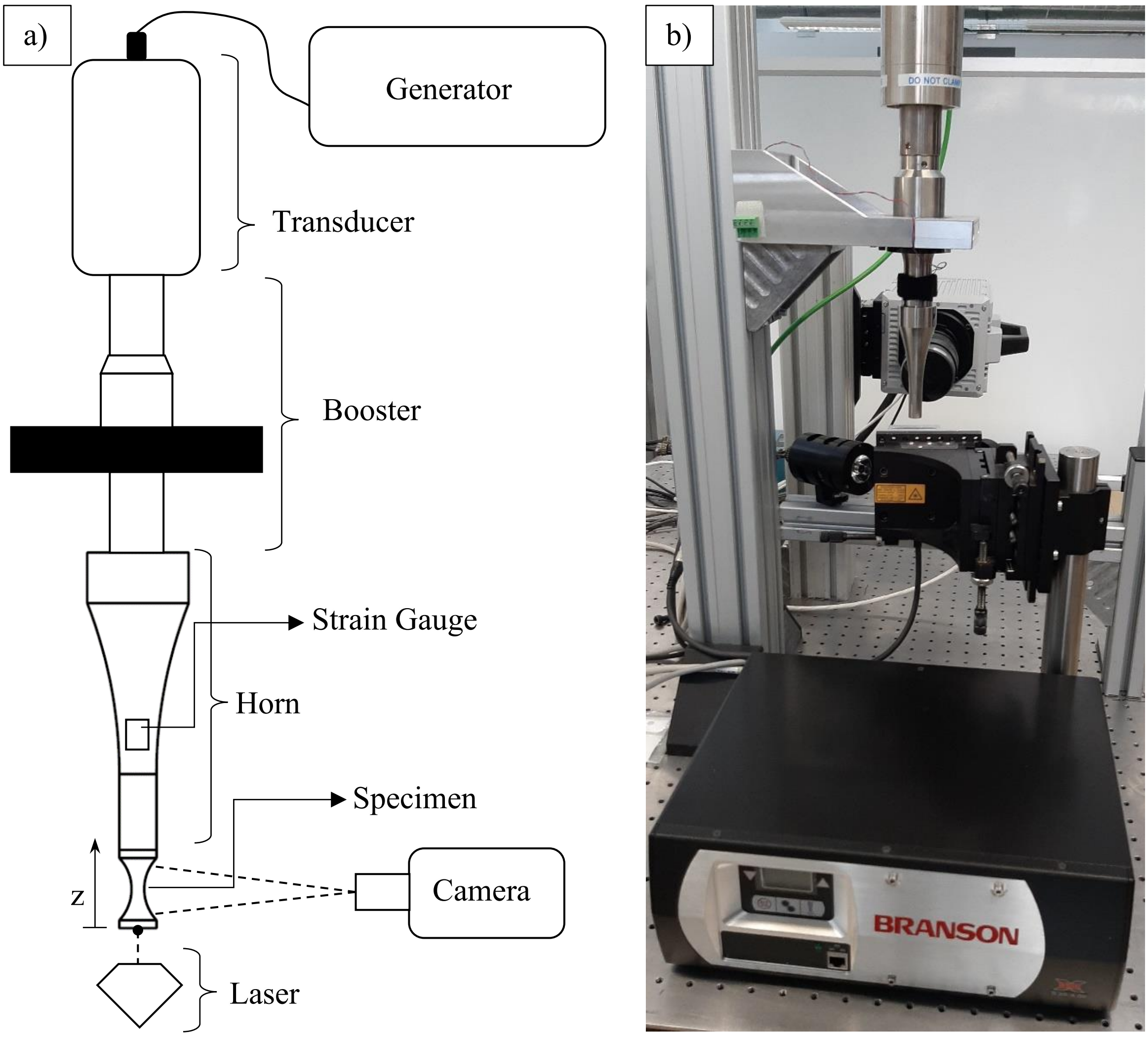

Figure 4.1 Ultrasonic testing equipment: (a) schematics indicating its main components, and (b) picture of the testing and measuring equipment.

The ultrasonic generator (model DCX S 20:4.00) is a commercial system for plastics welding, which is often adopted as power supply for VHCF tests [1]. The piezoelectric transducer is connected to the generator and, according to the supplier manual, guarantees a conversion of at least 90% of the received electrical energy into mechanical energy. At 100% conversion rate, it could theoretically produce a stable displacement amplitude between 1 μm and 11 μm.

The booster is rigidly attached to the transducer and amplifies the vibration amplitude by 2.5 times. The amplification is the ratio between the amplitude delivered to the horn and the one received from the transducer, meaning that, for this configuration, the maximum theoretical range of displacement amplitudes at the machine-horn interface is between $2.5\,\mu m$ and $27.5\,\mu m$.

The generator is set to linearly convert an external signal ranging from $1\,V$ to $10\,V$ into a percentage of its maximum operating power, respectively 10% and 100%. Taking into account the transducer conversion rate, and the device instabilities caused by operating on the range extremes, this translates, approximately, into a practical external signal to the generator ranging from $1.1\ V$ to $10\ V$, that can be linearly converted into a vibration amplitude between $1.1\ \mu m$ and $10\ \mu m$ by the transducer. The minimum external signal to be given to the machine is calculated according to the tensile stress that should be achieved to fracture the specimen, depending on its material and geometry.

Besides the vibration amplitude and frequency, the user is allowed to establish the ramp time, ranging from $1\ ms$ to $999\ ms$, i.e., the time the generator should take to go from the current vibration amplitude to the newly established one. Specifically, for the UST tests, it signifies the time needed for the machine to go from rest state to the set vibration amplitude, or the regime amplitude. Since, in this specific situation, ramp times below $10\ ms$ were observed to produce instabilities on the test, this value was adopted as the minimum stable ramp time, being applied to all the conducted tests.

The device is also capable of identifying the horn-specimen system natural frequency through a functionality called horn signature, provided it is comprised in the range between $19.5\ kHz$ and $20.5\ kHz$. Afterwards, the identified frequency can be used as the device output f_{out}. The vibrating components are suspended vertically to avoid flexural load due to the system weight, and they are clamped in correspondence of the booster nodal point (point of displacement amplitude equal to zero) using steel profiles as supporting structures, that can be seen in Fig. 4.1b.

4.2. Horn Design

The horn is a component that should be rigidly attached to the booster, as indicated in Fig. 4.1, and can be designed according to the type of ultrasonic tests one wishes to conduct, taking different geometries according to the stress configuration (uniaxial, biaxial, multiaxial) that is required on the specimen [2-5]. It also provides an amplification of the displacement received at its interface with the machine, delivering a higher displacement to the specimen, and therefore a higher stress, which is a necessary feature when the machine amplitude range is not enough to reach the required stress on the specimen.

From what was inferred in the previous sections, the horn and the specimens to be used in the UST test method must be designed in such a way that a few conditions are met. Firstly, the horn-specimen system must have its longitudinal natural frequency comprised in the range determined by the ultrasonic machine – in this case $19.5\ kHz$ and $20.5\ kHz$ – otherwise the machine will not start.

Furthermore, these two components, both individually and attached to each other, must have all the natural frequencies that are non-longitudinal sufficiently far from the machine range of frequencies to ensure that they do not enter a multiaxial state of resonance, which would consequently create a multiaxial stress state. Therefore, it was verified for all the mentioned components and system configurations that the only natural frequency comprised in the range between $18.5\ kHz$ and $21.5\ kHz$ is a longitudinal one.

Since the horn is projected to be used in multiple sets of tests, with different materials and specimen geometries, it is designed to have $20\ kHz$ as its longitudinal natural frequency by itself. This way, the machine is able to start with only the horn attached to it and no specimen, which is useful for calibration purposes.

Finally, the maximum stress amplitude on the horn must be guaranteed to be under the material fatigue limit considering the maximum amplitude output of the machine. The material in question is the Ti-6Al-4V alloy, which has a fatigue limit of around $410\ MPa$ [6]. Therefore, during design phase, it was established that the horn maximum attainable stress amplitude should be under $350\ MPa$.

For the design of both the horn and the specimen, the software Ansys Workbench, specifically the modules modal analysis and harmonic response, are used to verify that all the established requirements are properly respected. The former is used to verify all the frequency related constraints, while the latter is needed to ensure that the stress related constraints are followed. For the simulation, the necessary material properties are density, elastic modulus, and Poisson ratio for the Ti-6Al-4V alloy for the horn and the material that should be used on the specimen.

When either the horn or the specimen is simulated alone, the respective component remains free on both extremities. When simulating the whole system, a “bonded” connection between the horn and specimen is considered, while leaving the remaining extremity of either component free.

The horn design usually does not pose major limitations, the only critical point to be considered is the fatigue limit, since the Ti-6Al-4V alloy used can be easily machined within the required geometry and tolerance specifications. The simulation was thereafter executed using the material properties for Ti-6Al-4V as in Table 4.1. The properties were determined by analyzing horns that had been previously designed and produced for VHCF tests. The density was determined by measuring the mass and dividing by the calculated volume according to the design, the Poisson ratio follows the value in the supplier datasheet, while the elastic modulus is estimated through a modal analysis in Ansys by attempting to reproduce the longitudinal natural frequency of each horn as measured by the ultrasonic testing machine, i.e., through the horn signature feature.

Table 4.1 Material properties for Ti-6Al-4V required for the horn design.

Density (kg/m^3)	4485
Elastic modulus (GPa)	110
Poisson ratio	0.34

Fig. 4.2 shows the stress amplitudes of two horn designs considered in the experimental procedures conducted in this work. The stress distribution is calculated for when a harmonic displacement with amplitude $27.5\ \mu m$ at the machine-horn interface, corresponding to the testing device maximum theoretical output. The horn in Fig. 4.2a had been designed and produced prior to the research conducted in this thesis, being among the ones used for establishing the properties in Table 4.1. Its design is still presented in Fig. 4.2a, since it was used in several of the described experimental procedures. Its longitudinal natural frequency measured by the ultrasonic testing machine is $20160\ Hz$.

The response considered frequencies were $f_{n,h} = 20173\ Hz$ and $f_{n,h} = 19982\ Hz$ for the horns on Fig. 4.2a and Fig. 4.2b, respectively. Both horns are modeled as 3D solids, using tetrahedral elements with 10 nodes. The maximum normal stress amplitude in the longitudinal direction (z) should stay under the predetermined limit, being $303\ MPa$ and $325\ MPa$, for each of the respective components. Additionally, during the horn design procedure, it was verified that using smaller elements did not change the natural frequencies nor the presented stress maps.

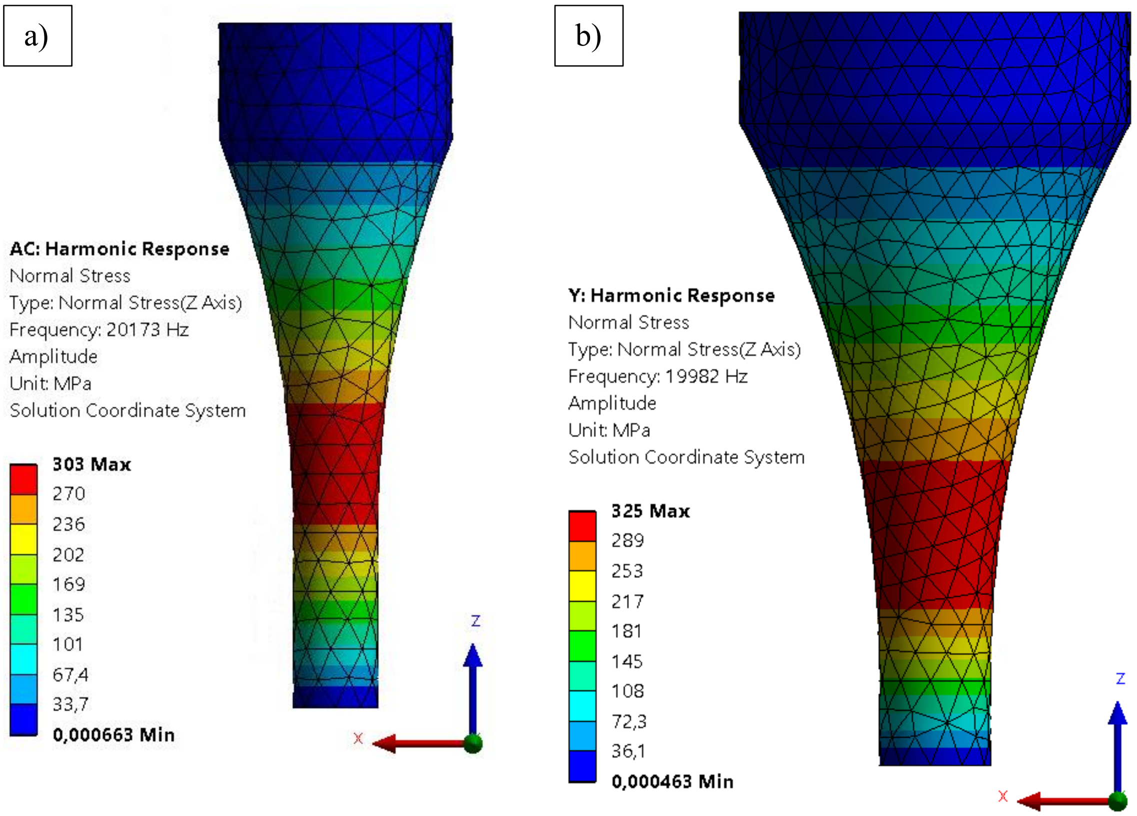

Figure 4.2 Maximum stress amplitude achievable on (a) horn A and (b) horn B designs during resonance.

The resulting amplification for each of the horns was also calculated considering the displacement amplitude at the horn-specimen interface divided by the imposed value at the machine-horn interface, resulting in 4.8 and 6.2 for Fig. 4.2a and Fig. 4.2b, respectively. The two designs are shown in the same order in Fig. 4.3a and Fig. 4.3b. Referring to the displacement amplitude applied to the specimen at the horn-specimen interface as the amplitude output A_{out}, and taking into account the amplitude range at the machine-horn interface defined in Section 4.1, it results in $13.2 \leq A_{out} \leq 120.0\ \mu m$ for horn A, and $17.0 \leq A_{out} \leq 155.0\ \mu m$ for horn B.

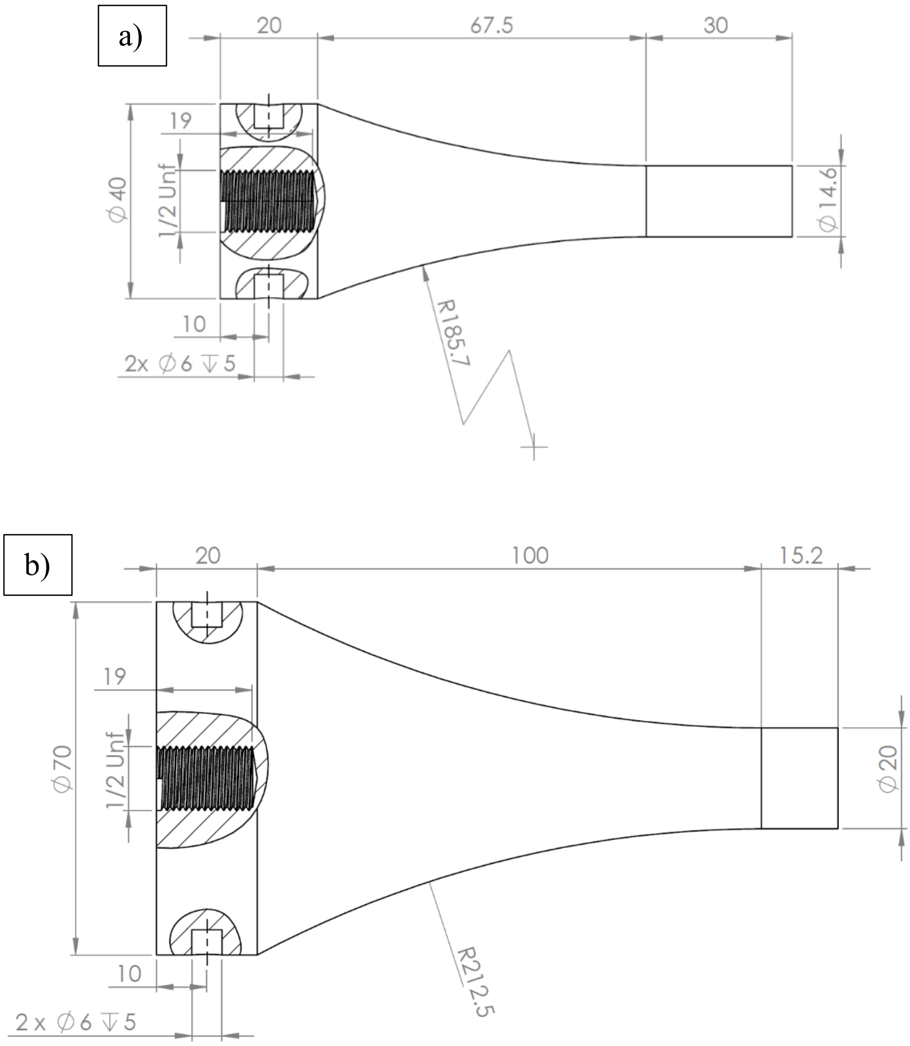

Figure 4.3 Final designs for (a) horn A and (b) horn B.

The first horn, from now on denominated horn A, with smaller amplification and mass, represents the standard component when a new experiment is being initially designed, since its smaller inertia lowers the risk that the specimen might be detached at the adhesive when the machine starts the movement. However, whenever either its amplification or its available area for contact with the specimen (with a diameter of $14.6\ mm$) is not sufficiently large to respect the requirements imposed by the specimen material and geometry, the second horn (horn B) could be alternatively adopted.

4.3. Specimen Design

The specimens design tends to be more complex than the horn, mostly because the required geometry often cannot be easily achieved, increasing substantially the experimental costs. Therefore, constant cross-section specimens are always the first type of geometry to be considered when designing an experiment with a new material.

Aside from the design constraints mentioned in Section 4.2, such as having a longitudinal natural frequency of $20\ kHz$ and avoiding non-longitudinal natural frequencies close to the machine range, the specimen design must follow a few specific requirements. Firstly, the horn-specimen interface must be at zero (or very close to zero) stress amplitude during the whole experiment, otherwise the adhesive could fail before the specimen, invalidating the corresponding test.

The next verification is that the specimen will be guaranteed to reach its tensile strength amplitude within the range of displacement amplitudes that can be achieved at the horn-specimen interface. If the constant cross-section specimen cannot respect this constraint, an hourglass specimen is designed, either with circular or rectangular cross-section. This amplification in strain is represented in Fig. 4.4, showing the two specimen geometries (constant cross-section and circular hourglass) in the same scale, for the same material submitted to the same vibration amplitude of the ultrasonic machine. The strain curves, also on the same scale, show that this hourglass specimen design manages to reach almost triple the strain when compared to the constant-section specimen.

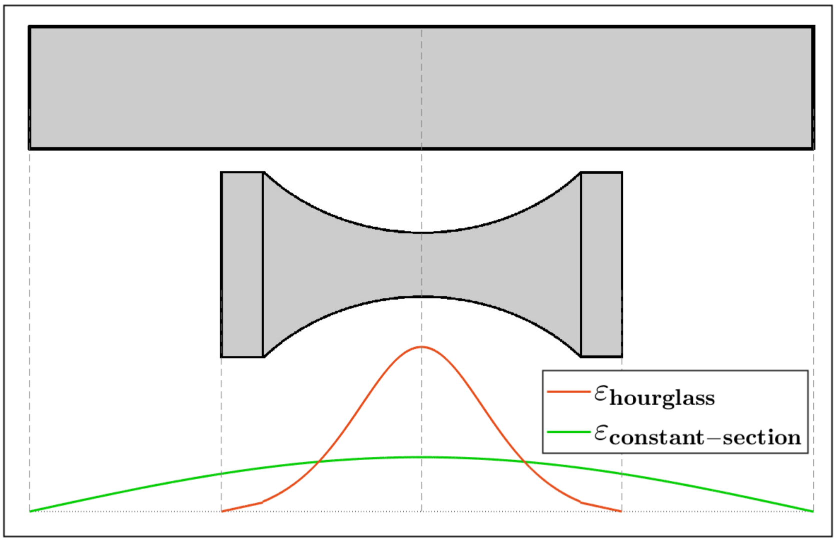

Figure 4.4 Comparison between the strains generated on constant-section and circular-section hourglass specimens of the same material under the same testing conditions.

As demonstrated by Eq. 2.2 from Section 2.2, the cross-section geometry and area do not influence the strain that can be reached on the constant cross-section specimen when considering only longitudinal resonance state. Therefore, when fracture strength cannot be reached, a design including cross-section variation, like the hourglass, is developed, especially for its capacity of significantly amplifying the resulting strain, while additionally reducing the volume of material needed.

As a final observation concerning the choice of materials, literature information was collected on their expected sensitivity to the strain rate resulting from the frequency of the cyclic load of the UST test, since it is observed that different metallic materials show a number of responses depending on the frequency of the conducted fatigue test, e.g., VHCF, and low and high cycle fatigue tests. While materials like titanium, austenitic steels, and nickel have low sensitivity to cyclic strain rate, results for ferritic steels, aluminum, and copper have shown hysteresis, cyclic hardening, and softening [7-9].

Generally, ceramic materials, such as alumina, silicon nitride and silicon carbide, tend to be modeled as linear-elastic, respectively presenting approximately the same elastic modulus independently of the strain rate. However, split Hopkinson pressure bar tests, both for Brazilian test and uniaxial compression configurations, have shown a tendency of the measured strength increasing with the strain rate, with many authors discussing the proper method to identify the failure instant in high strain rate tests due to the appearance of small cracks before complete fracture propagation [10-14].

Therefore, it would be reasonable to assume that the above-mentioned technical ceramics behave linear-elastically independently of the frequency of the cyclic load, with the material model and properties estimated through the UST being valid for most strain rates, including quasi-static applications. Meanwhile, the limited literature data about these materials being submitted to cyclic loads of any frequency, associated with novelty of the UST test, that tries to minimize fatigue damage mechanisms to estimate a strength value for an analogous quasi-static condition, prevents assumptions concerning load frequency sensitivity. However, on the upside, the strength measured through the UST method can be compared to that obtained through quasi-static tests for validation, while the failure instant is expected to be well-defined for all specimens, i.e., as the moment when fracture propagates enough to change the system natural frequency, interrupting the resonance condition, as observed in VHCF tests.

Similar observations and assumptions are made for graphene-based materials, such as graphite, the only exception being their tendency of presenting nonlinear behavior instead of linear-elastic as the above-mentioned technical ceramics. Indeed, literature for graphene-based materials shows viscoelastic, hyperelastic, and even plastic models being applied to simulate their behavior [15-18]. Fortunately, many of these material models incorporate rate-dependent terms that should properly consider nonlinear effects, such as creep, hysteresis, and stress relaxation, with the same property values estimated through the UST test being theoretically applicable to a wide range of strain rates, including quasi-static conditions.

4.3.1. Alumina 99.5% Specimens

The material parameters used in the alumina specimens design follow those provided in the supplier datasheet, according to Table 4.2, reporting both the catalog properties and additional values employed in the design of constant cross-section specimens. The elastic modulus adopted was 375 GPa due to the supplier datasheet reporting it as above 370 GPa, and after determining from other suppliers that this property value for alumina 99.5% would likely be below 400 GPa.

Table 4.2 Alumina properties considered for specimen design.

Supplier datasheet properties	
Density $[kg/m^3]$	3900
Elastic modulus $[GPa]$	> 370

Strength, 3-point bending $[MPa]$	490
Design parameters	
Elastic modulus $[GPa]$	375
Poisson ratio	0.26

Table 4.2 also shows the adopted Poisson ratio, not provided by this specific supplier, and calculated according to an average value observed in other suppliers datasheets, being any variations on this property of negligible consequence, since it only affects the torsional modes of resonance, being the longitudinal and flexural ones independent of it. Moreover, as long as the adopted Poisson ratio is a reasonable value for the material, the specimen torsional frequencies should also be kept outside the machine operating range.

Moreover, since increasing the elastic modulus also rises the longitudinal natural frequency, by selecting the specimen length in such a way that the horn-specimen system reaches at most $20.45\ kHz$ – i.e., under the maximum f_{out} of the testing device of $20.5\ kHz$ – in the scenario with the material having an elastic modulus of $400\ GPa$, it should guarantee the specimens' proper applicability to the ultrasonic test. This reasoning also avoids the prospect of needing to cut the specimens to increase their natural frequency, since reasonable material property variations, such as slightly lower elastic modulus and/or slightly higher density than those from catalog, would still not be enough to cause the system frequency to fall below the minimum f_{out} of $19.5\ kHz$. With its length defined through this method, the specimen by itself, with the parameters from Table 4.4, should have a longitudinal natural frequency $f_{n,s} = 20.01\ kHz$, which is shown in the harmonic response from Fig. 4.5.

The maximum achievable stress for this design, corresponding to the stress at the specimen central section when the machine is operating with horn A, at maximum output ($10\ V$), potentially generating $A_{out} = 120\ \mu m$, was also calculated, to guarantee specimen failure within the required constraints. Fig. 4.5 presents both the stress distribution on the specimen at this configuration, and the measurements of the final design.

The resulting specimen diameter of $10\ mm$ fits into horn A extremity of $14.6\ mm$, allowing the specimen extremity to be fully attached with adhesive and uniformly receive the horn vibration. This difference in diameter was adopted mainly for cost reduction, with the supplier already producing alumina rods of specific diameters, through extrusion and consecutive sintering, being that of $10\ mm$ the largest option, while the length could be freely chosen, since the rods can be cut as requested.

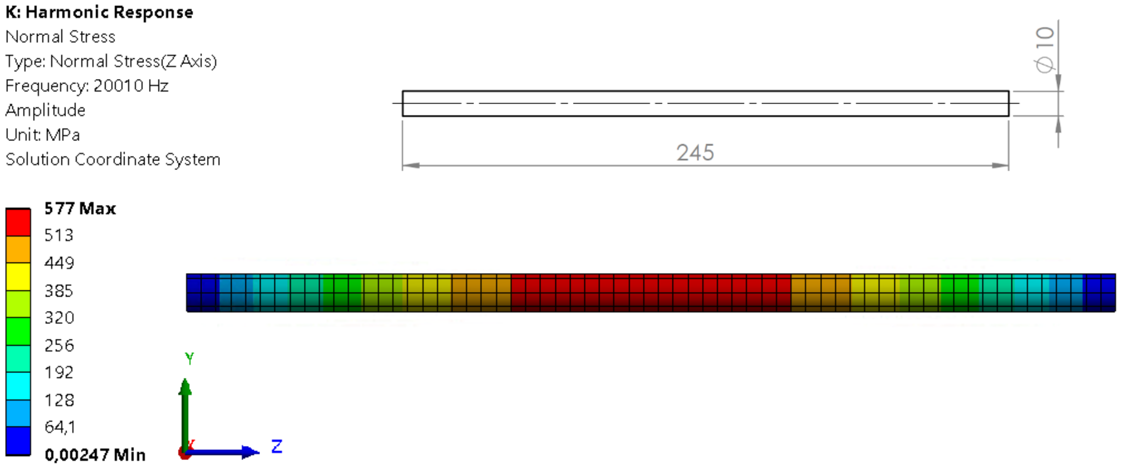

Figure 4.5 Alumina specimens design (measurements in $[mm]$), with FEM calculated stress for maximum machine output.

The simulation in Fig. 4.5 also shows that the maximum achievable stress of $577\ MPa$ is higher than the strength provided by the supplier for 3-point bending tests. Since, as pointed out in Chapter 1, these bending tests are characterized by low risk-volumes, reducing the possibility of a large defect being present in the high stress zone, it is expected that their measured strength values will be larger than those of a tensile test, even of the ultrasonic type.

Moreover, through Ansys Workbench, it was verified that the specimen other resonance modes were outside the machine operating range, as well as the previously established safety range. This ensures that the specimen will be submitted only to alternated tension and compression during the test.

4.3.2. Graphite R4550 Specimens

When designing these specimens, a few preliminary tests were conducted on graphite R4550 bars of constant square cross-section of $10 \times 10\ mm$. The bars had their dimensions and weight measured to calculate the material density, and their longitudinal natural frequency through Impulse Excitation Technique (IET) to obtain its elastic modulus. These properties are shown in Table 4.3, being used to design circular hourglass specimens following the constraints previously explained. The Poisson ratio was approximated as 0.16 according to datasheets from suppliers and the literature [15], following the same reasoning as in the alumina specimens designs.

Table 4.3 Graphite properties used in specimens design.

Properties measured from R4550 bars	
Density $[kg/m^3]$	1860
Elastic modulus $[GPa]$	10.9
Other design parameters	
Poisson ratio	0.16
Strength, 4-point bending $[MPa]$	61.2

R4550 specimens were also designed for the configuration using horn A, being the first considered design option the aforementioned square cross-section bars, shown in Fig. 4.6a, with the corresponding stress at maximum amplitude output, being $A_{out} = 120\ \mu m$. However, other studies suggest that graphite R4550 has a failure strength of $61.2\ MPa$ in 4-point bending tests [19], being too close to the ultrasonic device maximum achievable stress of $67.7\ MPa$ in this configuration. Therefore, hourglass specimens were developed, according to the design shown in Fig. 4.6b together with the maximum achievable stress of $201\ MPa$ when using the same testing configuration, following the behavior of the curves previously presented in Fig. 4.4. Both designs had their longitudinal natural frequencies, which are shown in their respective harmonic responses, aimed at $20.00\ kHz$, the center of the machine range.

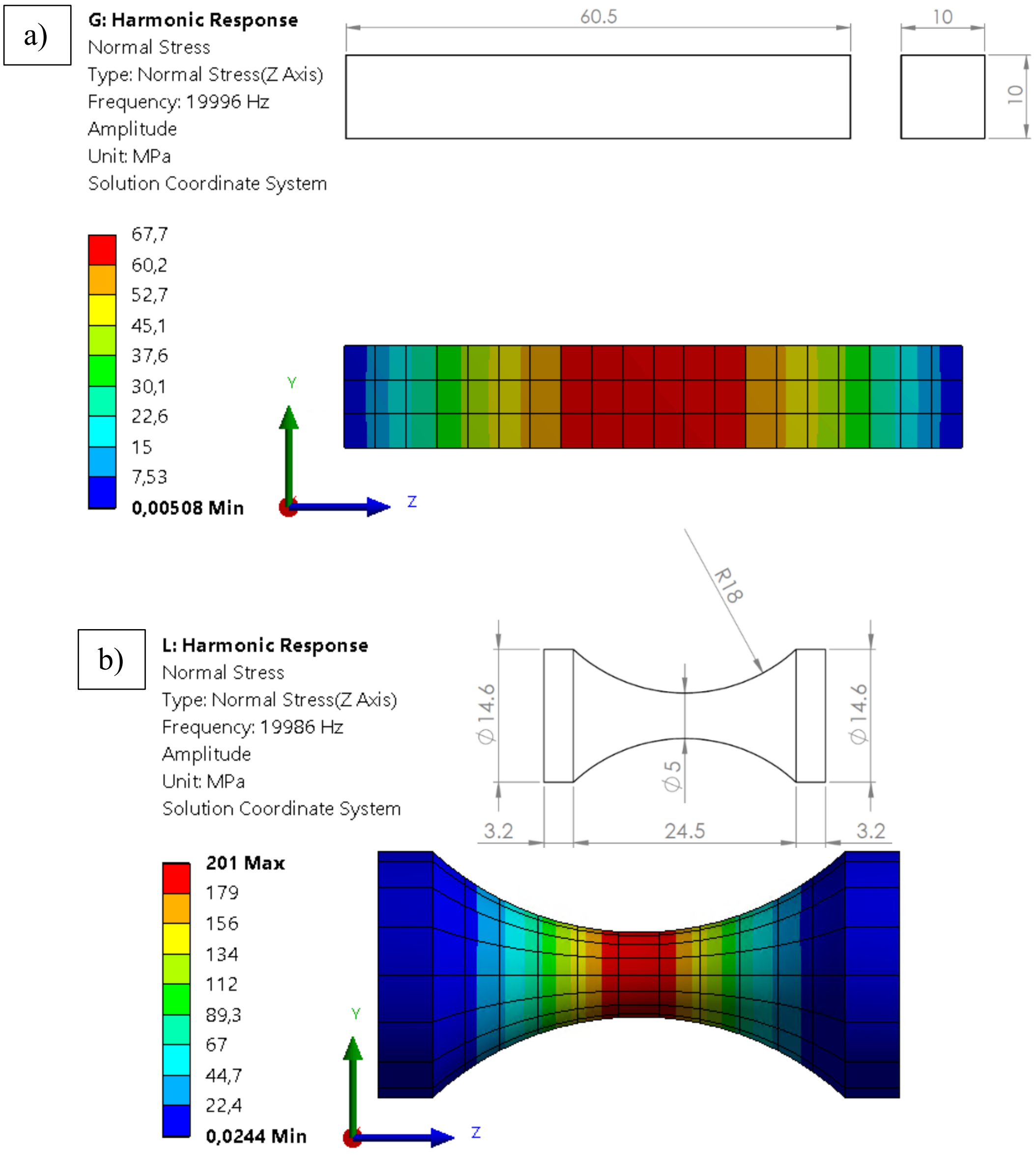

Figure 4.6 Graphite specimens design (measurements in [mm]*), with FEM calculated stress for maximum machine output, being (a) square constant-cross section, and (b) circular hourglass.*

The specimen in Fig. 4.6a could be easily obtained by cutting isostatically pressed graphite bars at the specified length. However, since some suppliers datasheets suggest that this material strength can surpass 80 MPa, depending on testing configuration, the more complex design was selected, which can be achieved due the high machinability of graphite R4550.

4.3.3. Specimens in Other Brittle Materials

Following the testing of alumina and graphite, specimens in other materials were designed, such as sintered silicon carbide, whose design was immediately adapted to the configuration with horn B, which allows a maximum displacement amplitude $A_{out} = 155\ \mu m$. The material properties were chosen according to a supplier datasheet, as presented in Table 4.4.

Table 4.4 Silicon carbide properties used in specimens design.

Supplier datasheet properties	
Density $[kg/m^3]$	> 3100
Elastic modulus $[GPa]$	400
Poisson ratio	0.14
Strength, 4-point bending $[MPa]$	> 400
Design parameters	
Density $[kg/m^3]$	3100

The density was chosen as the lowest possible value, since its increase corresponds to a decrease in the longitudinal natural frequency. Therefore, if it should fall below the machine range, it could be corrected by a slight reduction on the specimen length, both in the case of constant-section geometry, and hourglass – by equally shortening both of its extremities so it still remains symmetric. Using these parameters, the maximum achievable stress was calculated for the indicated testing configuration considering a constant-section and an hourglass geometry, both shown in Fig. 4.7, with their respective longitudinal natural frequencies applied to calculate the harmonic responses.

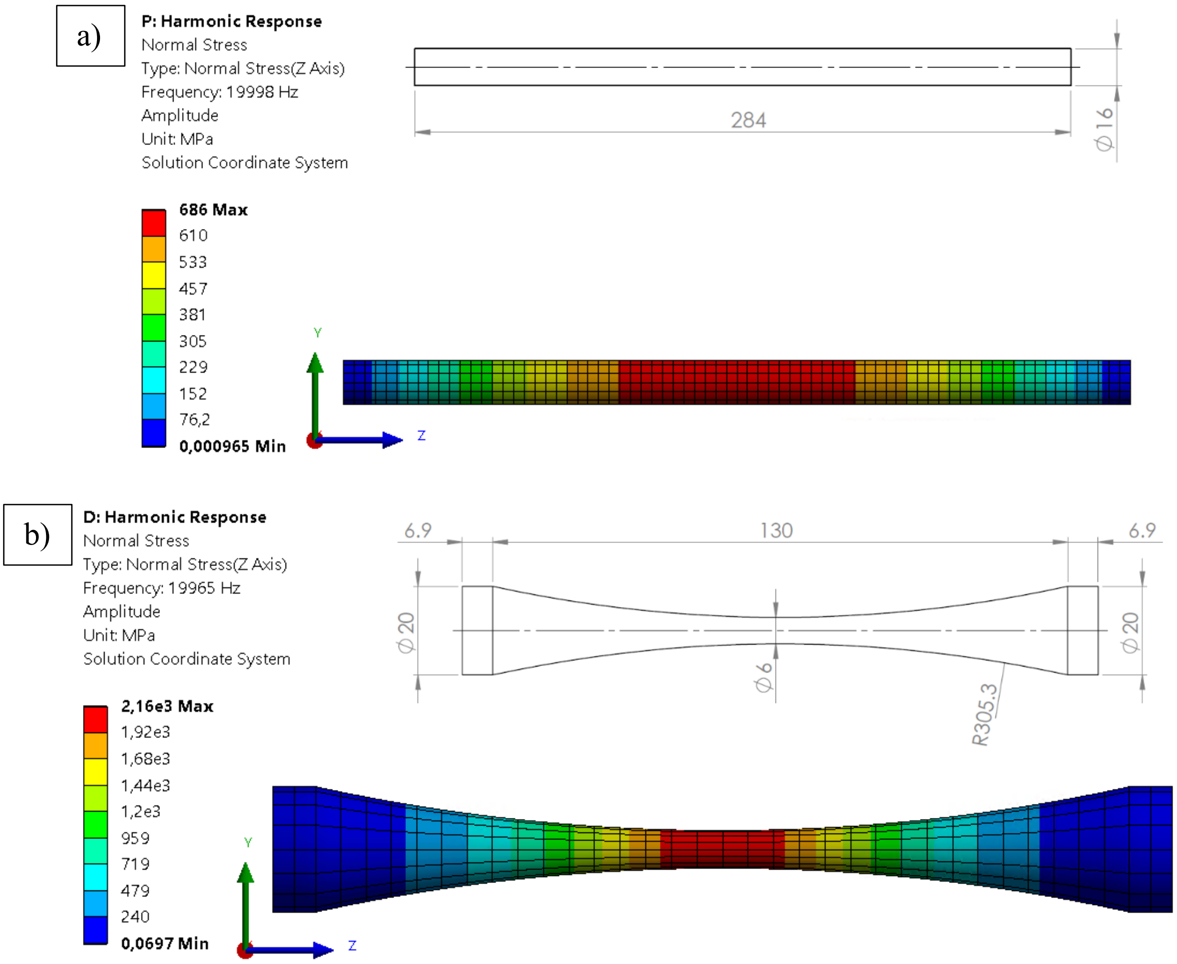

Figure 4.7 Silicon carbide specimens design (measurements in $[mm]$), with FEM calculated stress for maximum machine output, being (a) circular constant-cross section, and (b) circular hourglass.

Fig 4.7a shows the design with constant-section, which shows a maximum achievable stress (of 686 MPa) well above the catalog value for 4-point bending. The specimen diameter of 16 mm was adopted for being the largest size that could be fitted inside horn B diameter of 20 mm, while also keeping other natural modes of vibration at frequencies outside the established safety range of $[18.5, 21.5]$ kHz.

As a second option, to reduce the risk-volume, which should consequently reduce the time spent on defect characterization (on scanning, post-processing, and analysis), an hourglass geometry was also considered, as shown in Fig. 4.7b, allowing the maximum achievable stress to be increased to 2.16 GPa. This option, however, will probably increase production costs, since this material is not easily machinable.

Another material falling in a similar category was silicon nitride. However, in this case, the option of designing a constant cross-section specimen needed to be discarded, since the material properties presented in Table 4.5 were found to generate 602 MPa as the maximum achievable stress using horn B, which was similar to the calculated values considering the properties provided by other suppliers. Even considering the lower risk-volume involved in a 4-point bending test, the difference in the two stresses is too big to guarantee the proper conduction of the test.

Table 4.5 Silicon nitride properties used in specimens design.

Supplier datasheet properties	
Density $[kg/m^3]$	3290
Elastic modulus $[GPa]$	290
Poisson ratio	0.23
Strength, 4-point bending $[MPa]$	769

Therefore, a circular hourglass geometry was designed, as shown in Fig. 4.8, for horn B configuration, and a longitudinal natural frequency of 19.96 kHz, as applied to the stress calculated through the harmonic response. The measurements from the design show that the specimen fits perfectly on the interface with horn B, at 20 mm of diameter.

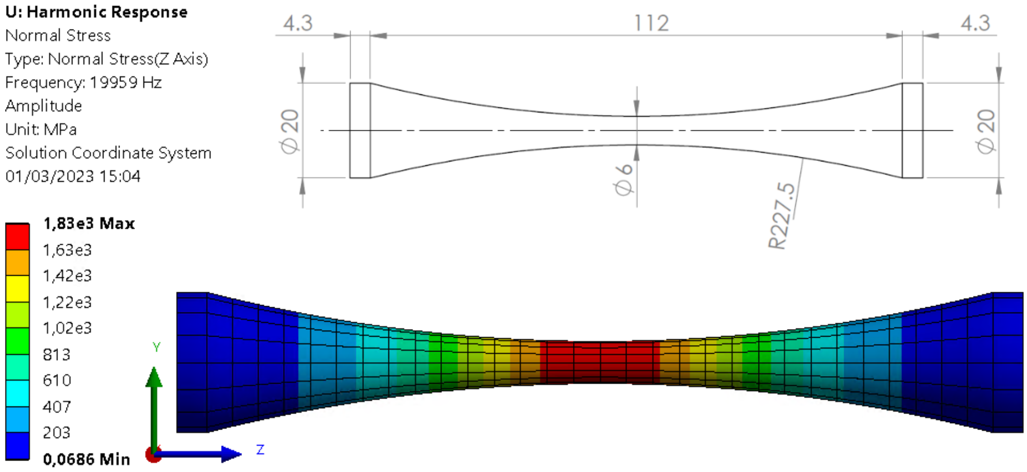

Figure 4.8 Silicon nitride specimens design (measurements in $[\mathrm{mm}]$*), with FEM calculated stress for maximum machine output.*

Finally, taking advantage of the advances in 3D ceramic printing technology of silicon carbide (SiSiC), a design for this material was developed, using the supplier properties as in Table 4.6. Since this fabrication process allows the printing of a wide variety of shapes, which are sintered afterwards, the hourglass geometries using horn A were immediately considered, since the additional amplification provided by these specimen geometries eliminate the need of using extreme configurations that could cause instabilities in the ultrasonic device during testing.

Table 4.6 3D-printed silicon carbide properties used in specimens design.

Supplier datasheet properties	
Density $[kg/m^3]$	2950
Elastic modulus $[GPa]$	340
Poisson ratio	0.18
Strength, 4-point bending $[MPa]$	220

For the mentioned configuration, a flat specimen was designed, as shown in Fig. 4.9, with the maximum achievable stress, in this case for $A_{out} = 120\ \mu m$, when its longitudinal natural frequency of 19.75 kHz is applied for the calculation of the stress caused by the harmonic response. The specimen extremities of $13 \times 6\ mm$ can be contained in the horn diameter of 14.6 mm, while other modes of vibration were verified to be outside the established safety range.

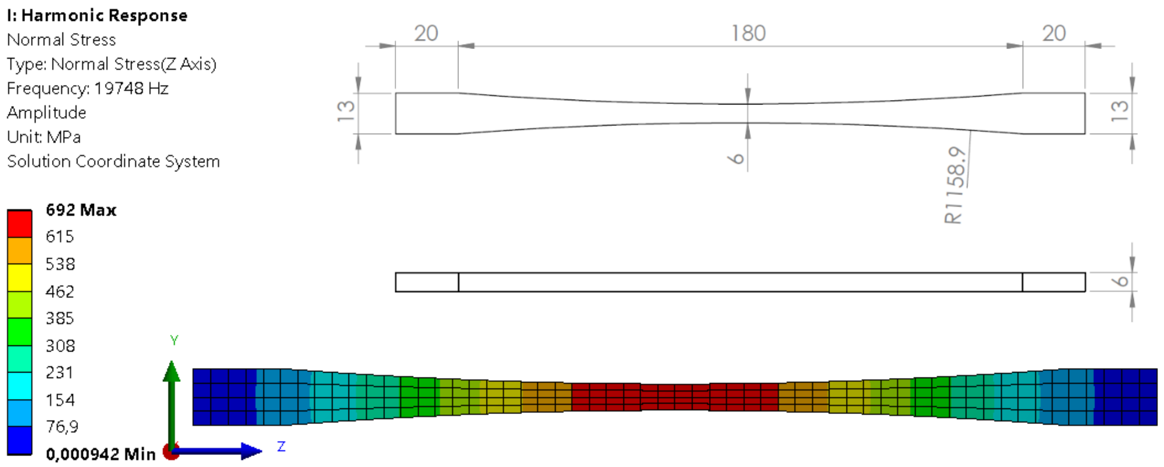

Figure 4.9 3D-printed silicon carbide specimens design (measurements in $[\mathrm{mm}]$), with FEM calculated stress for maximum machine output.

Two aspects concerning the fabrication process affected the design choices. Firstly, a reliable support for the specimen is required both during printing and to maintain its shape during sintering. Since this would be the first attempt at producing these kinds of specimens, the flat design could be printed horizontally without the need of additional supports, which would also considerably reduce the risk of bending its shape during sintering.

Secondly, the nature of this process makes it difficult to respect tight design tolerances without an additional finishing procedure after sintering. Since grinding of the full specimen should be avoided whenever possible, due to the material not being easily machinable, the design longitudinal natural frequency was aimed to be closer to the lower range of the ultrasonic device. As such, if the resulting specimen should fall below the required range, there still should be the possibility of increasing its frequency by equally shortening both of its extremities, as previously pointed out.

4.4. Measuring Equipment

The experimental data is measured mainly through two visual devices: a LK-G5001P laser from Keyence Corporation and a FASTCAM SA5 1000K-M1 high-speed camera from Photron. Both devices are indicated in Fig 4.1 in Section 4.1, while Fig. 4.10 illustrates the positioning of both devices relative to the specimen.

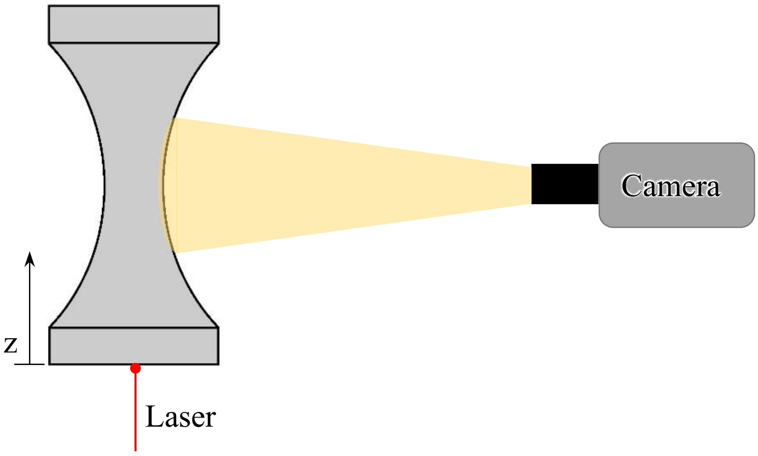

Figure 4.10 Schematic representation of the camera and the laser relative to the specimen.

As illustrated in Fig. 4.10, the laser always points at the specimen bottom close to its center and perpendicular to its surface for all UST tests. The laser can have a maximum of 392 kHz of sampling rate – value adopted for being capable of providing the maximum number of measurements per cycle – detecting the specimen free extremity displacement in z-direction and sending the measurement signal directly to the data acquisition system (which will be further described in Section 4.3).

Meanwhile, the camera is capable of reaching an acquisition rate of 1 $Mfps$. While aiming to strike a balance between reducing measurement errors while increasing the recorded region, the optimum recording window was found to be of 24×512 $pixels$, positioned with its larger side along the z-axis. While the 24 $pixels$ side, corresponding to a small recording length, it is positioned along the horizontal direction, in which the displacements are theoretically always zero.

This window allows an acquisition rate of 420 $kfps$, with external additional illumination by two single ultra-bright LED modules, model 900170, from Visual Instrumentation Corporation. This acquisition rate of a specimen that is vibrating at around 20 kHz will therefore grant the registration of around 21 photograms per cycle.

Moreover, the camera records a portion of the specimen lateral surface, having its exact position on the z-direction defined according to the specimen geometry. The goals when choosing which specimen zone should be registered are to increase the gathered information that could contribute to obtaining the material mechanical properties while reducing the measurement error, in this case connected to the camera resolution, by measuring zones with higher magnitudes of displacements.

The camera is generally set to acquire a length between 13 mm and 16 mm along the z-axis at its focal point. Meanwhile, specimens required in uniaxial ultrasonic testing are initially designed to have the displacement node at their center, as shown through Fig. 4.11a. As such, longer specimens, like those in alumina, have a zone around the node several times longer than the recordable one with low displacement amplitudes, in which case the recorded region should be selected near their free extremity, as shown in Fig. 4.11b. This positioning should provide the measurement of displacements far enough away from the horn, allowing the machine-imposed vibration to be influenced by almost the entire specimen, possibly providing a better representation of the material behavior.

As for the case of shorter specimens, like those in graphite, it is possible to position the camera to record a symmetrical region at the displacement node, as shown in Fig. 4.11c. This configuration should allow both the acquisition of large displacement amplitudes at the extremities of the recording window, while also acquiring data on the specimen displacement node, as well as spots with theoretically opposite phases of vibration, especially since graphite, as previously pointed out, has a tendency of presenting nonlinear behavior.

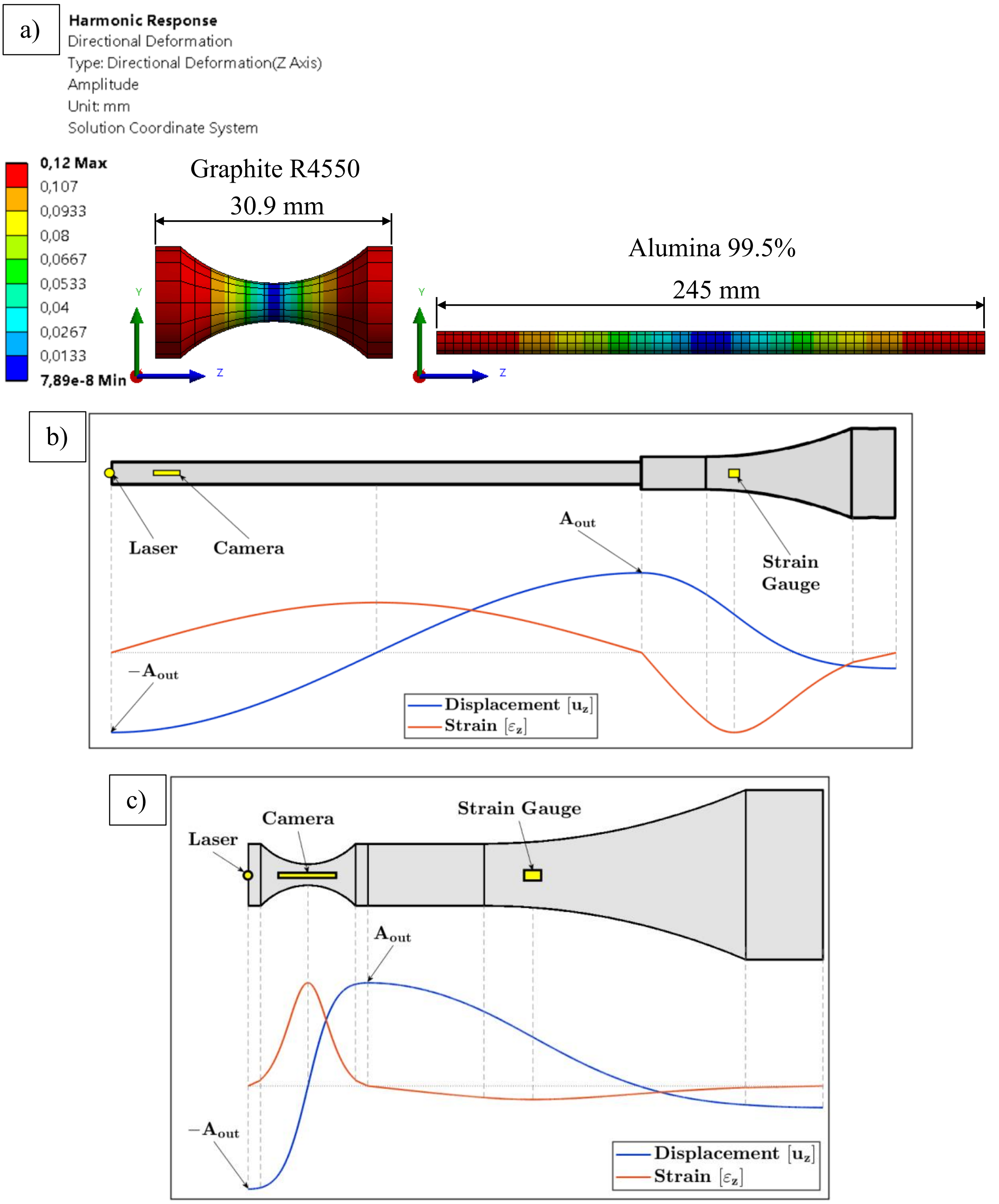

Figure 4.11 Comparison between theoretical responses for alumina and graphite specimens, being (a) numeric harmonic response displacement amplitude considering $A_{out} = 120\ \mu m$, *and analytical normalized displacement and strain amplitude curves on the horn-specimen system indicating the placement of the measuring devices for (b) the alumina specimens and (c) the graphite specimens.*

Both Fig. 4.11b and Fig. 4.11c show, respectively, the specimen and the horn in scale with each other, as well as with the recording length of the camera in z-direction, which corresponds to around 15 mm in both images. Each displacement and strain curve is normalized according to its own maximum respective value. Since both instances consider an ideal resonance condition, as the one presented in Section 2.2, where the natural frequencies of each specimen and the horn are the same as the machine output frequency, as well as all the considered materials being treated as linear-elastic, the displacement and strain amplitude curves also correspond to the instant of time t_k when the movement at the horn-specimen interface reaches a peak, being $u_{z,int}(t_k) = A_{out}$, while the movement at the free extremity of the specimen is at its valley, being $u_{z,f}(t_k) = -A_{out}$. In this moment, the specimens are entirely under tension and the horn under compression, being $\varepsilon_z \geq 0$ for the entire length of the specimens and $\varepsilon_z \leq 0$ for the entire length of the horn, with the central cross-sections of the specimens reaching the peak strain of the cycle for each respective geometry and material.

Additionally, both Fig. 4.11b and Fig. 4.11c show the laser positioned at the center of the free extremity of the specimen and the strain gauges placed in correspondence of the cross-section under maximum strain on the horn. By placing the strain gauges on the zone with the largest strain amplitude, the influence of measurement errors and noise should be reduced, with this position potentially being submitted to almost 3% of deformation at maximum machine output. Meanwhile, since the displacement amplitude in this zone is lower, being about 50% of A_{out}, the strain gauges are less likely to be detached due to inertia.

The camera is operated through the software Photron FASTCAM Viewer 3, which allows full camera control and image download via LAN connection to a computer. The software also allows the setup of external synchronization and trigger signals though input and output connectors that can link the camera directly to the data acquisition system. Given the high acquisition rate of the device, the images are only transferred to the computer when recording is finished, as such, the camera stores the images in a 64 GB internal buffered memory, i.e., by continuously acquiring a new image while erasing the oldest one, until it receives the signals that define when recording should start and stop. Therefore, the set images resolution and acquisition rate allow around 1 s of recording time before the camera memory gets full.

In addition to the mentioned measuring devices, other information is collected for verification purposes and support to the analysis, such as: camera signals that inform the frames recording timing, signals that identify the vibration amplitude and the start and end of the test. All the described data signals are gathered by the data acquisition system, the only exception being the actual recorded images, which are transferred directly to the computer once the test is over.

4.5. Control and Data Acquisition Device

The experiment is controlled by a National Instruments X series multifunction data acquisition (DAQ) device NI USB-6366, which is used to send the signals that govern the testing equipment and the data recording, while also receiving the signals that translate into the actual measurements of the experiment. The DAQ system is able to reach an acquisition rate of $2\ MHz$ and has an internal buffer that can store up to 62 million data points overall from up to 8 viable input channels, allowing a recording of at least $3.875\ s$ of data.

The DAQ device also issues output signals to the ultrasonic generator described in Section 4.1, turning it on and off at the start and end of the test, respectively, and informing the vibration amplitude that should be reached, while the frequency and the ramp time are set directly on the generator prior to the test. In the meanwhile, it also continuously receives signals from measuring devices and from the testing equipment, with all input channels being used, dedicated to the following: the laser, two strain gauges, the trigger signal, the generator on/off input, the generator amplitude output, the camera recording output, and the camera image exposure.

The ultrasonic frequency of vibration on the specimen requires a high acquisition rate to guarantee multiple points per cycle, therefore, the maximum achievable acquisition rate is adopted, being $2\ MHz$ for the DAQ system and $420\ kfps$ for the camera. Moreover, the high vibration frequency, associated with the method requirement of submitting the specimen to a reduced number of cycles, causes the test to last only for a few milliseconds. For this reason, to avoid the loss of information associated with simultaneous acquisition and transfer of data, which could amount to several cycles, both the DAQ system and the camera are set to continuously acquire signals and images, only transmitting the data to the computer once the test is finished. Since both devices store data temporarily on their respective buffered memories, once specimen failure is identified through the laser signal, a trigger is generated by the DAQ system to stop new data acquisition on both devices, and to transmit and save the data currently contained on their buffers to the computer.

4.6. Experiment Control Program

The control program is developed in National Instruments LabVIEW environment respecting the equipment settings as described in previous sections. The flow of this program can be seen in Fig. 4.12.

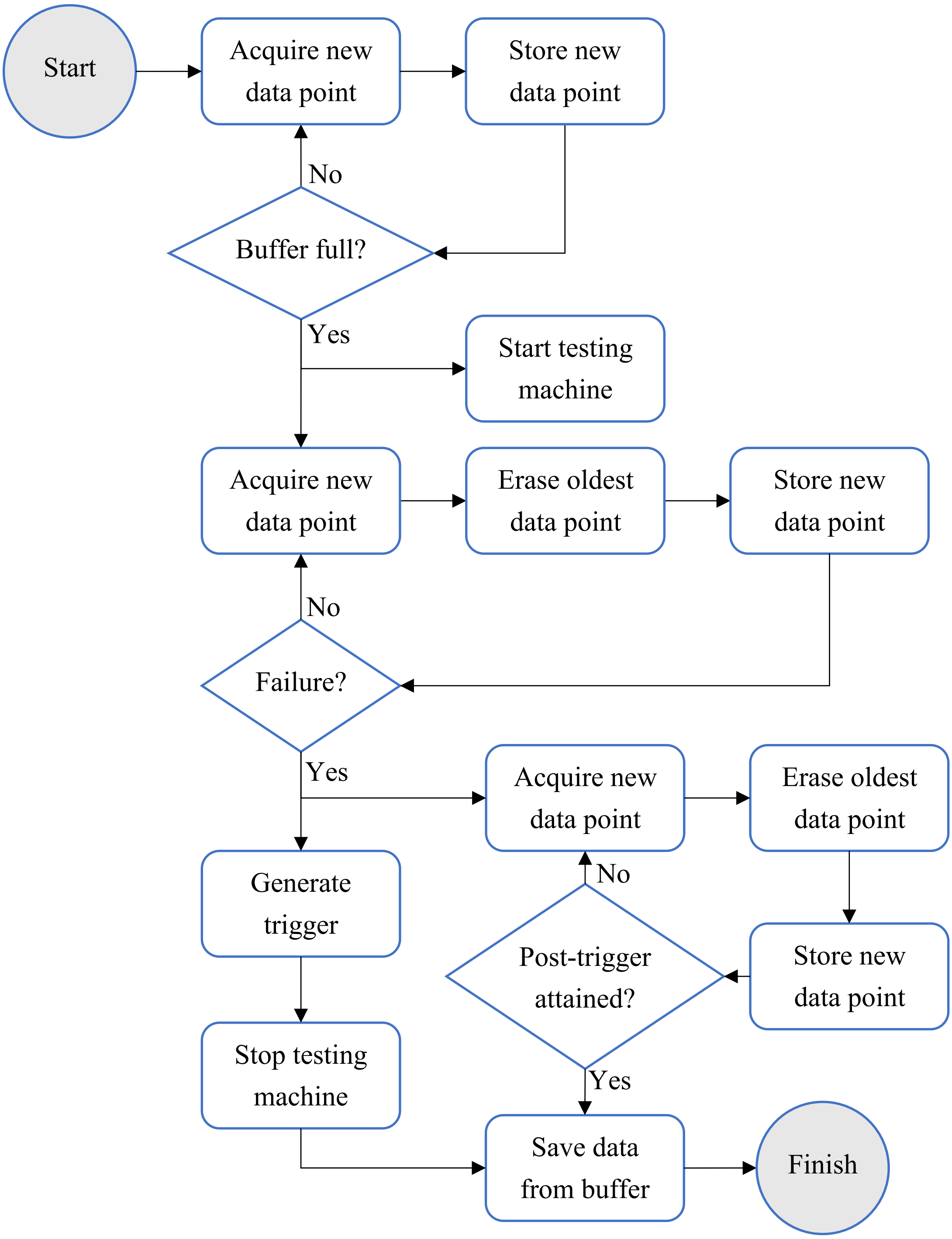

Figure 4.12 Flowchart of the program controlling the experiment and the data acquisition.

When the LabVIEW program is launched, the DAQ system data points acquisition immediately starts. After filling its own buffer, the system sends a signal to the ultrasonic generator to start the machine, while new data points are continuously acquired and older ones erased, until the specimen failure is detected. Once this happens, a trigger is generated and sent to the camera, and the machine is stopped. At the same time, a user-defined number of post-trigger data points is acquired before acquisition stops altogether, sending and saving all the recorded data to the computer.

Failure is defined in the program through the laser, by identifying when the signal for displacement of the specimen free extremity leaves the acceptable range. This range is calculated from the maximum achievable amplitude plus a safety margin, which should account for measurement errors, differences between the machine set output and actual output, and any unforeseen and unconsidered tested material behavior. For example, if under certain testing conditions, it is calculated that the laser will measure a displacement that could potentially arrive at $50\,\mu m$ of amplitude at regime, once the detected signal leaves the $[-70, 70]\,\mu m$ window, it will mean that the specimen probably failed, having the detached piece fall, as illustrated in Fig. 4.13.

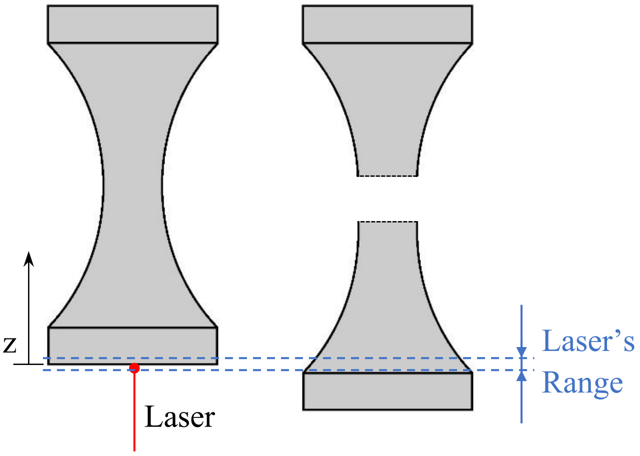

Figure 4.13 Illustration of the specimen extremity leaving the laser range when failure occurs.

As for the image acquisition aspect of the test, before launching the program, the camera is set to buffered recording while waiting for the end trigger from the DAQ system. Once the trigger signal is generated, the camera immediately stops the continuous recording, and keeps all the images currently in its memory, which are then sent to the computer, as shown in the flowchart in Fig. 4.14.

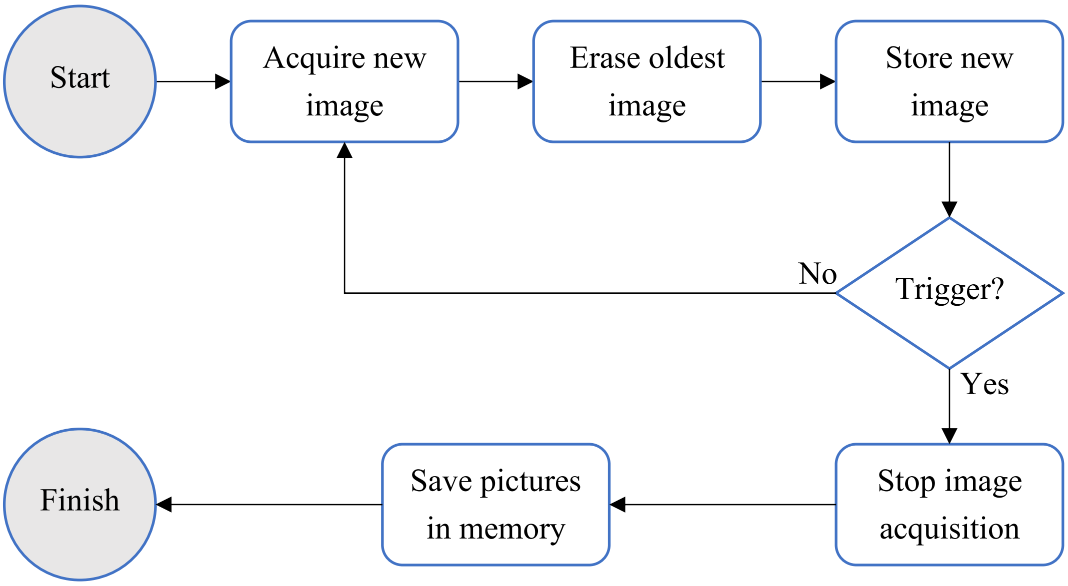

Figure 4.14 Flowchart of the camera acquisition control.

The trigger is set to the end of the test, when failure happens, due to the limited available recording time, since the high acquisition rates fill the camera and the DAQ system memories in around 1 s, and 4 s, respectively. With the configuration of an end trigger generated by failure, the acquisition instruments are guaranteed to record the last moments of test, when the vibration amplitude reaches its highest point, from which the specimen mechanical resistance should be obtained.

4.7. Ultrasonic Tensile Test Data Analysis

The analysis in this case means processing the raw experimental data to calculate the necessary information to be used in the material numerical parameter optimization, which will be further detailed in Chapter 5. The data in question is comprised by the camera images and the DAQ system measurements. The images are not particularly attached to a time frame, aside from the camera acquisition rate, and thus need to be synchronized with the remaining measurements. Meanwhile, the DAQ system records most of its channels in real time, the only exception being the laser, since it is the only measuring device that needs to have its signal preprocessed before being received by the DAQ system, which causes it to be delayed with respect to the other signals by around 2 ms.

Therefore, this data processing should follow a few steps in order. The first one is the tracking of the camera images to determine the specimen displacements between frames. Secondly, the obtained results for each frame are synchronized with the DAQ system real-time acquired data. Lastly, the laser is synchronized using the camera displacements as reference.

4.7.1. Image Tracking

Using Digital Image Correlation Engine (DICe), displacements along the specimen surface are calculated. To accomplish this, 20 ROIs to be tracked are defined in the reference image, i.e., one of the images before the machine start, when the specimen is sure to not have started moving yet. The tracking is conducted in all subsequent images until the last one, when failure already occurred. Fig. 4.15 illustrates this procedure, with the first/reference image and the 20 selected ROIs to be tracked.

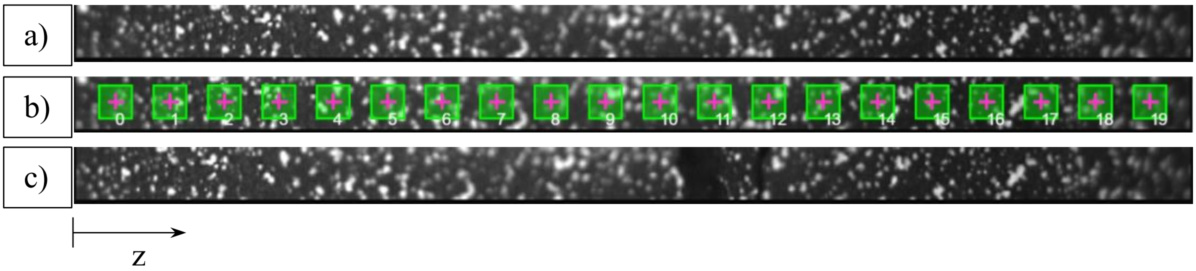

Figure 4.15 Tracking illustration, with (a) the reference image, (b) the reference image with the tracking ROIs defined, and (c) the last image, after failure happened.

As indicated by the coordinate system in Fig. 4.15, tracker number zero is the closest to the specimen free extremity. This particular illustration was taken from graphite tests, which, as explained in Section 4.4, have the camera recording window placed symmetrically at their center, allowing the fracture zone to be registered as shown in Fig. 4.15c. Moreover, the only result calculated through DICe were displacements in tracking analysis mode, since DIC algorithms are unable to calculate reliable results for strains due to the recording window resolution being too low, with only $24\ pixels$ in the cross-section direction.

Finally, it was verified for each test that the displacements calculated through the tracking in any direction other than z were approximately zero, all having levels around those of the measurement errors, mostly caused by noise. This guarantees that the specimens were only submitted to the uniaxial mode of resonance as designed.

4.7.2. Frame Synchronization

As pointed out before, the DAQ system records signals from the camera in real time. One of those signals, referred to as shutter, identifies the time during which the camera captures light before producing the image, generating simultaneously a $5\ V$ constant signal. For the speed of $420\ kfps$, the shutter time is defined as $1/1{,}000{,}000\ s$, as shown in Fig. 4.16. Once the trigger signal is received, the camera finishes the acquisition of the current image, and acquires one last image, called frame zero, which is discarded. Therefore, frame -1 is the last image in the final recording.

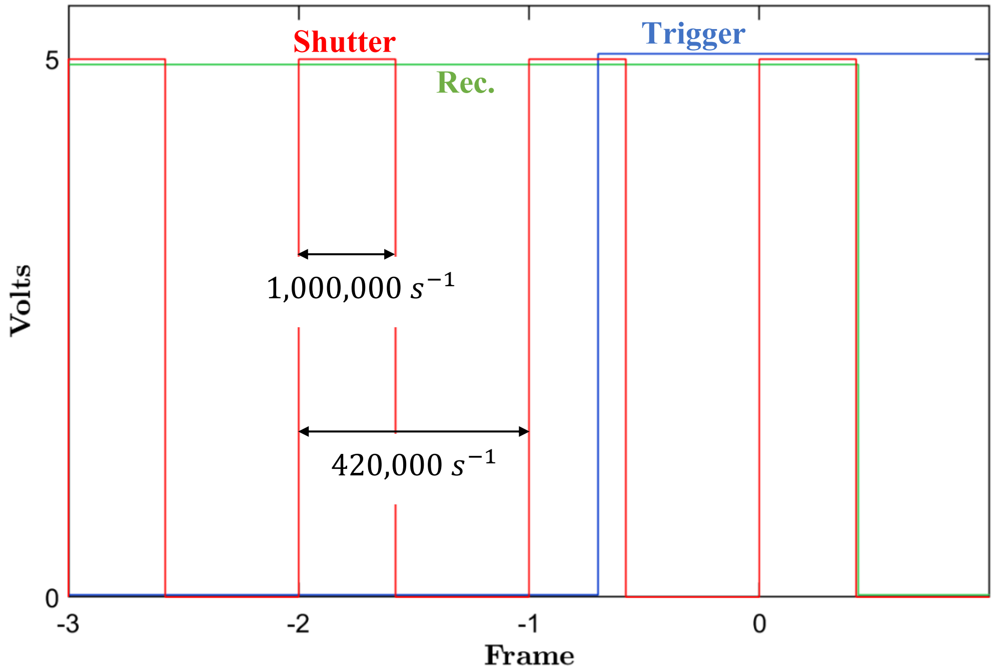

Figure 4.16 Schematics showing the last acquired frames in a test and the trigger and recording signals.

Since the shutter and trigger signals from Fig. 4.16 are timed by the DAQ system, each frame receives a time value that places them at the center of their respective $5\ V$ signal from the shutter, i.e., at the halfway point of the $1/1{,}000{,}000\ s$ time periods. Finally, to verify the synchronization, the frames timing is compared to the camera acquisition rate and recording signal. The latter, as opposed to the trigger signal form, should be constant at around $5\ V$ and then become zero once frame zero is acquired.

4.7.3. Laser Synchronization

As pointed out before, the timing associated with the laser signal by the DAQ system is delayed with respect to the remaining signals. To correct this issue, the displacements measured through the camera are used. Since at least part of the camera recording zone should correspond to the specimen portion to fall once failure happens, as it detaches from the horn-specimen system, it behaves like a falling rigid body, therefore, the displacements corresponding to the falling tracker ROIs should follow the exact same curve as the laser after a certain point, as illustrated by Fig. 4.17.

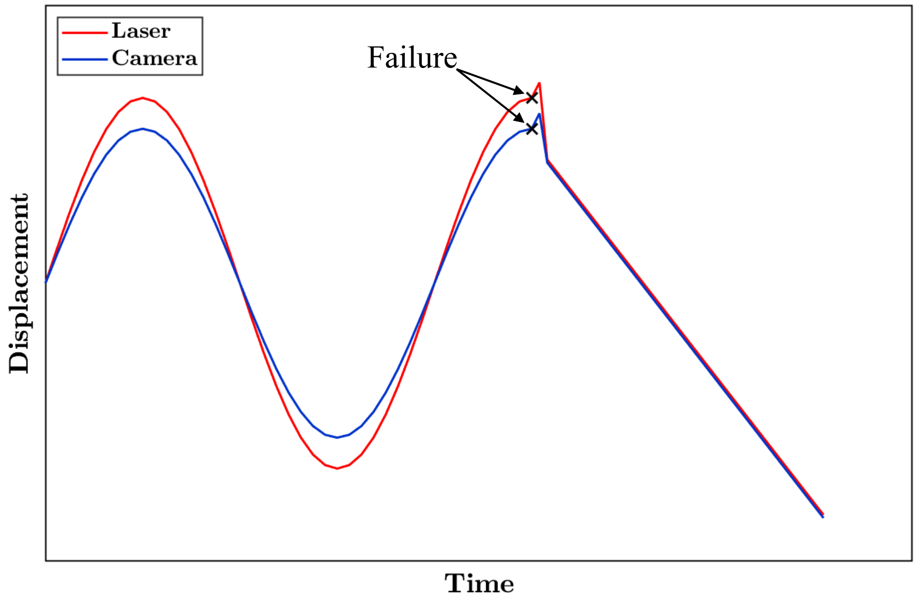

Figure 4.17 Illustration of the laser displacement curve after synchronization with the falling tracker ROIs.

For each test, the laser displacement curve is translated over the time axis until the displacements corresponding to the piece of specimen falling over the laser are overlapped with the tracker ROIs located on that same piece. Once the laser displacement curve is positioned as indicated in Fig. 4.17, the synchronization is done.

4.7.4. Cycles Counting

Finding a method for estimating the number of cycles for each test serves two purposes: i) providing evidence that their number is indeed low to support the hypothesis of negligible fatigue damage, and ii) defining the number of cycles for the estimated experimental displacement curve on the horn-specimen interface, referred to as $u_{z,int}(t)$, which is used as boundary condition for the numerical model of the test. Given the operating principles of the ultrasonic testing equipment, any relevant load only starts being applied to the specimen once resonance is achieved, which happens when the curves acquired by the measurement devices, also referred to as response curves, assume a frequency close enough to the set machine output f_{out}.

In all measurements, it was observed that once the machine receives the signal to start the test, the response curves take between 4 and 6 ms to start increasing towards the regime amplitude. During this initial period, the machine puts the system in resonance at a very low amplitude, whose magnitude is comparable to the signal noise. Indeed, during most of these $4-6\ ms$, the response curves are indistinguishable from any data recorded prior to the start signal, when the entire system is in rest condition. As soon as the response curves assume the output frequency of the machine (f_{out}), signifying that the system is in resonance, the amplitude starts ramping up to the regime amplitude.

To illustrate these observations, Fig. 4.18 shows the strain gauges response curve for one of the conducted tests, corresponding to the period between the start signal being sent to the testing machine and specimen failure happening. The portion of graph in red background represents the period before resonance is identified, being therefore excluded from the estimation of the number of cycles. A similar behavior is also observed for the displacement curves from the laser and the camera. Therefore, the number of cycles the specimen was subjected to until failure can potentially be estimated through the laser and each of the tracker ROIs as well.

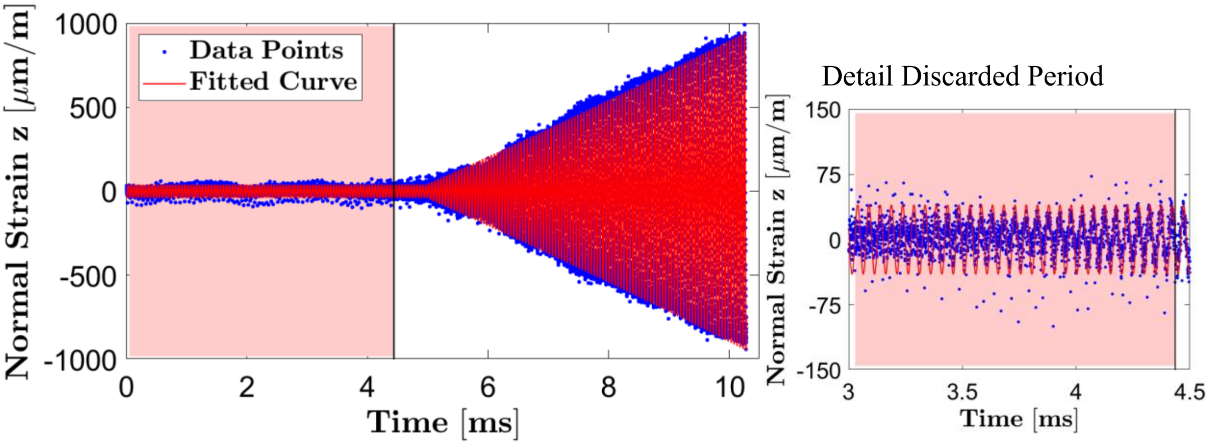

Figure 4.18 Normal strain in z measured on the horn, showing the period between the machine receiving the start signal and specimen failure being identified, highlighting with red background the period that is not considered for cycle counting.

Additionally, Fig. 4.18 presents a fitting curve of sinusoidal behavior obtained through a nonlinear least squares method in Matlab, which is further detailed in Section 5.1. The fitting is conducted only on the white background portion of the graph, with the frequency of the sinusoidal curve being imposed as equal to the machine output. For comparison purposes, a sinusoidal of frequency f_{out} and constant amplitude of value similar to the noise is extended over the entire discarded period, to highlight the strain gauge response curve assuming f_{out}, which can be observed on the zoomed detail shown on the right. Indeed, the data points only start taking a sinusoidal shape after the 3.5 ms mark, while they only assume a frequency similar to f_{out} nearly at the 4.5 ms mark.

Therefore, to define the instant from which the system assumes a resonance condition, an algorithm was devised to find the points that are likely peaks and valleys of each displacement or strain curve. This algorithm searches for a maximum and a minimum in each cycle, whose period is defined by f_{out}. The result of this search should look like the illustration in Fig. 4.19, which plots purely illustrative data to facilitate the visualization, being considerably less affected by noise than experimental data, as the one in Fig. 4.18. The points on Fig. 4.19 plotted over red background represent the data excluded from the fitting and the cycles counting procedure, according to the developed algorithm.

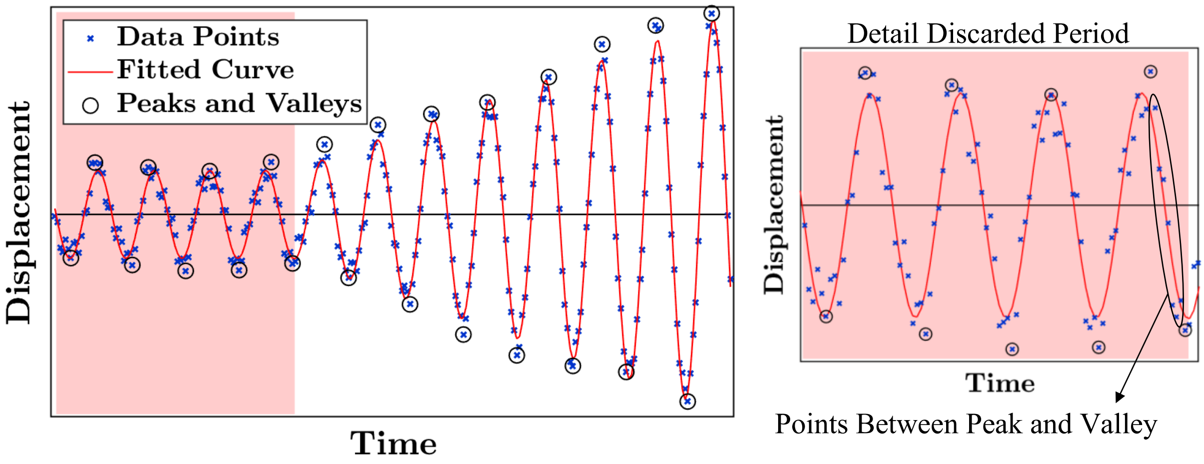

Figure 4.19 Illustration of the algorithm for identification of peaks and valleys, highlighting in red the portion of the curve that is not considered in cycles counting.

The algorithm evaluates from which point resonance was achieved by counting the data points between each peak and valley and comparing it to the theoretical value, that considers the output frequency and the respective measuring device acquisition rate. For example, the curve in Fig. 4.19 should have around 10 experimental points between each peak and valley, approximately the same value as the camera and the laser, by adding a reasonable tolerance, it is determined that the curve should have from 8 to 12 data points between each peak and valley. Whenever the number of points falls outside of this range, all the preceding data is taken out of consideration in the cycle counting, as indicated in Fig. 4.19 detail, where there are only 7 points between a peak and a valley. Finally, the number of valid peaks (n_{peaks}) and valid valleys ($n_{valleys}$) are used to calculate the number of cycles, rounded to the closest integer:

$$n_{cycles} = \frac{n_{peaks} + n_{valleys} - 1}{2} \tag{4.1}$$

Since the noise and errors level does not change as the amplitude increases, this algorithm was verified to always be able to account for the cycles above a certain amplitude, which corresponds to about $50\ \mu m/m$ for the strain gauges, $3\ \mu m$ for the camera, and $5\ \mu m$ for the laser. Therefore, the cycles counted by tracker ROIs near the node, such is the case for the graphite specimens, are often seen to measure less than half the number of cycles compared to the laser, the strain gauges, and the tracker ROIs far from the node. For this reason, the number of cycles of a test is defined as the largest obtained value among the laser, the strain gauges, and all the tracker ROIs, provided it does not differ too much from the values obtained in the remaining curves, in which case additional verification should be conducted. However, this was never an issue, since several curves for the same test always resulted in the same largest value for the number of cycles, even among the different measuring devices, e.g., laser, camera, and strain gauges, also indicating the reliability of the method in estimating the number of cycles.

4.8. References

[1] A. Tridello, D. S. Paolino, and M. Rossetto, "Ultrasonic VHCF tests on very large specimens with risk-volume up to 5000 mm^3," *Appl. Sci.*, vol. 10, no. 7, Apr. 2020, doi: 10.3390/app10072210.

[2] P. Ilie, X. Lesperance, and A. Ince, "Development of an ultrasonic fatigue testing system for gigacycle fatigue," *Mater. Des. Process. Commun.*, vol. 2, no. 6, Dec. 2020, doi: 10.1002/mdp2.120.

[3] D. Montalvão and A. Wren, "Redesigning axial-axial (biaxial) cruciform specimens for very high cycle fatigue ultrasonic testing machines," *Heliyon*, vol. 3, no. 11, Nov. 2017, doi: 10.1016/j.heliyon.2017.e00466.

[4] P. Costa, M. Vieira, L. Reis, A. Ribeiro, and M. de Freitas, "New specimen and horn design for combined tension and torsion ultrasonic fatigue testing in the very high cycle fatigue regime," *Int. J. Fatigue*, vol. 103, pp. 248–257, Oct. 2017, doi:

10.1016/j.ijfatigue.2017.05.022.

[5] U. Karr, R. Schuller, M. Fitzka, A. Denk, A. Strauss, and H. Mayer, “Very high cycle fatigue testing of concrete using ultrasonic cycling,” *Mater. Test.*, vol. 59, no. 5, pp. 438–444, May 2017, doi: 10.3139/120.111021.

[6] R. J. Morrissey and T. Nicholas, “Fatigue strength of Ti-6Al-4V at very long lives,” *Int. J. Fatigue*, vol. 27, no. 10–12, pp. 1608–1612, 2005, doi: 10.1016/j.ijfatigue.2005.07.009.

[7] M. Fitzka *et al.*, “Usability of ultrasonic frequency testing for rapid generation of high and very high cycle fatigue data,” *Materials (Basel).*, vol. 14, no. 9, 2021, doi: 10.3390/ma14092245.

[8] C. Lee, “Effect of strain rate on fatigue property of A356 aluminium casting alloys containing pre-existing micro-voids,” *Int. J. Fatigue*, vol. 131, 2020, doi: 10.1016/j.ijfatigue.2019.105368.

[9] P. Gabor, H. J. Maier, and I. Karaman, “Effect of strain rate on fatigue behavior of ultrafine grained copper,” *Fract. Nano Eng. Mater. Struct. - Proc. 16th Eur. Conf. Fract.*, pp. 209–210, 2006, doi: 10.1007/1-4020-4972-2_102.

[10] T. Jiao, Y. Li, K. T. Ramesh, and A. A. Wereszczak, “High Rate Response and Dynamic Failure of Structural Ceramics,” *Int. J. Appl. Ceram. Technol.*, vol. 1, no. 3, 2004.

[11] J. Zheng, H. Li, and J. D. Hogan, “Strain-rate-dependent tensile response of an alumina ceramic: Experiments and modeling,” *Int. J. Impact Eng.*, vol. 173, 2023, doi: 10.1016/j.ijimpeng.2022.104487.

[12] M. Ji, H. Li, J. Zheng, S. Yang, Z. Zaiemyekeh, and J. D. Hogan, “An experimental study on the strain-rate-dependent compressive and tensile response of an alumina ceramic,” *Ceram. Int.*, vol. 48, no. 19, pp. 28121–28134, 2022, doi: 10.1016/j.ceramint.2022.06.117.

[13] J. L. Zinszner, B. Erzar, and P. Forquin, “Strain rate sensitivity of the tensile strength of two silicon carbides: Experimental evidence and micromechanical modelling,” *Philos. Trans. R. Soc. A Math. Phys. Eng. Sci.*, vol. 375, no. 2085, 2017, doi: 10.1098/rsta.2016.0167.

[14] V. Sharma, S. Nemat-Nasser, and K. S. Vecchio, “Modeling the strain-rate dependence of fatigue life of hot-pressed silicon nitride,” *Mech. Mater.*, vol. 29, no. 3–4, pp. 253–

273, 1998, doi: 10.1016/S0167-6636(98)00024-6.

[15] L. Peroni, M. Scapin, F. Carra, and N. Mariani, “Investigation of dynamic fracture behavior of graphite,” *Key Eng. Mater.*, 2013, doi: 10.4028/www.scientific.net/KEM.569-570.103.

[16] P. Jaszak, “Modeling of the elastic properties of compressed expanded graphite - A material used in spiral wound gaskets,” *Int. J. Press. Vessel. Pip.*, vol. 187, Nov. 2020, doi: 10.1016/j.ijpvp.2020.104158.

[17] S. Vinod *et al.*, “Strain Rate Dependent Shear Plasticity in Graphite Oxide,” *Nano Lett.*, vol. 16, no. 2, pp. 1127–1131, 2016, doi: 10.1021/acs.nanolett.5b04346.

[18] M. F. Alzoubi, S. Khateeb, and S. Al-Hallaj, “Modeling of compression curves of phase change graphite composites using Maxwell and Kelvin models,” *J. Compos. Mater.*, vol. 50, no. 8, pp. 1123–1135, Apr. 2016, doi: 10.1177/0021998315588624.

[19] J. Guardia Valenzuela, “Optimisation graphite-matrix composites for collimators in the LHC upgrade,” Universidad Zaragoza, 2019.

Chapter 5

5. Numerical Modeling

Once the UST test raw data is processed and analyzed, the next step for the material characterization can be pursued, which is the development of a Finite Element Model (FEM) simulating the test and the specimen material, whose properties will be determined through an optimization aiming to reproduce the displacements experimentally measured. This procedure will be detailed in this chapter, being subdivided as: the model setup, comprising the definition of boundary conditions and a material model for the specimen on LS-DYNA after qualitative observation of the experimental displacement behavior; the determination of the optimization variables and objectives in LS-OPT; the extraction of the specimen stresses and strains in each finite element calculated for the respective ultrasonic test once the material properties are optimized.

5.1. FEM Definition

Since the horn was designed to behave linear-elastically within the entire range of the machine possible amplitude outputs, it was not included in the FEM, in which only the specimen will be involved and analyzed. Moreover, given that the specimens geometries tend to be simple, and an optimization, mainly of material parameters, is required, plane elements were selected to model it, which significantly lowers computational time. Specifically, for the cases of alumina and graphite specimens, both possessing circular cross-section, the axisymmetric formulation was applied.

As boundary conditions, one of the specimen extremities is free, while the other, at the horn-specimen interface, receives a displacement curve over time emulating the machine movement ramping up to the set output amplitude, here referred to as the boundary motion curve. This setup can be visualized in Fig. 5.1 through the LS-DYNA model of the hourglass graphite specimens with the boundary motion curve, i.e., the effective displacement being delivered to the specimen at the interface, indicated by $u_{z,int}(t) = \alpha \cdot g(t)$, as estimated for one of the conducted tests.

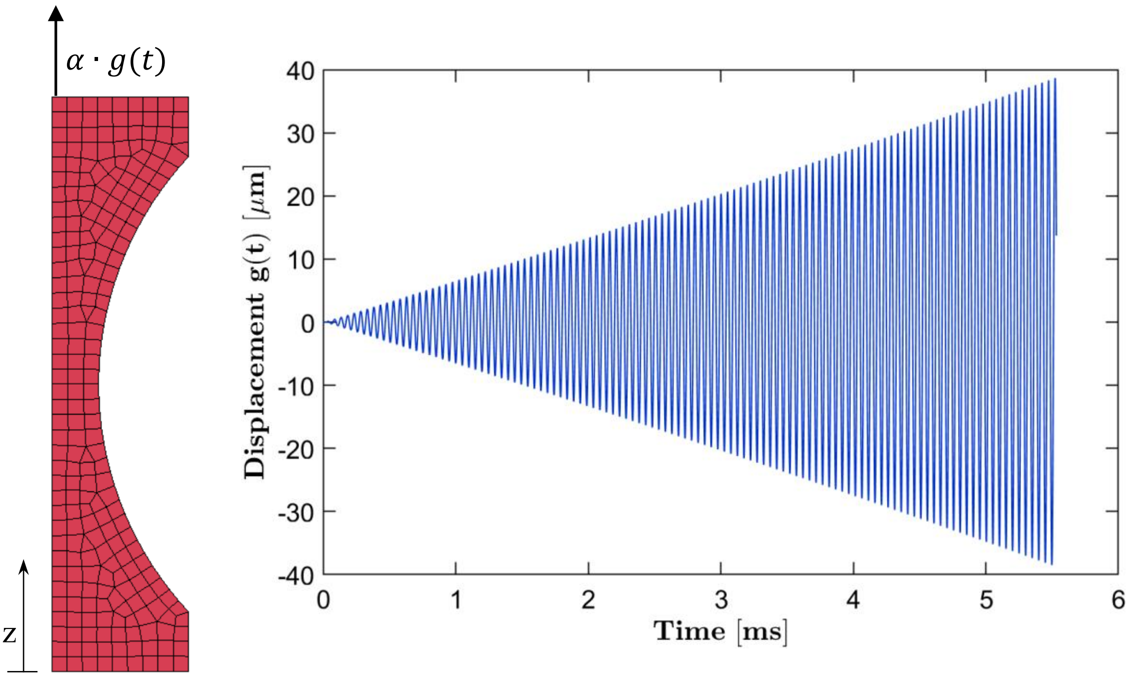

Figure 5.1 FEM of the hourglass graphite specimens with the boundary motion curve from one of the tests.

Since the horn-specimen interface geometry does not allow its displacement measurement with another laser, and there is not a second available high-speed camera that can reach a rate high enough to acquire multiple points per cycle, the boundary motion curve is approximated through the test measurements provided by strain gauges placed on the horn.

However, even though the strain gauges follow both the machine output frequency and the amplitude increment rate at the ramp, the actual strain amplitude measured in all the conducted tests, both in alumina and graphite, were found to be 12% to 23% larger than expected. This is attributed, in part, by the adhesive between the horn and the specimen absorbing around 8% of the displacement amplitude from the horn, instead of delivering 100% of it to the specimen, as observed in one of the tests that had the camera recording the horn-specimen interface.

Another contributing factor to this difference is that, to calculate the displacement arriving at the horn-specimen interface from the strain measurements by the strain gauges, it is assumed that the horn material has a perfectly linear-elastic behavior, which is a numerical approximation expected to have slight differences from the experimental behavior, especially when involving high strain rates like in the ultrasonic test. Moreover, no data in the literature that can be used to verify accuracy of strain gauges during the ramp was found, since ultrasonic testing machines are used in fatigue tests, with the only measurements available being related to the regime condition, and never considering the ramp at the beginning.

Since recording the zone around the adhesive in multiple tests would mean less accurate data on the specimens, multiple measurements for calibration purposes were collected with only the horn and no specimen attached to the machine. It was noticed that the displacements obtained from the camera and the laser, both measuring the horn free surface, were coherent with each other, always having at most a ±4% difference between one another, in the several measurements conducted for multiple output amplitudes. The measured displacements were also within the expected, according to the machine set output once regime was achieved, staying within a similar error margin, of ± 5%. However, the strain gauges always measured values 8% to 19% above the expected, assuming the displacements were accurate.

Despite having multiple contributing factors to this difference between the experimental strain and the theoretically estimated one, it was verified that, in all calibration measurements, the strain gauges curves have the expected frequency, and the form of their ramp is approximately linearly proportional to that of the displacements measured by the laser and the camera. Therefore, the boundary motion curve can be estimated through the fitting of the experimental strains measured on the horn, which is linearly converted into a displacement curve following the analytical equations for the horn-specimen system presented in Section 2.2.

Furthermore, it was observed that, for all the conducted experiments, the displacement $g(t)$, as illustrated in Fig. 5.1, has a form that can be fitted by the equation:

$$g(t) = (at^2 + bt + c) \cdot sin(2\pi \cdot f_{out} \cdot t) \tag{5.1}$$

being f_{out} the output frequency of the ultrasonic generator, t the time from the start of the test, and a, b and c empirical parameters resulting from the fitting of strain gauges data converted into a displacement curve as previously explained. The boundary motion curve, representing the effective displacement received by the specimen is proportional to Eq. 5.1, being $u_{z,int}(t) = \alpha \cdot g(t)$, with α being a non-dimensional quantity whose exact value will be optimized in LS-OPT, expected to be in the range $[0.75, 0.95]$, according to the described performed measurements.

The observations relative to the boundary motion curve are confirmed by Fig. 5.2, containing experimental data relative to the test that had the camera recording the horn-specimen interface. Fig. 5.2 compares the value measured by the tracker on the specimen at the spot closest to the horn, which should translate into the displacement curve applied to the specimen, as indicated in Fig. 5.1. This curve is then compared to $g(t)$, the empirically obtained curve from the strain gauges placed on the horn, and the curve corrected by the multiplication to α, showing that $g(t)$ is indeed a good approximation of the curve shape, while α can be optimized to properly adjust its amplitude. This should allow the reliable identification of boundary conditions, while the camera can be placed elsewhere on the specimen to prioritize the quantification of material behavior.

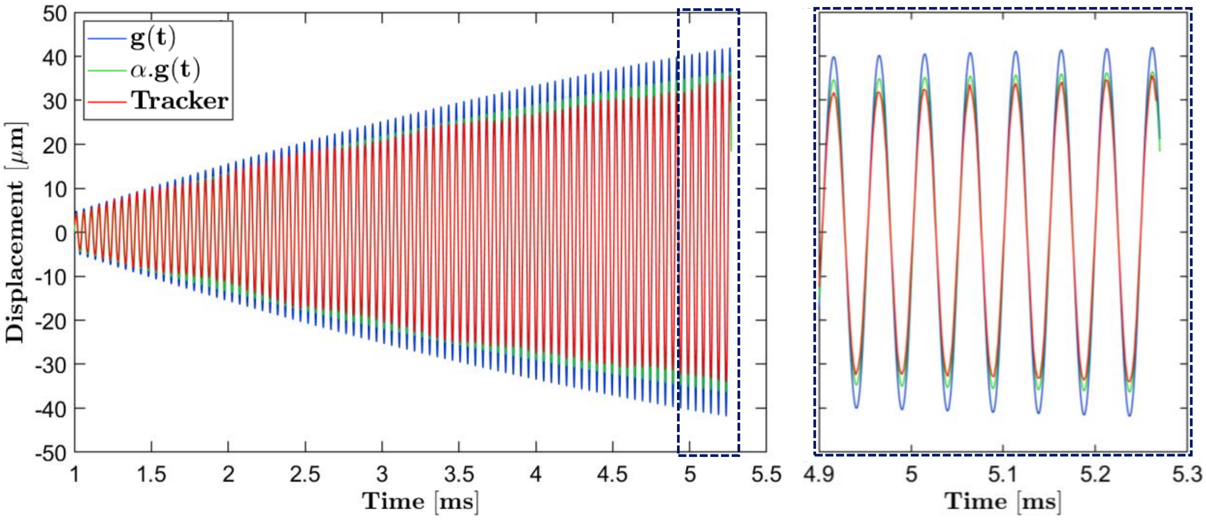

Figure 5.2 Comparison between the displacement curves $g(t)$, $\alpha \cdot g(t)$ once α has been optimized, and the one measured through tracking analysis.

Finally, the material model that should best simulate the specimens behavior should be selected. This task is accomplished through a qualitative observation of the specimen displacement curves and the choice of a material model possessing the necessary characteristics, potentially requiring some trial and error when it is observed that, even after material properties optimization, the desired result cannot be reached.

5.2. Parameter Optimization

With the FEM established, the optimization of the material parameters can be achieved through LS-OPT. The variables to be optimized are α, as detailed in Section 5.1, relative to the boundary motion curve, and one or more of the chosen material model properties. For instance, in a linear-elastic model, the only property to be optimized is the elastic modulus, since the density is directly measured on the specimens, and the Poisson ratio is approximated using the same methods as in the specimen design, which is satisfactory, since it cannot be estimated from uniaxial data. However, nonlinear material models usually possess multiple variables that need to be optimized, as in the case of graphite, further detailed in Chapter 7.

As optimization objective, it was established that the software should obtain the variables that best reproduce the displacements measured through the camera and the laser. Therefore, the goal was to minimize the error between the nodes numerical output displacement and the values experimentally measured. Particularly, only the experimental displacements from the last two cycles of each test are considered in the objectives, since at the beginning of the ramp, the noise in the measurements produces larger errors, whose influence in the results should be reduced. Moreover, the cycles preceding failure are the ones determining the material ultimate strength, being reasonable to focus on them to optimize material properties. It was also observed that calculating the numerical versus experimental errors between large datasets, i.e., more than one or two cycles, significantly increases computational time without necessarily improving the results.

Since the laser is pointed at the specimen center in all tests, its results can be directly inputted as objective of the corresponding node. However, the camera tracker points displacements need to be interpolated to calculate the experimental displacements at the corresponding nodes of the FEM. This can be seen in the schematics of Fig. 5.3, highlighting where some of the graphite specimen FEM nodes are positioned in the zone recorded by the camera and relative to the tracker ROIs.

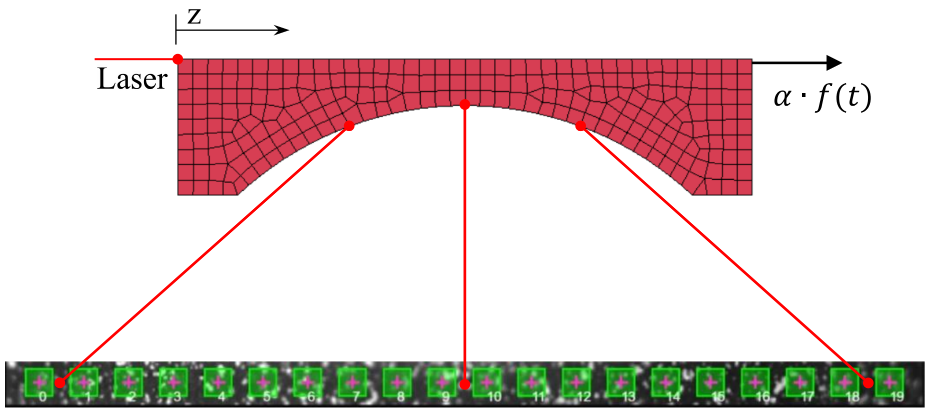

Figure 5.3 Illustration of procedure to define the experimental displacements as optimization objective.

The linear interpolation method adopted for the camera measurements was selected to avoid redoing the FEM for each specimen, since the camera resolution, as in the physical size corresponding to the recorded window, is slightly different for each test, being measured only after the camera focus is set for the respective specimen. The same method was applied to the alumina specimens, the only difference being that, as pointed out in Section 4.4, the camera records a zone far from the specimen center, and so will be the corresponding FEM nodes.

No other constraints are added to the optimization, since the boundary motion curve, calculated empirically from the experimental data, will dictate both the frequency and the ramp general form of the specimen resonance state. Hence, once the most accurate material model is selected, the variables indicating the material properties should converge to values that allow the reproduction of the measured resonance state on that frequency (f_{out}). Otherwise, in the case where the material properties values do not allow resonance condition to be attained for that frequency of the boundary motion curve, the simulated specimen simply behaves as a rigid body in motion, i.e., with all its nodes showing the exact same movement as the displacement applied on the boundary, with the same phase, frequency, and amplitude, while the strains in all elements are always zero.

Since each specimen is submitted to a different boundary motion curve, with its respective frequency and number of cycles, constituting essentially a different FEM for each test even if the material is the same, the variables cannot be optimized simultaneously for all the specimens. Therefore, optimization is conducted for each test independently. The material parameters obtained in each instance are then used to calculate the mean among the different tests to define the material properties. Finally, the optimizations are reconducted, this time fixing the material properties at the obtained mean values, and only having as variable the α

from the boundary motion curve. Hence, the only parameter unique to each specimen will be the one related to the respective test boundary condition since the material is the same in all instances.

The need to run multiple optimizations, which include at least one per specimen plus all the required trial runs to find the most adequate material model, emphasizes the importance of simplifying the numerical model. Therefore, to minimize computational time, it was verified that the mesh adopted to model the analyzed specimens were not refined beyond necessary. To exemplify this verification, Fig. 5.4 shows the results for the graphite specimens mesh as presented in Fig. 5.3, measuring around $0.8\,mm$, and a more refined mesh, measuring around $0.4\,mm$. The results in Fig. 5.4 were calculated using the nonlinear material model and parameters estimated in this work for graphite R4550, which will be discussed in Chapter 7. Both analyses consider the same boundary conditions, with the displacement applied to the specimen simulating the ramps observed in this work. The results are shown for the instant of time t_k when $u_{z,int}(t_k) = A_{out} = 48\,\mu m$, putting the specimen under a tensile load.

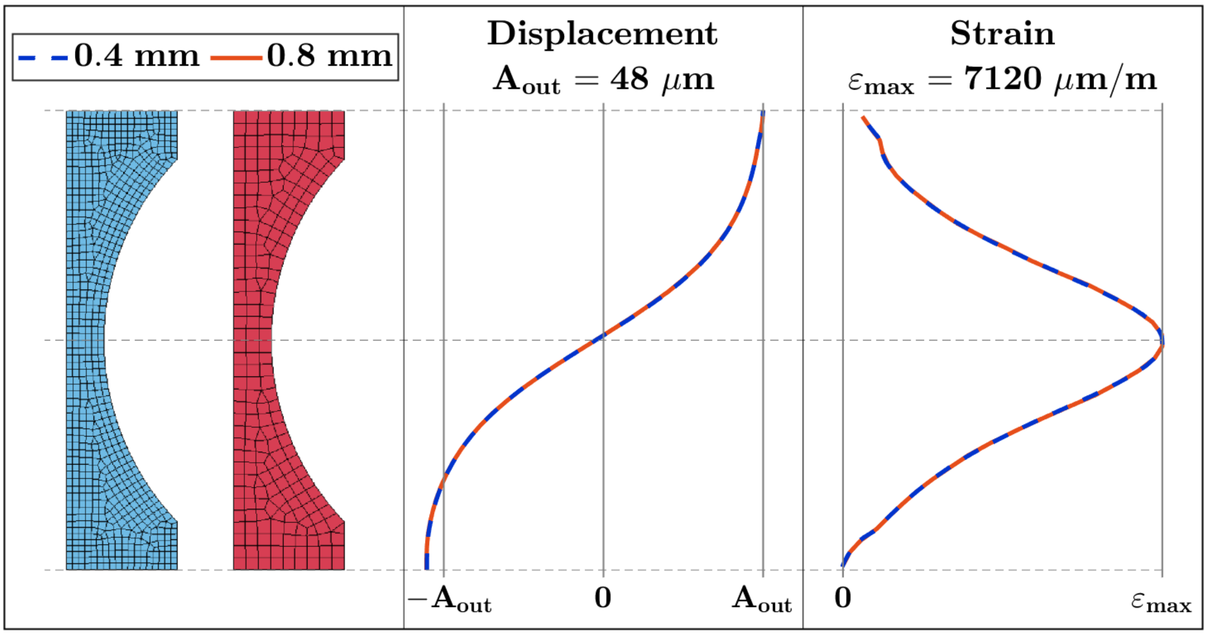

Figure 5.4 Comparison between longitudinal displacements and strains along the specimen axis calculated using two different meshes.

The nonlinear behavior of graphite R4550, in Fig. 5.4, can be noticed through the fact that the displacements at the interface with the horn and at the free extremity of the specimen have different magnitudes from each other, i.e., $U_f \neq A_{out}$, as opposed to the values presented through the analytic equations and curves from Section 2.2, which consider a linear-elastic model with $f_{out} = f_{n,s}$, resulting in $u_{z,f}(t) = -u_{z,int}(t)$. Additionally, it demonstrates that the strain on the interface with the horn is slightly above zero, which could be caused by a combination of the adopted nonlinear material model, and the applied boundary displacement being a ramp instead of regime condition. Despite these particularities caused by the nonlinear material model and $u_{z,int}(t)$ being a ramp, both meshes produce very similar results, with the maximum strain ε_{max} resulting in $7120\ \mu m/m$ for the more refined mesh, and $7119\ \mu m/m$ for the less refined mesh used in this work.

5.3. Results Extraction and Analysis

To verify the calculated material properties, the optimized FEM nodes displacements are compared to those experimentally measured through the calculation of a coefficient of determination, according to Eq. 5.2:

$$R^2 = 1 - \frac{\Sigma\left(u_{exp} - u_{num}\right)^2}{\Sigma\left(u_{exp} - \overline{u_{exp}}\right)^2}, \tag{5.2}$$

being u_{exp} and u_{num} the experimental and the numerical displacement, respectively, at the corresponding FEM node. Furthermore, rather than comparing the experimental and numerical results of only the two cycles preceding failure, which correspond to those considered as optimization objectives, the last 20 cycles for each test are applied to Eq. 5.2. By considering more cycles in the coefficient of determination, a more general evaluation of the numerical model and optimization procedure can be obtained, also providing indication of the process robustness in reproducing a large portion of the test despite the restricted choice of optimization objectives.

With the FEM optimized and validated, the normal stress generated in each element is extracted, particularly the values for the highest global tensile stress achieved on that specimen σ_{max}, and its tensile strength at fracture σ_f, which is the local nominal stress value extracted from the element in correspondence to the critical defect identified according to the procedure established in Section 3.3. By this definition, it is expected that $\sigma_{max} \geq \sigma_f$, since the element that achieves the highest tensile stress will not be necessarily the one to originate failure, which could happen in an element achieving a lower tensile stress but containing a larger defect.

The critical defect position within the specimen is also calculated through the analysis conducted in VGSTUDIO, being defined as the coordinates of its geometrical center. For the few cases, all identified in alumina specimens, in which the critical defect was large enough to occupy more than one element, it was verified that its center position on the z-axis was positioned in an element located on the fracture surface, being adjusted accordingly when necessary.

With the successful completion of the numerical model, the material properties are defined, as well as the accurately estimated amplitudes of the boundary motion curve. Furthermore, the value for the material fracture strength σ_f is finally obtained, completing the required information for the calculation of the stress intensity factors $K_{I,d}$, defined in Section 3.3. Additionally, the tensile stress σ achieved on each defect position can also be identified, through the extraction of the local nominal stress generated in each element, then applied to the same formulation for further analysis.

Numerical Modeling

Chapter 6

6. Alumina 99.5%

In this chapter, the parameters for micro-CT and UST test on alumina will be specified, along with the particularities of the analysis methods for the experimental data and the numerical model, followed by the results presentation. The entirety of the procedure defined for characterization of brittle materials was applied to 10 specimens of alumina 99.5%.

6.1. Preliminary Material Characterization

To verify the specimens conformity with the initial design parameters, a few measurements were conducted, more specifically to verify their density, longitudinal natural frequency, and elastic modulus. While the density was calculated from measurements using a precision scale and a caliper, the frequency and elastic modulus were obtained through IET. The results were obtained as follows:

Table 6.1 Preliminary characterization of alumina specimens.

Property	Mean	Standard deviation
Density $[kg/m^3]$	3969	1.3

Frequency $[Hz]$	20362	25
Elastic modulus $[GPa]$	395.1	0.9

Table 6.1 shows that the specimens have slightly higher values for all three properties when compared to the values adopted in the design. Nevertheless, the frequency of the specimen is within the ultrasonic machine operating range, which should allow the tests to be properly conducted.

6.2. Defect Characterization Parameters

Alumina is a relatively simple material to be scanned, since it is expected to be homogeneous while its component chemical elements should be able to attenuate the x-rays at a level that should create good contrast in the results. Particularly, the specimens geometry is not expected to generate excessive beam hardening, which can be eliminated with an adequate filter during the scan, in this case a copper filter, as shown in Table 6.2 with the other adopted test parameters.

Table 6.2 CT-scanner configuration adopted for the alumina specimens.

Parameter	Set value
Tube current $[\mu A]$	80
Tube voltage $[kV]$	240
Exposure time $[s]$	1.0
SOD $[mm]$	55
SDD $[mm]$	1100
Filter	1.5 mm Cu
Number of projections	1600

The configuration in Table 6.2 produces a resolution of $10\ \mu m$, which is enough to capture the full diameter of the specimen, and a portion of its length of around $18\ mm$ in high quality, from the captured span of $20.48\ mm$, since the upper and lower borders of the reconstruction from cone beam CT-scanners always need to be eliminated due to errors caused by a phenomenon called capping artifact. Additionally, according to Section 3.3, the obtained resolution should be enough to reliably identify the presence of defects that respect $\sqrt{A} \geq 40\ \mu m$, which is a size considerably larger than the grain sizes identified in the literature for alumina samples of at least 98% purity, ranging from $0.3\ \mu m$ to $10\ \mu m$ [1-3].

However, as observed in Subsection 4.3.1, these specimens have a large zone at their center that could be considered as being at risk of fracture during the UST test. Therefore, to ensure that the zone where the fracture would happen is scanned before the specimen failure, the micro-CT captured a span of at least $135\ mm$ at each specimen center, as illustrated in Fig. 6.1, showing the final 3D reconstruction and its location on the specimen. To achieve this, each specimen was placed vertically on the stage and scanned 10 times, changing the stage z-position at constant steps accordingly. When all the reconstructions are positioned in VGSTUDIO, they generate the 3D representation in Fig. 6.1, necessary for the accurate identification of the defects locations.

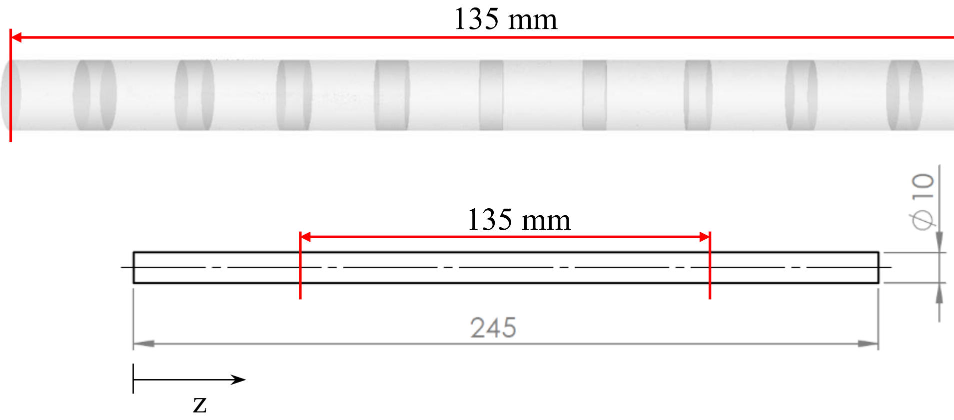

Figure 6.1 Schematics of the scanned length of alumina specimens.

The parameters for defect analysis were selected as described in Section 3.2, with the algorithm focus on void analysis, to find pores and internal cracks, deemed more prominent in a homogenous material. However, an inclusion analysis was also conducted to verify the need to consider additional types of imperfections.

Moreover, the weights of the custom probability criterion were selected to prioritize the defect candidate contrast with the surrounding region, with its size, and relative gray value also being considered in smaller scale. Within the software, this translates into altering the factors called, respectively, scaled deviation, ignore small defects, voxel count, and deviation. The analysis results were then qualitatively observed, to ascertain that defect candidates were not being incorrectly included or excluded in the results, in which case the chosen weights would be slightly changed until most defects, specifically the largest ones, were accurately accounted for, following the values according to Table 6.3. Meanwhile, all the absent parameters were fixed at zero.

Table 6.3 Probability factors used for defect analysis on alumina.

Factor	Scaled deviation	Ignore small defects	Voxel count	Deviation	Constant
Value	1.00	[0.30, 0.50]	[0.10, 0.30]	[0.10, 0.30]	4.00

6.3. Defect Characterization Results

The internal defect analysis on alumina produced a wide variety of results, that were classified into three groups: pores, cracks, and inclusion. Generally, alumina specimens are characterized for the presence of seemingly uniformly distributed pores, which account for almost the totality of identified defects. They tend to be small – being all under $350\ \mu m$ in size ($\sqrt{A}$) – while their shapes indicate that they might be generated by the presence of trapped gas or poor fusion among the particles. 5 out of the 10 analyzed specimens only presented pores in all their respective scanned lengths.

The described results are illustrated through specimen number 6 on Fig. 6.2, with 6.2a showing the analysis on the complete scanned length and the absence of large defects, while 6.2b shows the defects surrounding the fracture surface after overlapping the ultrasonically tested specimen pieces with the original, among the defects contained between the fracture surfaces and those split by them, the largest one is selected as the critical. Moreover, Figs. 6.2c, and 6.2d compare the three observed types of pores, representing, respectively, a defect with high sphericity, a defect elongated on the specimen axial direction (same as the rods extrusion before sintering), and a defect with irregular shape. While the two formers are probably caused by gas, the latter might indicate poor bonding between particles, since some material seems to be present but in a smaller density than the surroundings, generating a zone with lower gray values than the material while still being higher than those caused by complete voids, like in Figs. 6.2c and 6.2d.

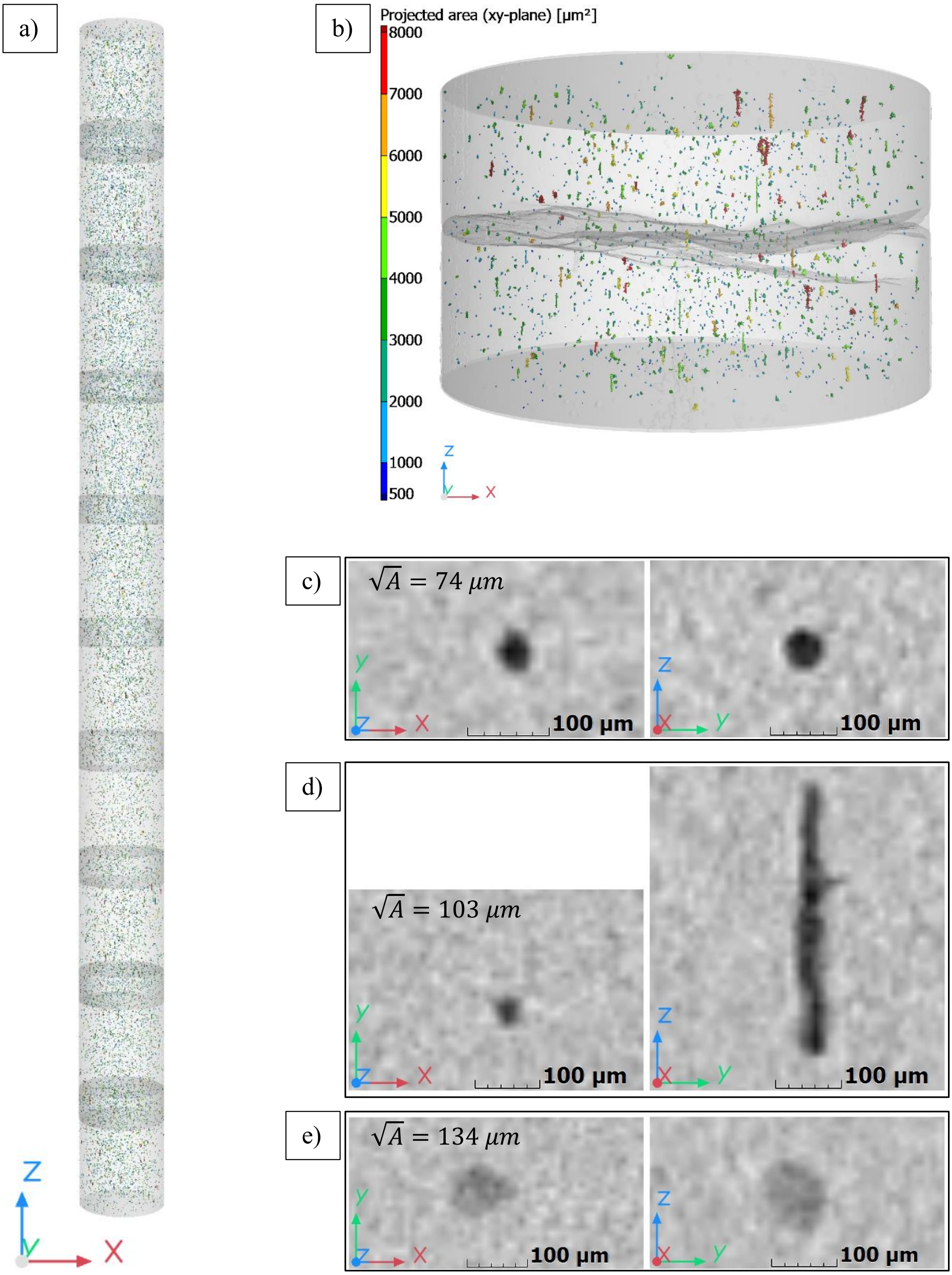

Figure 6.2 Micro-CT data for alumina specimen 6, with (a) all the identified defects, (b) the defects surrounding the fracture surface, (c) a highly spheric pore, (d) an elongated pore, and (e) a defect likely caused by poor bonding.

In addition, multiple severe defects were detected in other specimens, albeit in much smaller number, in the form of cracks. These shapes are characterized by large sizes, often above

$1\ mm$, and by their propagation through well-bonded material, which might indicate their appearance after sintering. 4 out of the 10 analyzed specimens presented one or more crack-type imperfections, besides pores, in their respective scanned lengths. One of these instances is presented in Fig. 6.3, with specimen number 5, whose analysis allowed the identification of two cracks, with sizes $3443\ \mu m$ and $1186\ \mu m$, respectively, with the fracture surface developing from the largest one, as seen in Fig. 6.3b showing the overlap between the specimen remaining pieces scans and the original. Meanwhile, Fig. 6.3c shows the comparison of the same slice taken before and after the ultrasonic test, confirming the crack being split by the fracture surface.

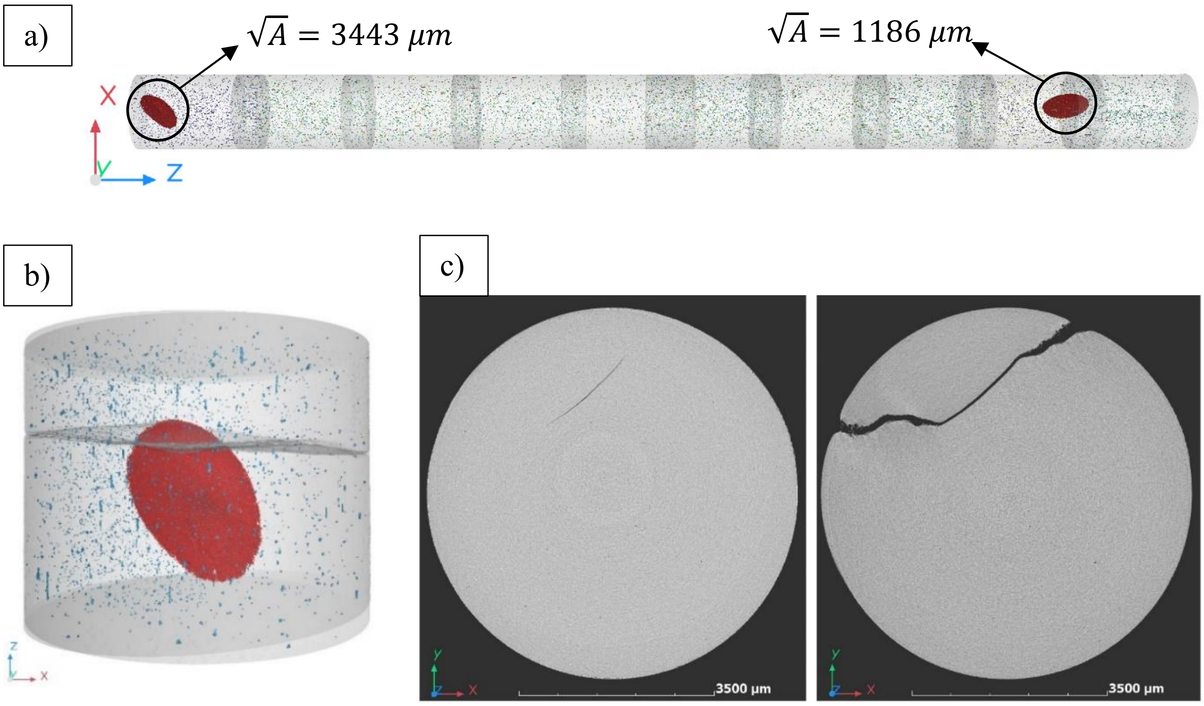

Figure 6.3 Micro-CT data for alumina specimen 5, with (a) the two identified cracks with their respective sizes, (b) the fracture surface passing through the largest crack, and (c) the before and after of a fracture surface cross-section slice.

Finally, despite the inclusion analysis having been conducted in all original scans, only one inclusion was found. Aside from this particularity, the relative specimen, of number 1, showed no cracks, only pores as its remaining imperfections. Taking advantage of the fact that this inclusion also happened to be specimen 1 critical defect, being seen on its fracture surface, it was observed in FESEM, and an Energy-Dispersive X-Ray Spectroscopy (EDS) analysis was conducted to identify the components present in the inclusion. Fig. 6.4 shows the defect analysis conducted on specimen 1, with 6.4a showing the defects in the vicinity of the fracture surface, all of which are pores, highlighting the only inclusion. Meanwhile, Fig. 6.4b contains the slice from the original scan, where the fracture surface would split the inclusion, in correspondence with the FESEM image in Fig. 6.4c, taken after the ultrasonic test, along with the results from the EDS analysis of the inclusion, showing that it was caused by an impurity of ferrous oxide (FeO) mixed with alumina, while the 4% of other elements are mostly carbon and oxygen.

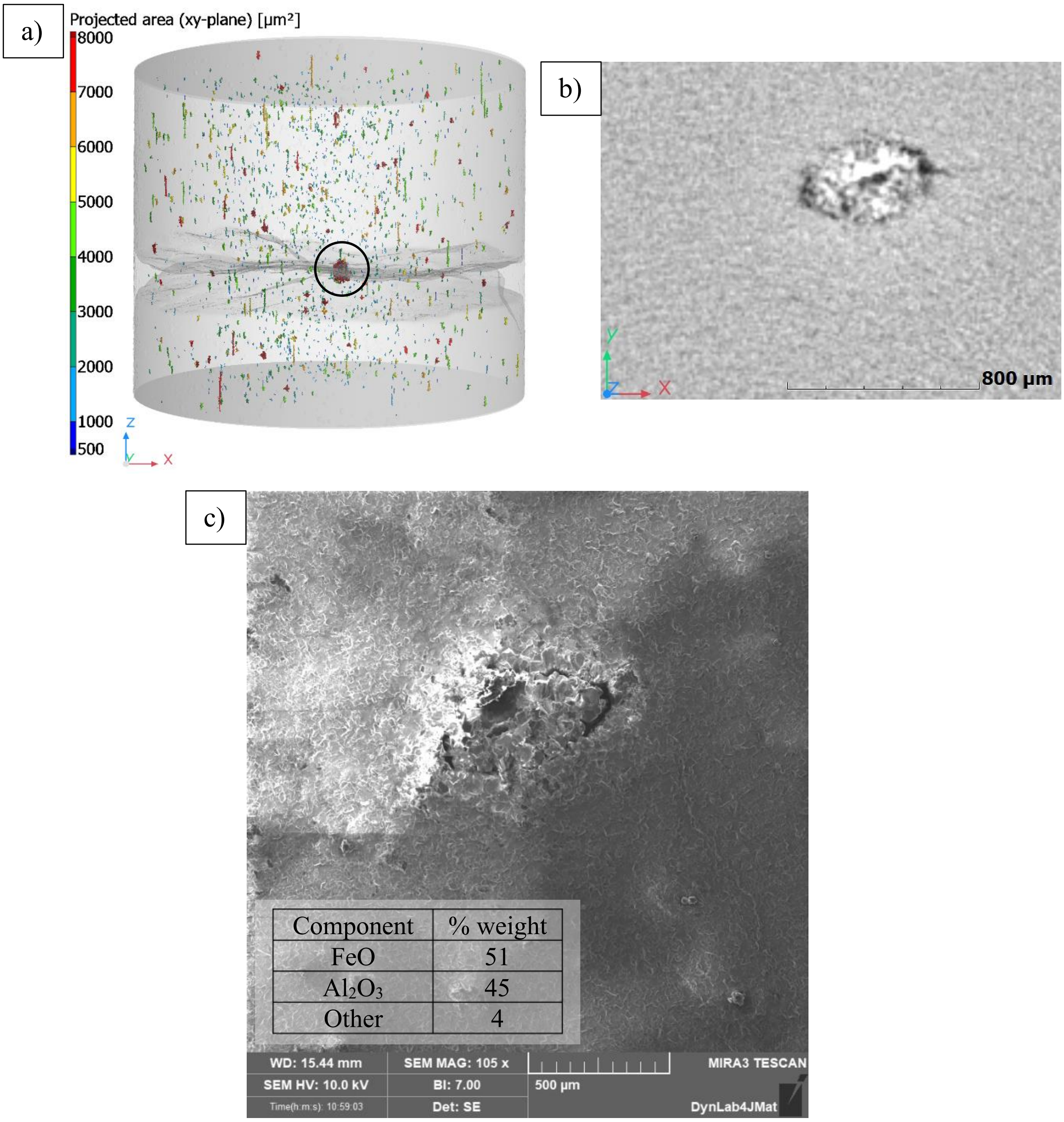

Component	% weight
FeO	51
Al_2O_3	45
Other	4

Figure 6.4 Experimental analysis of alumina specimen 1, the micro-CT showing (a) the defects surrounding the fracture surface and (b) the slice from the original scan containing the inclusion, and (c) the FESEM image with the EDS analysis results of the inclusion.

Following the established methods for the identification of the critical defect and its classification, Table 6.4 was compiled, comparing, for each specimen, the largest defect with the critical defect, it also indicates that the inclusion size is comparable with the largest pores, while the cracks are around 10 times larger.

Table 6.4 Defect analysis results for each alumina specimen, comparing their respective critical and largest defects.

Specimen	Critical defect size [μm]	Critical defect type	Largest defect size [μm]	Largest defect type
1	397	Inclusion	The critical is also the largest.	
2	96	Pore	149	Pore
3	107	Pore	289	Pore
4	92	Pore	305	Pore
5	3443	Crack	The critical is also the largest.	
6	93	Pore	193	Pore
7	3102	Crack	The critical is also the largest.	
8	2714	Crack	The critical is also the largest.	
9	1089	Crack	1152	Crack
10	104	Pore	175	Pore

Table 6.4 also indicates that the specimens containing exclusively pores always present larger defects than the one identified as critical, which is expected. Since the normal stress reaches different amplitudes along the specimen and, when no particularly severe imperfections are present, the critical defect will likely be in the higher stress zones, closer to the specimen center. Meanwhile, when a very large imperfection is present, the specimen could very well fail on a lower stress zone, such is the case for number 5, in Fig. 6.3.

Given the variety of imperfections found on alumina specimens, concerning size, shape, and origin, a large scatter of fracture strength is expected as well. To visually compare the critical defects, their surface mesh was extracted from VGSTUDIO, being presented in Fig. 6.5, with 6.5a showing the inclusion, from specimen 1 (in red), in scale with the pores (in green), while 6.5b shows the inclusion in scale with the cracks (in blue). The defects view on the xy-plane corresponds to their respective projected areas, used to define $\sqrt{A}$.

Alumina 99.5%

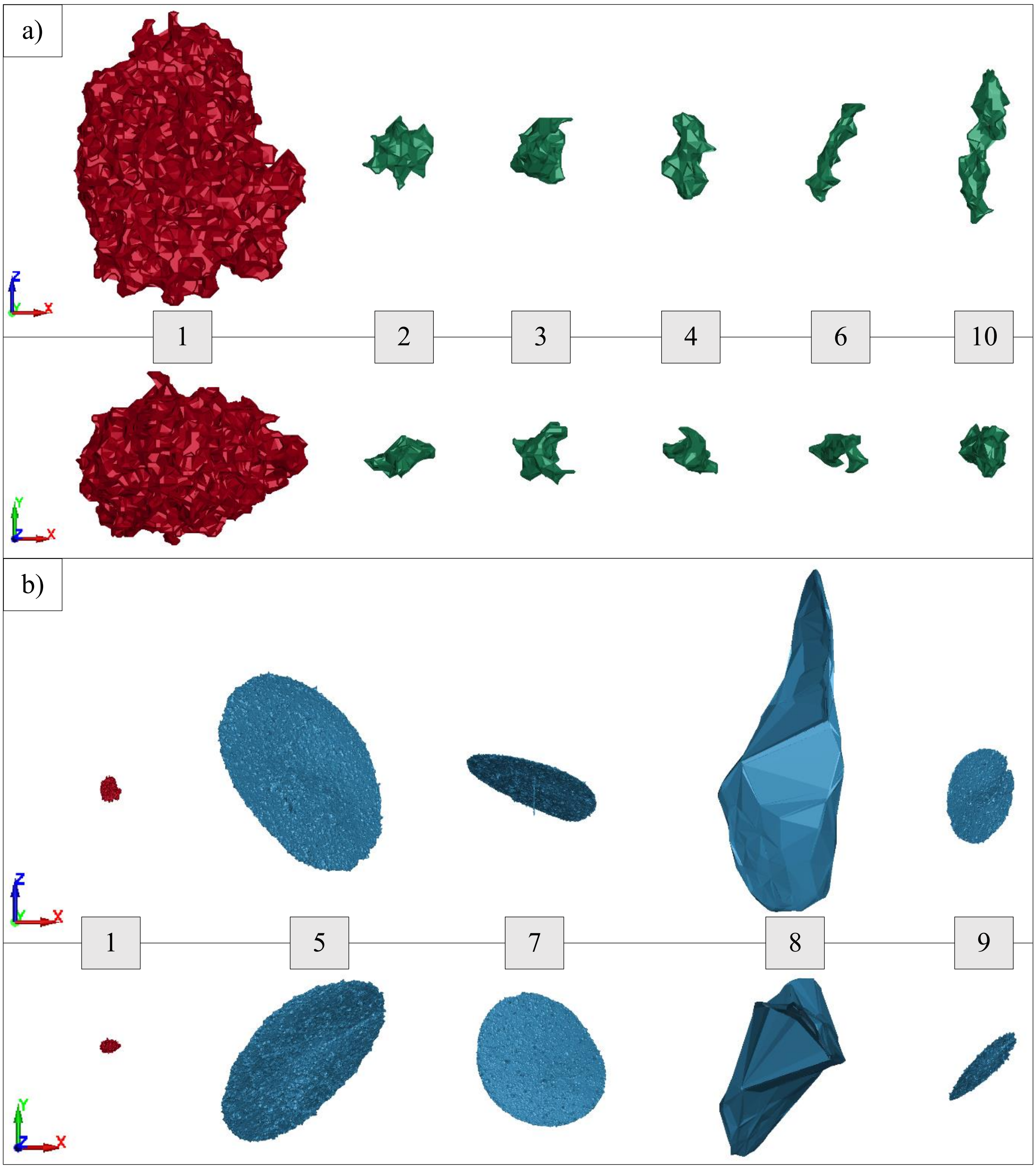

Figure 6.5 Alumina critical defects surface meshes, with frontal (xz-plane) and top (xy-plane) views, being (a) the inclusion (red) in scale with the pores (green), and (b) the inclusion (red) in scale with the cracks (blue).

It can be noticed, from Fig 6.5, that the pores tend to assume one of the previously described shapes, even though their surfaces are often irregular. Meanwhile, the cracks are mostly penny-shaped, although not completely flat and assuming elliptical forms, and often connected with neighboring pores, increasing their irregularity. The only exception being specimen 8, which showed ramified cracks on the fracture surface and its surroundings, as in Fig. 6.6, showing the 3D overlap and a vertical slice of these cracks. The critical defect, this time in red, is apparently formed by multiple interconnected cracks, while the remaining highlighted imperfections are smaller cracks disconnected from the critical one, the pores being all suppressed from the graphical representation for a better visualization of the cracks.

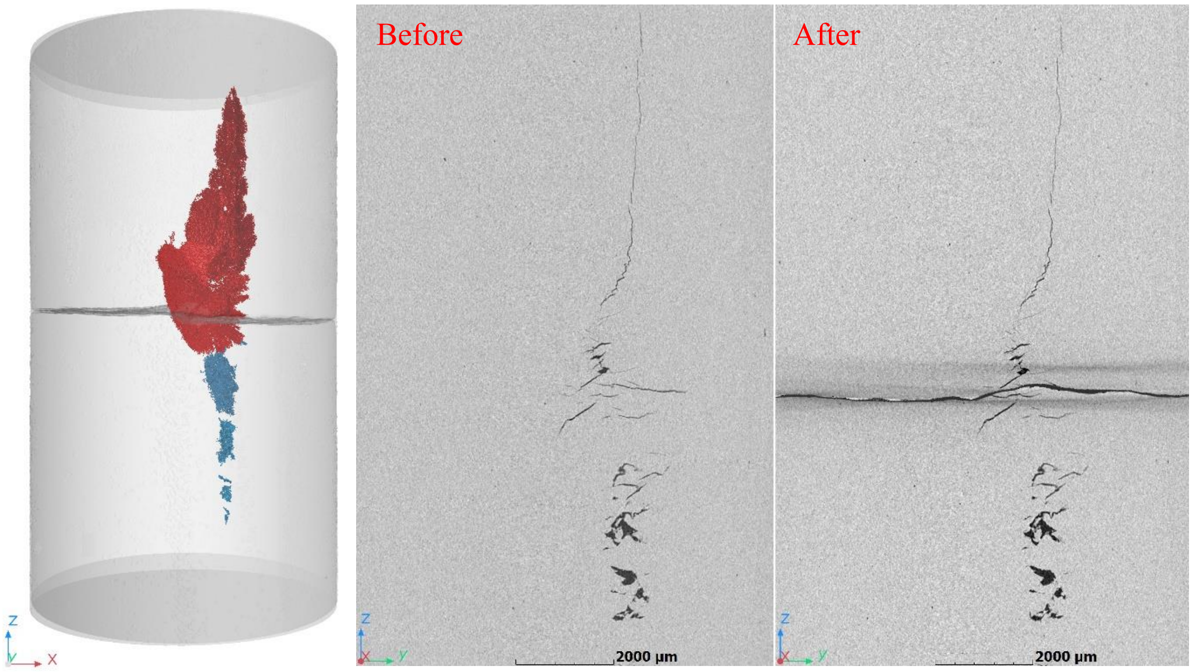

Figure 6.6 Illustration of alumina specimen 8 cracks.

Finally, a verification using defect analysis results was conducted to collect evidence that the small number of cycles necessary to conduct the UST test were not likely to have caused defect propagation like in fatigue tests. Since the micro-CT parameters used to scan the original specimens and their broken pieces were the same, the defect analysis results should also be approximately the same for the defects in the vicinity of the piece fracture surfaces, i.e., excluding those that were split or went missing with eventual small fragments.

Therefore, a defect analysis with the same parameters as the originals was conducted on the broken pieces scans, comparing the corresponding detected imperfections before and after the ultrasonic test. The defects larger than 40 μm identified in both analyses were compared, as shown for specimen 8 in Fig. 6.7a through the plot of their sizes by their position from the specimen free extremity in the ultrasonic test, which then had their normal Probability Distribution Functions (PDF) calculated as in Fig. 6.7b. Particularly, specimen 8, also having a large number of cracks, as seen in Fig 6.6, that were not part of the fracture surface and were captured on the rescan, should provide more concrete evidence that the defects are not propagating due to fatigue. Indeed, the largest defects in the specimen have approximately the same sizes in both analyses, while the difference in mean size for before (μ_b) and after (μ_a) the ultrasonic test is below the scanning resolution of 10 μm.

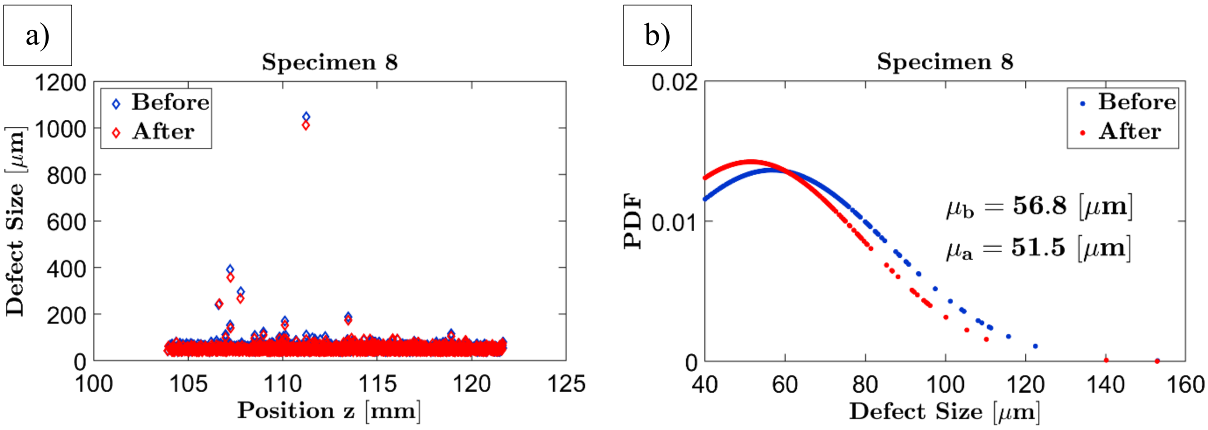

Figure 6.7 Defect analyses before and after the ultrasonic test for alumina specimen 8, with (a) showing the defect sizes and their positions, and (b) their size normal PDF.

Although the scanning and analysis parameters were the same in all instances, several other factors can influence the results, such as the newly created fracture surfaces whose irregular shapes cause localized beam hardening or noise in the scans, and errors in the broken pieces orientation over the original during object registration. Moreover, there could be effects of remaining substances, that are not present in the original scans, applied to the specimens lateral surfaces for the tensile test, comprised by spray paint for DIC analysis, adhesives for eventual strain gauges and for attaching the specimen to the horn, all of which cannot be properly removed without causing additional damage to the fracture surfaces.

Nevertheless, the difference in the resulting mean defect size in all instances was seen to be below the scanning resolution, according to Fig. 6.8, reporting the remaining specimens. Therefore, there is no evidence suggesting that defects might have propagated due to the cycles required to achieve the specimens fracture strength, indicating a possible absence of fatigue damage.

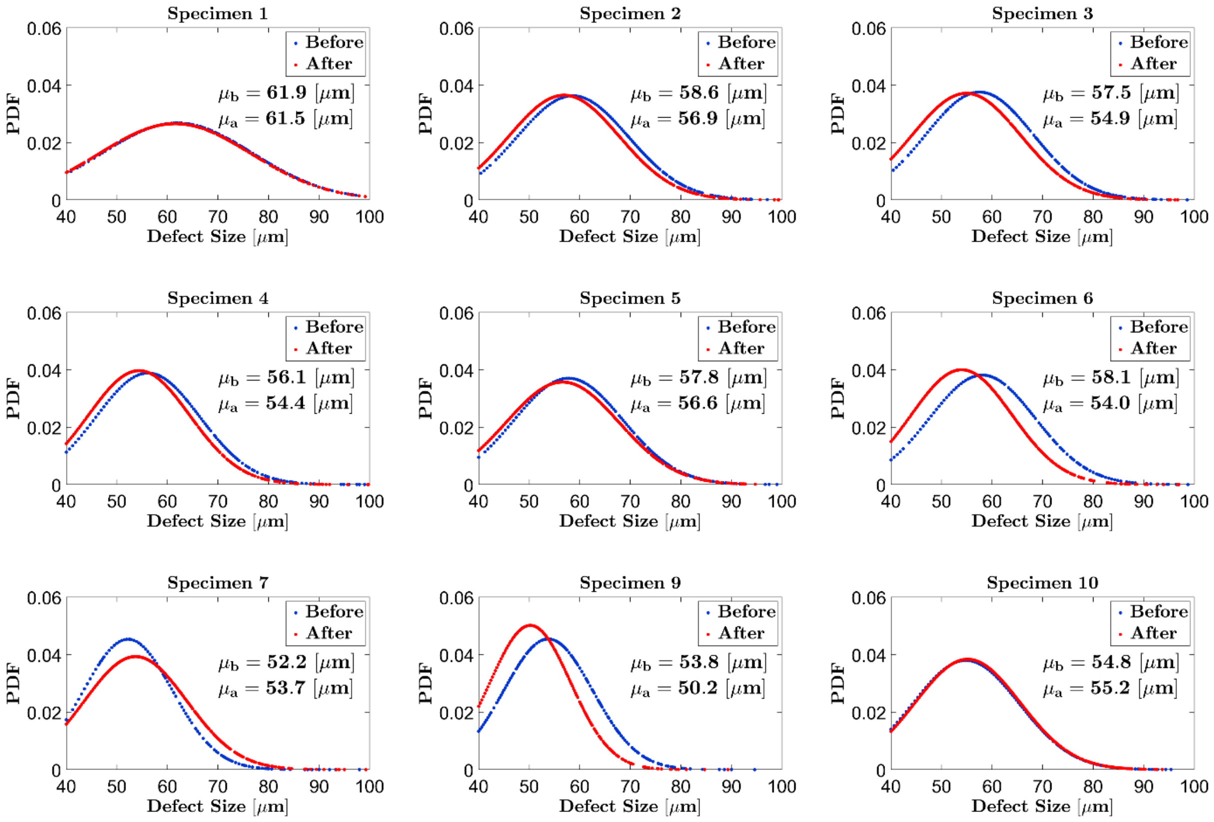

Figure 6.8 Comparison of normal PDF of defect sizes before and after the ultrasonic test for the remaining specimens.

6.4. Ultrasonic Tensile Test Parameters

The specific parameters for the UST tests on alumina are reported on Table 6.5. The selected output amplitude applied to the material properties measured in Section 6.1 considering a linear-elastic material, should achieve the indicated maximum stress amplitude at the end of the ramp. The output frequencies were defined by the horn signature procedure, in which the ultrasonic testing machine measures the horn-specimen system resonance frequency. Meanwhile, the camera resolution indicates the pixel size of the acquired images.

Table 6.5 UST test parameters for alumina.

Specimen	Output frequency f_{out} $[Hz]$	Output amplitude $[V]$	Maximum stress $[MPa]$	Camera resolution $[\mu m]$
1	20269	9	547	30.7
2	20284			30.6

3	20271			29.5
4	20324			28.9
5	20270			28.5
6	20332			28.9
7	20269			28.0
8	20329			28.9
9	20362			28.9
10	20387			28.9
Mean	20310	-	-	29.2

Furthermore, since the camera was positioned near the specimen free extremity, to allow the measurement of larger displacement amplitudes, the fracture zone was unlikely to be recorded. Since, when failure happens, the system natural frequency suddenly changes, it is expected that the machine will be momentarily destabilized until it is stopped, producing peaks of stress, which often causes the broken piece still attached to the horn fall off due to the adhesive failure. When concerning a material as brittle as alumina, these sudden peaks of stress could cause not only failure on the adhesive, but also on other points of the specimen piece still attached to the machine.

Therefore, another camera, with $30\ kfps$ acquisition rate, was used to record the full specimen, so that the first generated fracture surface could be defined in case secondary fractures should occur between failure and the system complete halt, which generally takes around three or four cycles. The recording window by the second camera can be seen in Fig. 6.9a, which also indicates the zone being captured by the main camera, detailed in Section 4.4, whose frame is shown in Fig. 6.9b. Meanwhile, Fig. 6.9c indicates the first fracture surface to appear on the specimen, also marked in Fig. 6.9a. This particular specimen produced three secondary fracture surfaces after failure occurred, hence the need to set up a second camera.

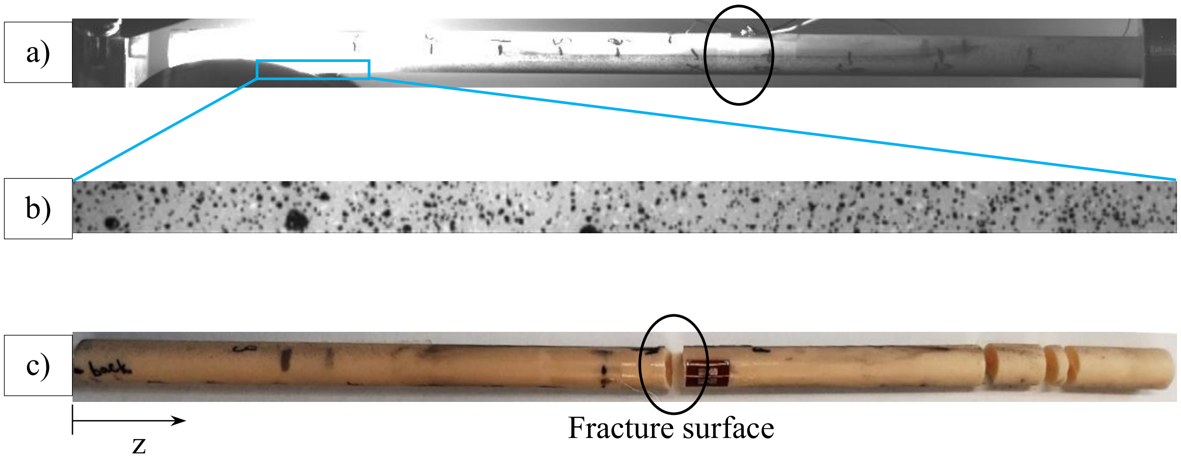

Figure 6.9 Alumina data recording schematics, showing (a) second camera frame, indicating (b) the zone recorded by the main camera for DIC, and (c) the fracture surface.

6.5. Ultrasonic Tensile Test Results

Following the raw data analyses procedures described in Section 4.7, the displacement graphics for each specimen were obtained and plotted, as in Fig. 6.10 for specimen 6. Fig. 6.10 shows the results measured through the laser, whose position is indicated on the specimen schematics, and the camera, already interpolated for the 6 points in correspondence to the FEM nodes, as indicated in the recorded frame.

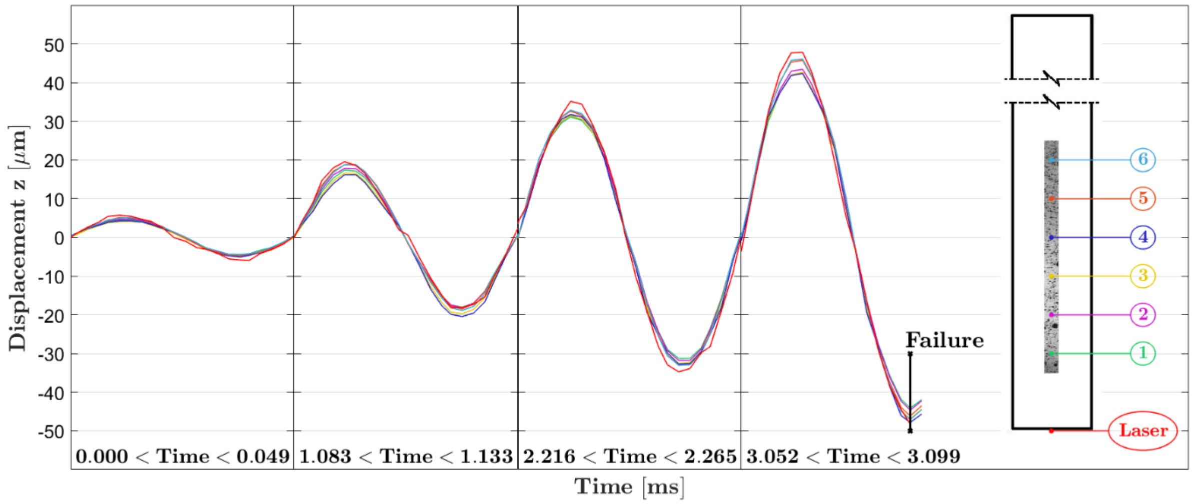

Figure 6.10 Displacement results for specimen 6 showing the amplitudes at different time ranges up to failure.

Fig. 6.10 shows the laser being in phase with all the camera tracker points, accordingly to the expected, meaning that, for each cycle, all the curves have their peaks and valleys, respectively, around the same instant. Fig. 6.10 also demonstrates that failure occurs around a peak of tensile stress, i.e., where the measured displacements are near a cycle valley, when, theoretically, the lower half of the specimen should have negative displacements and the upper half positive ones, as demonstrated by Fig. 4.11b, in Section 4.4. Moreover, it can be noticed that, even while ramping up to regime state, the displacements seem symmetrical with respect to the zero abscissa, with each curve in Fig. 6.10 having similar magnitudes for the maximum and minimum value within the same cycle. Such verifications were conducted for all tested specimens and, once the analysis was validated, the results could be compiled in Table 6.6.

Table 6.6 UST test experimental results for alumina.

Specimen	Maximum laser amplitude $[\mu m]$	Number of cycles	Test duration $[ms]$	Fracture surface position z $[mm]$
1	47.0	75	3.7	76.2
2	66.6	100	4.9	109.9
3	52.2	68	3.4	143.0
4	52.8	71	3.5	145.8
5	24.9	69	3.4	57.3
6	48.1	64	3.1	108.5
7	17.5	33	1.6	101.6
8	18.0	44	2.2	116.8
9	39.1	57	2.8	140.9
10	44.6	68	3.3	114.0

Table 6.6 reports the maximum measured amplitude by the laser, with the camera measurements being very similar in each case, as in Fig. 6.10, since it records a zone close to the specimen free extremity. Moreover, the comparison between the amplitudes indicates that the testing machine is not able to reproduce the ramp increase rate throughout the different tests, particularly, specimens 3 and 5 sustained a similar number of cycles, with the latter achieving less than half the amplitude at the laser. Nevertheless, the machine seems to be capable of respecting the imposed ramp time, since all tests lasted less than 5 ms, while the theoretical regime amplitude measured by the laser should be $108\,\mu m$. Furthermore, the

boundary motion curve defined in Section 5.1 was observed to properly respect these particularities, especially since its general shape comes from strain gauges measurements on the horn.

Finally, Table 6.6 also reports the position in z-direction of the fracture surface, with $z = 0$ corresponding to its free extremity. The fracture surface position is the same as the one measured for the critical defect, as defined in Section 3.3. In general, it can be said that the specimens that only showed pores as imperfections fail closer to the specimen center (at $z = 124.5\,mm$), i.e., at the higher stress zones, while those containing more severe flaws, are largely dependent on their locations.

6.6. FEM Setup

Observing the displacement curves behavior, following the one from Fig. 6.10, it was established that the material model best able to simulate alumina 99.5% was linear-elastic. Indeed, the results in Fig. 6.10 are within the expected when considering the analytical resonance state for the alumina specimens, demonstrated in Fig. 4.11b, in Section 4.4, which employs a linear-elastic material model. Although the experiment likely does not obey the analytical equations assumption of $f_{out} = f_{n,h} = f_{n,s}$, causing slight changes on the amplitudes observed in Fig. 4.11b, the experimental curves in Fig. 6.10 are still in phase with each other, i.e., all their peaks and valleys happen around the same instant of time in each cycle, and they are also symmetrical with the zero abscissa despite the increasing amplitude of the boundary motion curve. Both behaviors suggest a linear response that is not dependent on the strain rate.

Therefore, the only material property that needs to be optimized in the adopted linear-elastic model is the elastic modulus E, along with factor α from the boundary motion curve. Meanwhile, the Poisson ratio was used as the design value of 0.26, since it cannot be estimated from longitudinal displacement data. The optimization objectives were grouped so that each measuring device would contribute equally to the variables calculation. Therefore, the laser measurements were attributed weight 6, while each of the nodes measured by the camera, as shown in Fig. 6.10 were attributed weight 1.

6.7. FEM Results

To guarantee the successful optimization of the FEM, the displacements numerically obtained are compared to those experimentally measured, as in Fig. 6.11, representing specimen 6, also having their determination coefficients calculated, according to Section 5.3, as a method for quantitatively validating the results. It can be noticed in Fig. 6.11, through the observation of the last cycle before failure, that the linear-elastic material model applied to alumina is capable of reliably reproducing its behavior during the ultrasonic test.

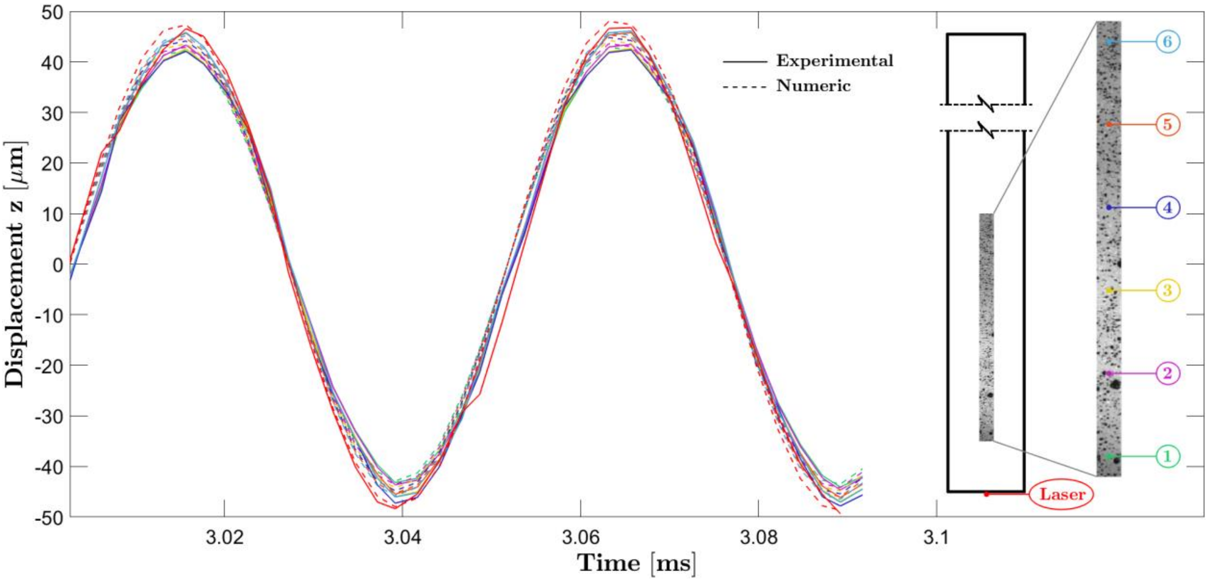

Figure 6.11 Comparison between the experimental displacement curves and those obtained through the numerical model for alumina.

Furthermore, the optimization conducted in all specimens resulted in an elastic modulus of $371.2\ GPa$, which is 6.0 % smaller than the one measured through IET, shown in Section 6.1. However, this difference is expected, since experimental data from the literature suggests that brittle materials elastic modulus measured in dynamic non-destructive tests, such as IET, tend to be slightly higher than those measured in quasi-static tests, such as uniaxial compression, and three and four-point bending [4-6]. Although the UST test involves high strain rates, contrary to quasi-static tests, it also generates strains on the specimen that are considerably larger than those caused by the impulse from an IET method, potentially causing a similar effect to those of a quasi-static test. The final empirically obtained material properties are reported in Table 6.7.

Table 6.7 Alumina material properties.

Density $[kg/m^3]$	3969

Elastic modulus $[GPa]$	371.2

With the obtained material model, the results for each specimen could be extracted according to Table 6.8, showing primarily the determination coefficients indicating the model high accuracy for all specimens. Moreover, Table 6.8 reports their respective factor α values, all within the range $[0.80, 0.89]$, with the resulting maximum amplitude achieved by the boundary motion curve, corresponding to the amplitude effectively delivered to the specimen, including the optimized α. Another indication of the proper choice of material model and estimation of the optimization variables is the fact that the calculated achieved amplitude, i.e., the amplitude of the boundary motion curve in the last cycle, is similar to the maximum amplitude measured by the laser for each respective specimen, previously presented in Table 6.6, in Section 6.5. Considering these two quantities as estimates of A_{out} and U_f, respectively, it is observed that $A_{out} \approx U_f$, with U_f differing at most in 5.5% from A_{out}. Meanwhile, the analytical amplitudes shown Fig. 4.11b, in Section 4.4, have $A_{out} = U_f$ for a linear-elastic material, indicating that the differences in the experimental values for of A_{out} and U_f are likely caused by a combination of experimental errors, and by the analytical equations assuming $f_{out} = f_{n,h} = f_{n,s}$ and regime condition.

Table 6.8 Results for each alumina specimen extracted from the optimized FEM.

Specimen	Average R^2	Factor α	Achieved amplitude $[\mu m]$	σ_f $[MPa]$	σ_f/σ_{max}
1	0.997	0.86	49.7	203.8	0.85
2	0.997	0.84	66.4	322.6	0.99
3	0.997	0.86	53.4	248.6	0.95
4	0.997	0.86	54.1	249.0	0.94
5	0.994	0.80	26.0	85.3	0.68
6	0.996	0.85	48.5	236.4	0.99
7	0.986	0.85	16.8	79.5	0.97
8	0.981	0.89	18.4	90.2	1.00

Alumina 99.5%

9	0.996	0.84	39.4	186.1	0.96
10	0.993	0.81	47.2	232.6	1.00

Table 6.8 also shows the fracture strength, corresponding to the one calculated on the critical defect, and its ratio to the maximum strength globally achieved on the specimen, defined as σ_f/σ_{max}. Accordingly, if a risk-volume for alumina 99.5% were to be calculated based on this experimental dataset, it should correspond to the volume of material withstanding at least 68% of the maximum stress, which is a rather low value when compared to the 90% often adopted in VHCF tests [7], representing further evidence to the already expected defect susceptibility of alumina. In this case, if the threshold for calculating the risk-volume were to be adopted as the lowest measured ratio σ_f/σ_{max}, then it would be $V = 9817\ mm^3$, while the commonly adopted threshold of 90% would result in $V = 5301\ mm^3$, both of which are considered large values when conducting size effect analyses [7,8].

According to the supplier datasheet, the material strength value was measured through 3-point bending, being 490 MPa, with no indication of testing configuration and specimen geometry. However, upon further contact with the supplier, updated data was obtained for the material, from 3-point bending tests following the norm JIS R1601:2008 [9], for 30 mm and 40 mm span between supports, both concerning rectangular cross-section specimens of 3 mm height and 4 mm width. The supplier results are compared to the results obtained in the UST test in Table 6.9, with mean strength defined by the supplier as the specimen ultimate strength while the mean strength for the UST test corresponds to the fracture strength σ_f.

Table 6.9 Comparison of strength data and risk-volumes for alumina in different test configurations.

Test configuration	Mean strength $[MPa]$	Risk-volume at $0.9 \cdot \sigma_{max}\ [mm^3]$	Risk-volume at $0.68 \cdot \sigma_{max}\ [mm^3]$
UST	193.4	5301	9817
3-point bending, 40 mm span	340	1.2	14.2
3-point bending, 30 mm span	440	0.9	10.6

Alumina 99.5%

Given the relationship between risk-volume and material strength, as detailed in Section 1.2, it is expected that the supplier testing configuration will obtain considerably larger values for alumina strength. Indeed, Table 6.9 shows that the risk-volume in the UST test is over two orders of magnitude larger than both 3-point bending configuration.

6.8. Stress Intensity Factors

Finally, following the SIF calculation methodology defined in Section 3.3, the critical defect size can be quantitatively correlated with the fracture strength. Following Eq. 3.3, $\sigma_f\sqrt{\sqrt{A_c}}$ is plotted in function of $\sqrt{A_c}/\emptyset$, being $\emptyset = 10\ mm$, for the alumina specimens, resulting in Fig. 6.12a, allowing the estimation of a fitting curve, corresponding to the function $1/Y$. After the empirical estimation of $K_{I,d}$ according to Eq. 3.2, the graphic in Fig. 6.12b is generated, representing SIF values that tend to be constant at C with the critical defect size, as dictated by the empirical equation.

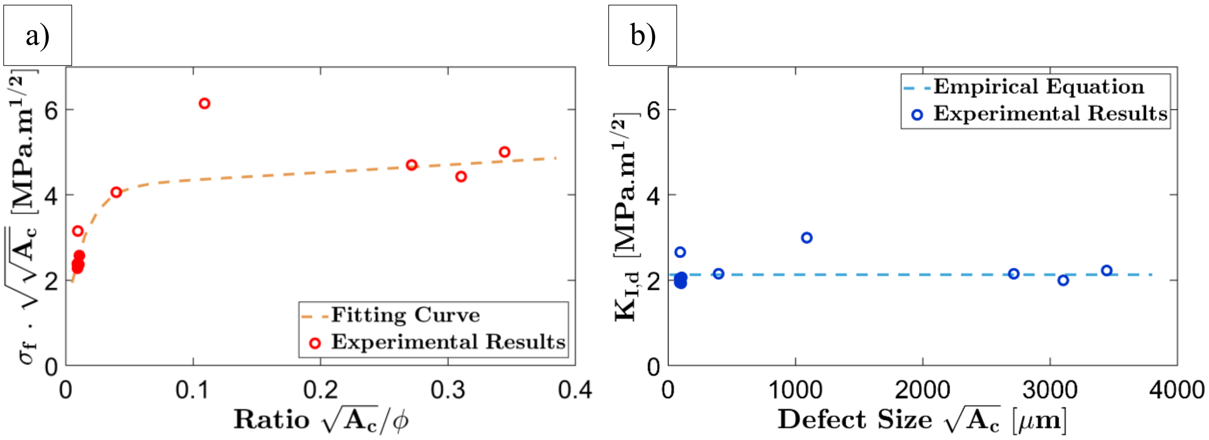

Figure 6.12 Correlation between σ_f *and* $\sqrt{A_c}$ *for alumina, being (a) the raw data and the respective fitting, and (b) the data applied to the empirical formulation for the SIFs. The filled markers represent the four specimens used to calculate the constant* C*.*

The empirical formulation resulting in Fig. 6.12b follows Eq. 6.1, for the alumina specimens:

$$K_{I,d} = 2.13 \cdot \frac{1}{4.19 \cdot e^{0.387 \cdot \frac{\sqrt{A_c}}{\emptyset}} - 3.12 \cdot e^{-65.1 \cdot \frac{\sqrt{A_c}}{\emptyset}}} \cdot \sigma_f\sqrt{\sqrt{A_c}} \tag{6.1}$$

Particularly, the estimation of the constant $C = 2.13\ MPa \cdot m^{1/2}$ only took into account specimens 3, 4, 6 and 10, highlighted in Fig. 6.12 through the filled markers, not considering the specimens whose critical defects were cracks or the inclusion, given Murakami's formulation limitations [10]. Furthermore, since specimen 2, although also only possessing pores as imperfections, resulted in a considerably higher fracture strength when compared to the other four, while having a similar critical defect size, it was not taken into account in this estimate to avoid influencing the SIF values by data that was too far from the mean.

Considering the whole set, Eq. 6.1 resulted in a mean SIF of $2.22\ MPa \cdot m^{1/2}$ with a standard deviation of $0.34\ MPa \cdot m^{1/2}$. The obtained values, although calculated using the values for the critical defect size, do not translate into the critical SIF, or fracture toughness K_{Ic}, since they correspond to an empirical formulation relating the strength and critical defect size measured through the methods explained in this work.

As a further comparison, the empirical formulation in Eq. 6.1 was applied to the 400 largest defects identified on each specimen, to calculate the SIF generated by the nominal tensile stress being produced at each defect position when failure happened. The graphics in Fig. 6.13 show the obtained results, with each specimen critical defect plotted in red.

Particularly, this analysis is to verify that the largest value of $K_{I,d}$ in the respective specimen was also caused by its critical defect, potentially validating Eq. 6.1. This does seem to be the case for all the specimens containing cracks (5, 7, 8, and 9), and for the specimen containing the inclusion (1). However, for the specimens that only presented pores (2, 3, 4, 6, and 10), although the value for the critical defect is generally among the highest, some cases, specifically specimens 3 and 4, showed SIF values up to 14% larger than their respective critical ones, which could cast doubt on the validity of Eq. 6.1, indicating the influence of factors other than the size, such as shape, distance to the material surface, and distribution within the material, which could cause two smaller defects close to each other to be more critical than if just one slightly larger defect were in that same place.

Nevertheless, the formulation accurately predicts failure when severe defects are involved, which correspond to the extreme situations, where the strength levels are the lowest, while also providing a sufficiently good approximation in their absence. Therefore, it can still be applied to component design while also maintaining its simplicity, since it depends only on the defect and component sizes.

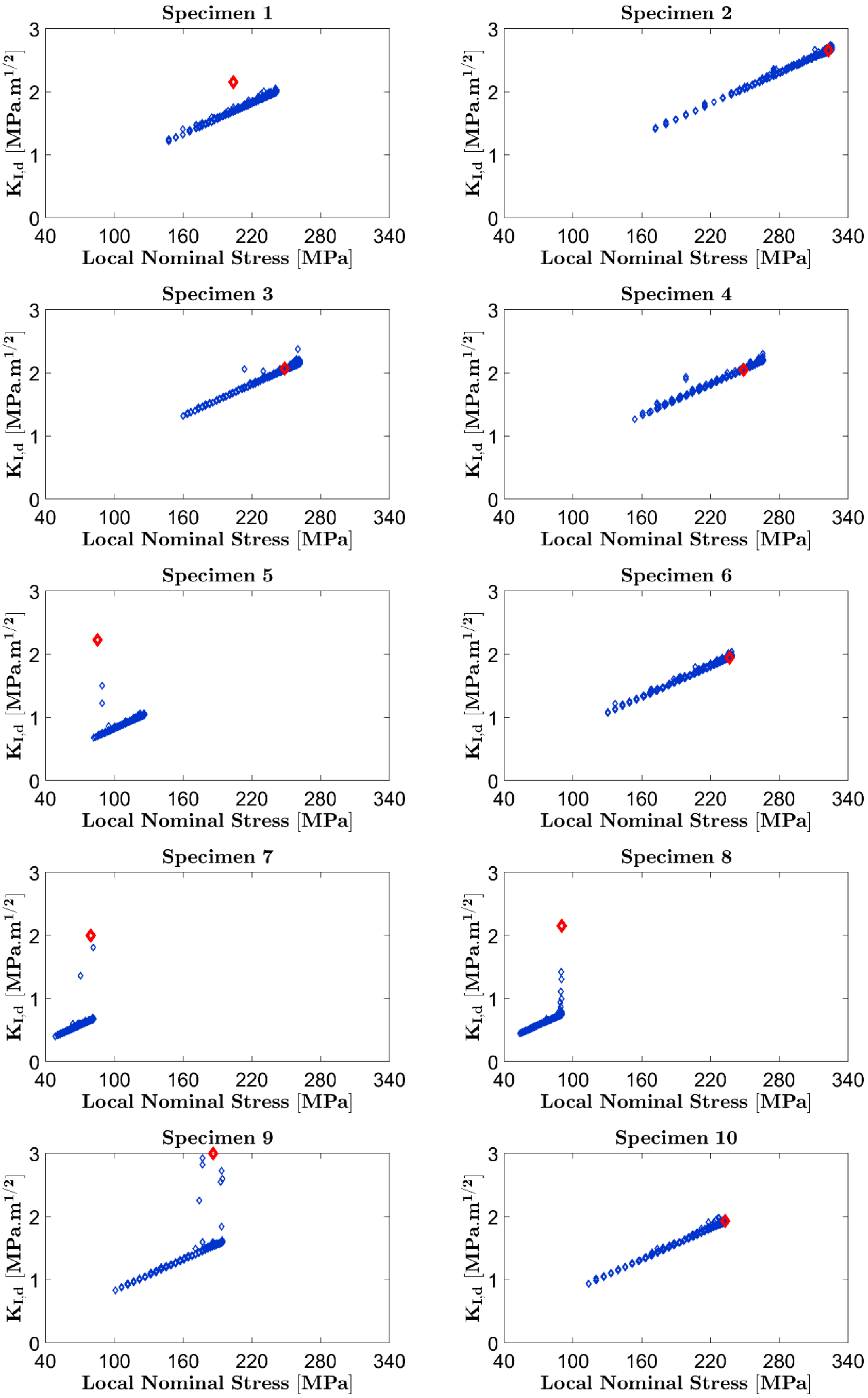

Figure 6.13 SIF at fracture on each alumina specimen for the 400 largest identified defects, with the critical defect being highlighted in red.

6.9. References

[1] T. Jiao, Y. Li, K. T. Ramesh, and A. A. Wereszczak, “High Rate Response and Dynamic Failure of Structural Ceramics,” *Int. J. Appl. Ceram. Technol.*, vol. 1, no. 3, 2004.

[2] J. Seidel, N. Claussen, and J. Rödel, “Reliability of alumina ceramics: Effect of grain size,” *J. Eur. Ceram. Soc.*, vol. 15, no. 5, pp. 395–404, 1995, doi: 10.1016/0955-2219(95)91430-V.

[3] B. . T. and E. D. C. K.-Y. Lee, L.C.G. Cropsey, “Grain size, density, and mechanical properties of alumina batch-processed in a single-mode microwave cavity,” *Mater. Res. Bull.*, vol. 32, no. 3, pp. 287–295, 1997.

[4] G. Nie, Y. Bao, D. Wan, and Y. Tian, “Measurement of the high temperature elastic modulus of alumina ceramics by different testing methods,” *Key Eng. Mater.*, vol. 768, 2018, doi: 10.4028/www.scientific.net/KEM.768.24.

[5] D. Kotsanis, P. Nomikos, and D. Rozos, “Comparison of Static and Dynamic Young’s Modulus of Prasinites,” p. 54, 2021, doi: 10.3390/materproc2021005054.

[6] W. de A. Thomaz, D. Y. Miyaji, and E. Possan, “Comparative study of dynamic and static Young’s modulus of concrete containing basaltic aggregates,” *Case Stud. Constr. Mater.*, vol. 15, 2021, doi: 10.1016/j.cscm.2021.e00645.

[7] A. Tridello, D. S. Paolino, and M. Rossetto, “Ultrasonic VHCF tests on very large specimens with risk-volume up to 5000 mm^3,” *Appl. Sci.*, vol. 10, no. 7, Apr. 2020, doi: 10.3390/app10072210.

[8] A. P. Pagnoncelli, A. Tridello, and D. S. Paolino, “Modelling size effects for static strength of brittle materials,” *Mater. Des.*, vol. 195, Oct. 2020, doi: 10.1016/j.matdes.2020.109052.

[9] “JIS R1601:2008 - Testing method for flexural strength (modulus of rupture) of fine ceramics at room temperature,” *Japanese Ind. Stand. / Japanese Stand. Assoc.*, 2008.

[10] Y. Murakami, *Theory of elasticity and stress concentration*. 2016. doi: 10.1002/9781119274063.

Alumina 99.5%

Chapter 7

7. Graphite R4550

In this chapter, the parameters for micro-CT and UST test on alumina will be specified, along with the particularities of the analysis methods for the experimental data and the numerical model, followed by the results presentation. The procedure defined for characterization of brittle materials was successfully applied to 16 hourglass specimens of graphite R4550.

7.1. Preliminary Material Characterization

The graphite specimens were initially characterized through simple measurements, as in the alumina case, with its dimensions and weight being verified, resulting in the density value reported in Table 7.1. Additionally, the specimens longitudinal natural frequency was verified though IET, resulting in the mean value of $20971\ Hz$, which could represent an issue since it is outside the machine operating range. However, the horn-specimen system frequency should be within the range for the test to be possible, with the horn having considerably larger mass and dimensions than the specimen, its frequency is expected to mostly dictate the system, keeping it at the desired overall value. Therefore, the only remaining concerns were the specimen itself not going into the resonance state and the generation of excessive tension on the adhesive, which, upon the tests execution, were verified not to be issues.

Table 7.1 Preliminary characterization of graphite specimens.

Property	Mean	Standard deviation
Density $[kg/m^3]$	1830	4.6
Frequency $[Hz]$	20971	27

In addition to the values in Table 7.1, the elastic modulus, considering a linear-elastic material, was numerically estimated through Ansys Workbench harmonic response analysis, producing a value of $11.8\,GPa$, considerably larger than the $10.9\,GPa$ used in the design. With the resulting density being similar to the one originally employed, the variation in elastic modulus is the reason for the unexpectedly high natural frequency.

7.2. Defect Characterization Parameters

Graphite caused slightly more difficulty in the configuration of the CT-scanner for the acquisition of good quality projections. Its relatively low density showed a tendency of causing noise in the final reconstructions. To avoid this, the x-ray beam was not filtered, and the detector was positioned very closely to the tube, with SDD at only $750\ mm$, as shown in Table 7.2. This way, the material would be able to attenuate a higher percentage of the x-rays intensity, improving the contrast and, therefore, reducing the noise.

Table 7.2 CT-scanner configuration adopted for the graphite specimens.

Parameter	Set value
Tube current $[\mu A]$	100
Tube voltage $[kV]$	60
Exposure time $[s]$	1.0
SOD $[mm]$	32 (64)
SDD $[mm]$	750
Filter	none
Number of projections	1600 (800)

In Table 7.2, the parameters having values between parenthesis are those that were not the same in the original scans and the ones conducted after the ultrasonic test. In the original scans, the resolution was higher, at $8.53\ \mu m$, with more projections, while rescans acquired half the number of projections and doubled SOD, also doubling the resolution value. This decision was made to reduce scanning time, since the main goal with the rescans was to define the fracture surface position, while the originals had high quality and resolution to allow an accurate defect analysis. Moreover, according to the observations in Section 3.3, the resolution from the original scans should provide proper identification of defects that respect $\sqrt{A} \geq 34.12\ \mu m$, still larger than the expected grain sizes for ultra-fine grain graphites, such as R4550, ranging from $1\ \mu m$ to $30\ \mu m$, as pointed out by literature data [1,2].

Since these specimens are relatively short, at $30.9\ mm$ of total length, only one scan should be enough to capture the entire risk-volume, acquiring the specimen central zone, as in Fig. 7.1, indicating the scanned dimension. All the specimens had a length of at least $12.7\ mm$ scanned in high quality, allowing a reliable defect analysis with high likelihood of containing the fracture surface.

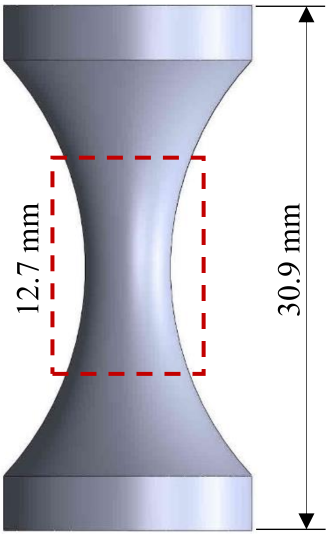

Figure 7.1 CT-scanned portion of the graphite specimen compared to its full length.

Once the scans were collected and the reconstructions obtained, the defect analyses, according to described in Section 3.2, were conducted, to verify the presence of voids and inclusions. Once the primary types of defects were identified through a few tentative analyses, it was established that all specimens would be well characterized with a void analysis using the custom probability criterion, whose factors weights are reported in Table 7.3.

Table 7.3 Probability factors used for defect analysis on graphite.

Factor	Scaled deviation	Ignore small defects	Sphericity	Constant
Value	0.50	0.50	0.50	1.00

As reported in Table 7.3, showing all the factors whose weights were attributed non-zero values, scale deviation was adopted as 0.5, since it checks the deviation of the defect candidates gray levels regarding their surroundings, or the contrast levels. Moreover, the factor to ignore small defects was also used, to avoid selecting defects that occupy too few voxels for an accurate measurement, which could also cause image noise to be identified as defects.

Finally, sphericity (Φ), also given a 0.5 weight, is calculated as the ratio between the surface of the smallest sphere containing the defect (S_s) and the defect surface (S_d), according to Eq. 7.1. This factor was used since preliminary evaluations showed the complete absence of large cracks and excessively elongated pores. Therefore, its use does not incorrectly eliminate defect candidates, while also contributing to eliminating defect candidates that are actually noise, and generating smoother contours on real defects, since it treats them more like pores rather than cracks.

$$\Phi = \frac{S_s}{S_d} \tag{7.1}$$

7.3. Defect Characterization Results

Unlikely alumina, graphite showed no cracks or inclusions as imperfections, only pores. They were generally uniformly distributed and all below $120\ \mu m$ in size, assuming one of two shapes: approximately spherical, probably caused by trapped gas within the raw mixture before pressing, and more random shapes, in correspondence to low material density areas, where the x-rays attenuation is lower than the material but higher than the background, probably indicating poor bonding between grains. Contrary to alumina rods, graphite specimens did not present elongated pores in a specific direction, which is expected, since R4550 is produced through isostatic pressing.

These results are exemplified by Fig. 7.2, showing specimen 12, with Fig. 7.2a corresponding to the defect area graphical representation on the original scan, with dimensions as in Fig. 7.1, overlapped with the two broken pieces rescanned after the ultrasonic test, with the fracture surface generated very close to the specimen center. Moreover, Fig. 7.2b and Fig. 7.2c illustrate the two described types of pores found in graphite specimens. Since hourglass specimens considerably reduce the material risk-volume when compared to constant cross-section ones, all graphite specimens failed near their centers, around their halfway lengths, as shown in Fig. 7.2a, which is also expected when considering that no particularities were identified among the analyzed imperfections.

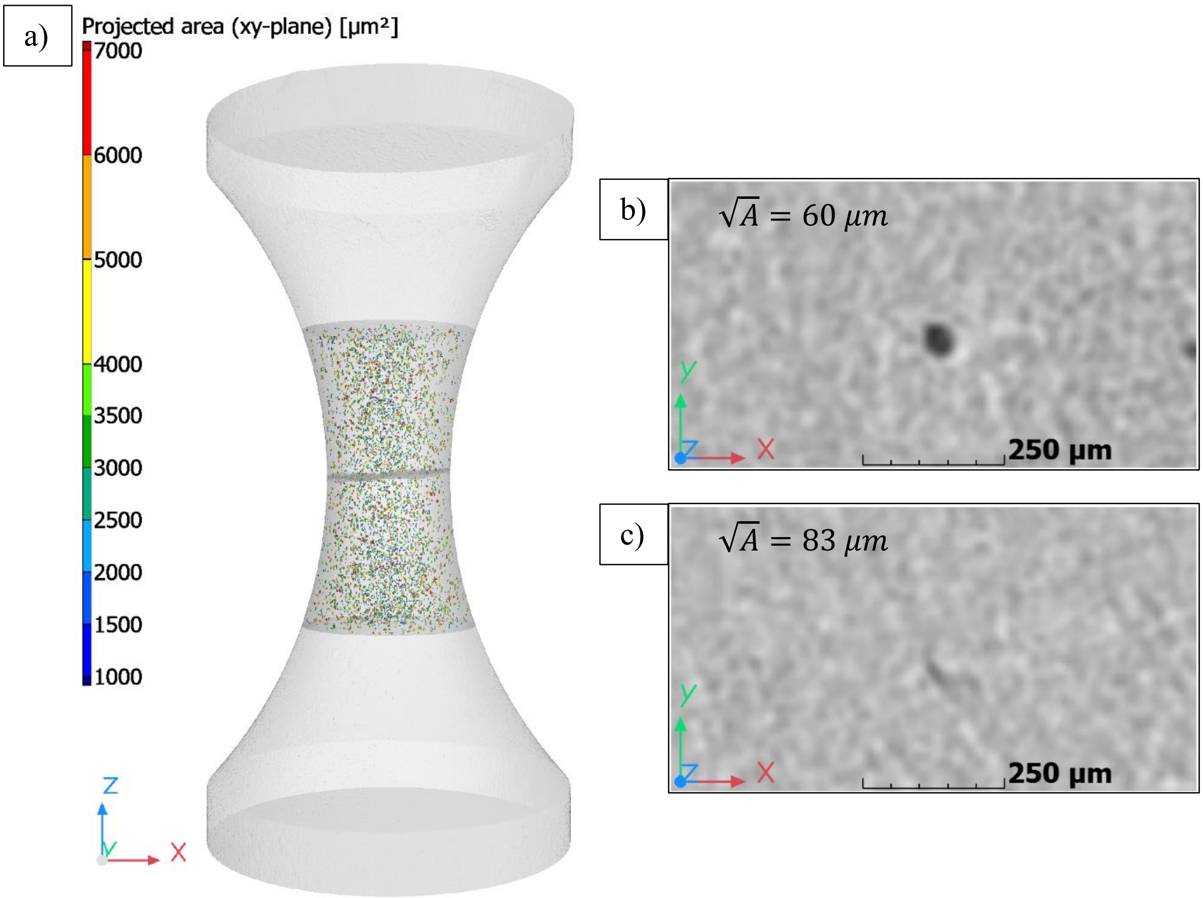

Figure 7.2 Micro-CT data for graphite specimen 12, showing (a) the 3D image for the original scan with defect analysis overlapped with the rescanned pieces, (b) a highly spherical pore, and (c) an irregularly shaped pore.

Once the rescans are conducted and overlapped with the originals, the critical defect can be selected through the method described in Section 3.3, being illustrated for the graphite specimens in Fig. 7.3, showing the cross-section containing the critical defect of specimen 12. In Fig. 7.3, it can also be perceived that the scan is more detailed in the original, with better quality and sharpness, which are reduced on the rescans due to the lower resolution and number of acquired projections.

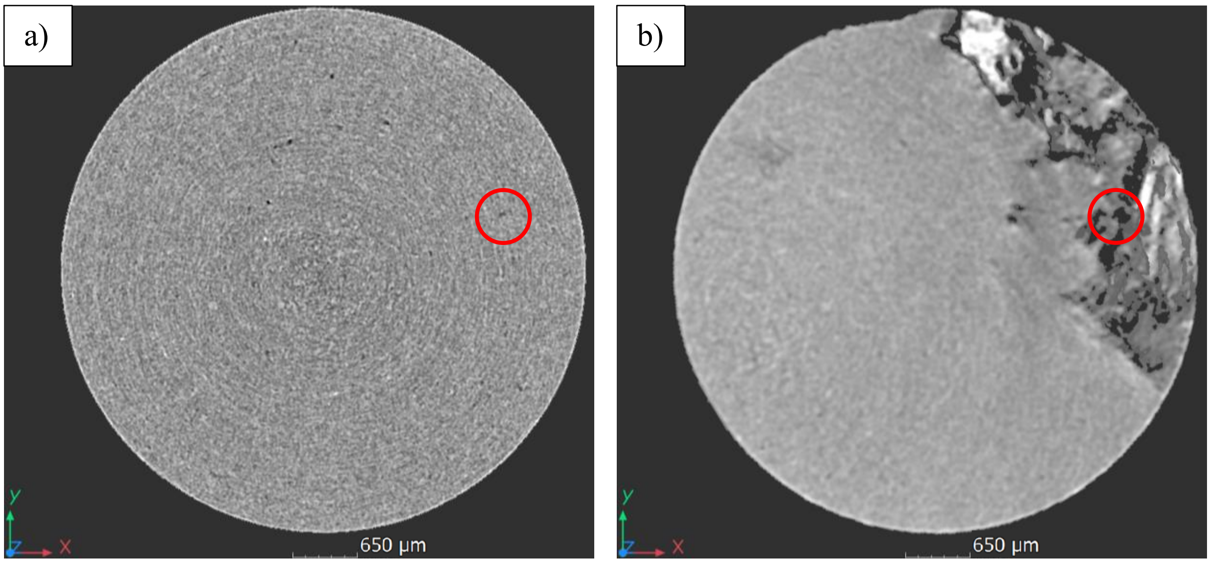

Figure 7.3 Graphite specimen 12 critical defect indicated in red (a) on the original scan, and (b) on the fracture surface.

Table 7.4 reports the results obtained for graphite, with specimen 1 being the only one having its critical defect being also the largest, showing that the largest defect is almost never the critical. Nevertheless, this was anticipated, since the scanned material volume is expected to be considerably larger than the risk-volume, to guarantee that the critical defect would be properly analyzed.

Table 7.4 Defect analysis results for each graphite specimen, comparing their respective critical and largest defects.

Specimen	Critical defect size [μm]	Largest defect size [μm]
1	112	critical = largest
2	84	96
3	92	98
4	84	93
5	86	117
6	85	99
7	99	105
8	93	96
9	89	100

Graphite R4550

10	94	105
11	89	101
12	85	96
13	82	91
14	92	101
15	93	114
16	84	91
Mean	90	101

Finally, all 32 fracture surfaces were observed through FESEM to verify the possibility of crack propagation, which could indicate fatigue. In all observations, the fracture surfaces had an aspect as shown in Fig. 7.4a, being impossible to determine where failure started or to identify its path, hence, suggesting no evidence of fatigue. Moreover, the microstructure of R4550 was also observed, as in Fig. 7.4b, being shown to possess the usual morphology of isostatically pressed graphites, according to those found in the literature [1,2].

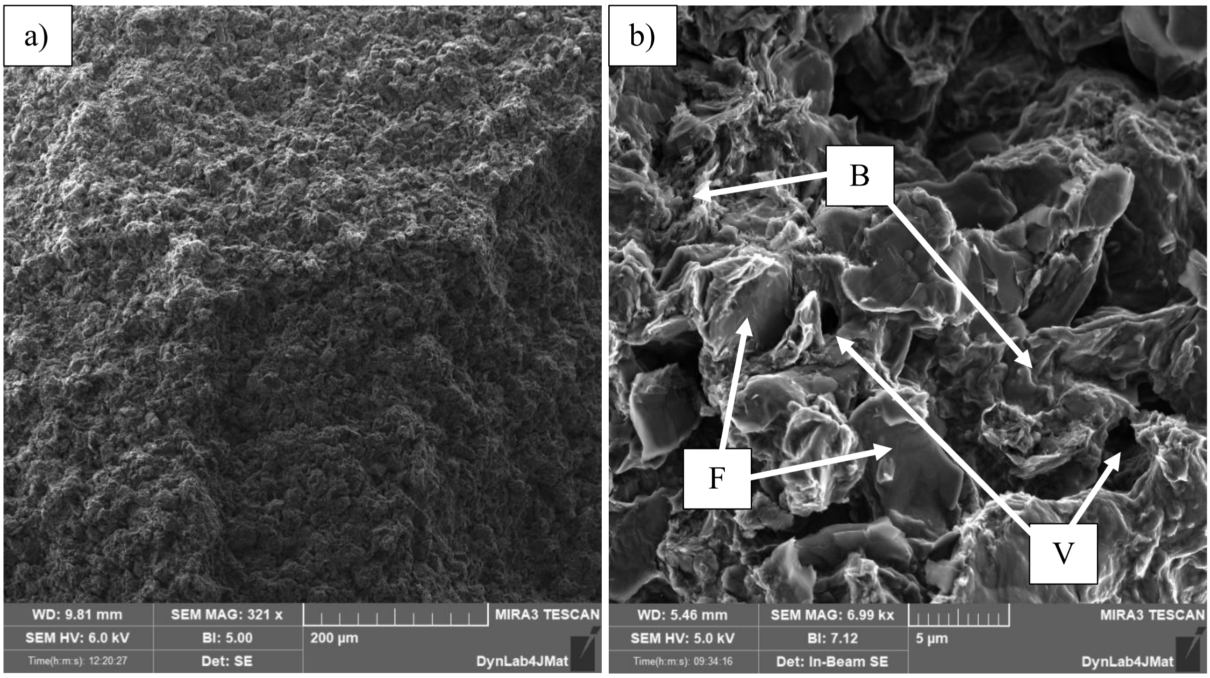

Figure 7.4 FESEM images of graphite specimen fracture surfaces, illustrating (a) their general aspect, and (b) their microstructure indicating filler (F), binding carbon (B), and void (V).

Fig. 7.4b shows similar structures to those identified on fracture surface morphology of isostatic graphite for nuclear applications (SNG623) in [1], specifically:

- the flat and smooth surfaces, corresponding to filler particles split by trans-granular fracture (F), in this case measuring around $10\ \mu m$, being within the expected range for ultra-fine grain graphites of $1 - 30\ \mu m$;
- the rougher areas resulting from intergranular fracture, relative to either pure binding carbon or biding carbon attached to filler particles that were not split during fracture (B);
- the voids that were produced during manufacturing or due to the dislodging of filler particles during failure (V), in this case too small to be identified through CT-scan, measuring less than $5\ \mu m$.

7.4. Ultrasonic Tensile Test Parameters

The specific parameters for the UST test on graphite are reported in Table 7.5, with the output frequencies being those measured through horn signature, corresponding to the horn-specimen system natural frequencies. It can be observed that, although the specimens by themselves were all above the machine operating frequencies, the horn-specimen system still remained within the desired range. Meanwhile, the output amplitude of $4\ V$ was verified to be able to fracture the specimens, since it should be able to produce a normal stress amplitude of $97\ MPa$, which is the value calculated using the updated elastic modulus of $11.8\ GPa$ measured through IET, as detailed in Section 7.1.

Table 7.5 UST test parameters for graphite.

Specimen	Output frequency f_{out} $[Hz]$	Output amplitude $[V]$	Maximum stress $[MPa]$	Camera resolution $[\mu m]$
1	20251	4	97	26.6
2	20240			27.1
3	20251			26.3
4	20246			27.2
5	20165			27.1
6	20252			27.3
7	20238			26.7
8	20210			27.2
9	20180			27.2
10	20224			27.2
11	20194			27.2
12	20228			27.2
13	20187			27.2
14	20237			27.3
15	20231			27.3
16	20233			27.1
Mean	20223	-	-	27.1

Moreover, the mean pixel size of the camera frames was measured as $27.1\ \mu m$, corresponding to a recorded length of the specimen of $13.9\ mm$, which allows the frame to be positioned symmetrically at the specimen center, as indicated in Fig. 7.5, showing both the camera and the broken specimen with its top half still attached to the horn and the bottom one laying on a support. This configuration will likely be able to capture the fracture surfaces in all tests, as indicated through the schematics showing a frame after failure occurred, in scale with the specimen geometry, while also being able to record relatively high displacements closer to the frame top and bottom extremities.

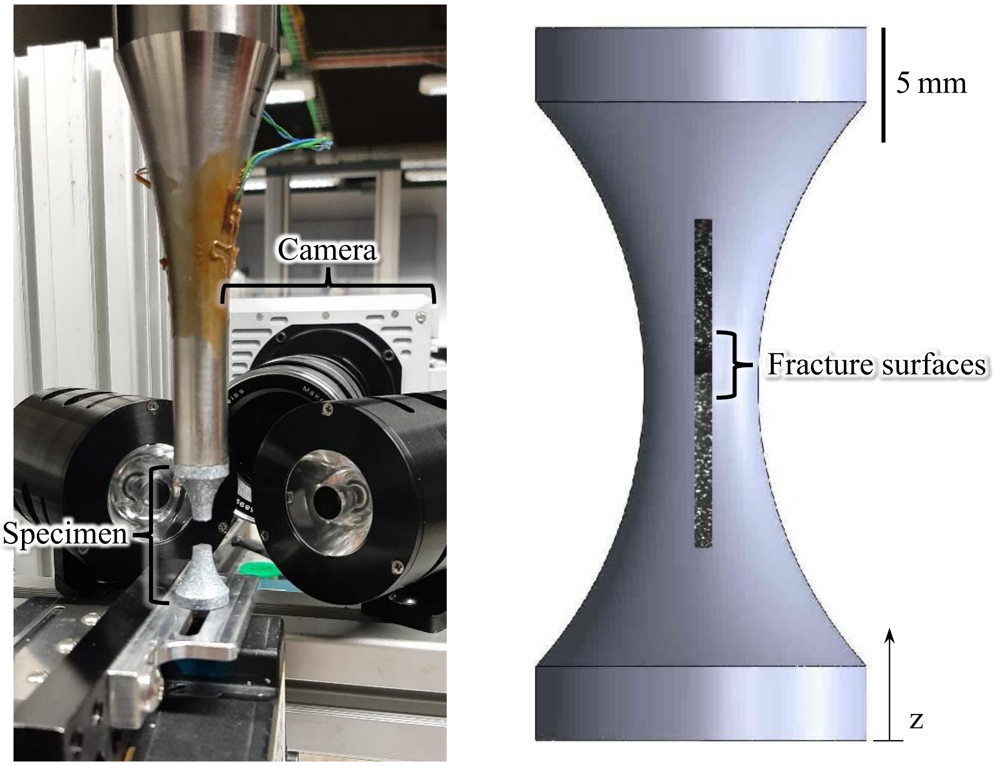

Figure 7.5 Positioning of the high-speed camera on graphite specimens.

7.5. Ultrasonic Tensile Test Results

Through the analyses of the camera recordings, it was observed that none of the specimens was detached from the horn before failure, while the fracture surfaces were successfully captured in all tests. The graphics for the displacements in z-direction could be plotted to qualitatively evaluate their experimental behavior in search for a material model that could simulate it. Specifically, the evolution for specimen 16 displacement curves can be observed in Fig. 7.6a, as an illustration of the general behavior measured in all the conducted tests on graphite, demonstrating that the specimens indeed went into longitudinal resonance state despite the difference in their IET natural frequency and the machine output frequency f_{out}. The legend shows the position of points whose displacements were calculated on the recorded frame, also corresponding to the positions of the FEM nodes, being node 9 located on the central-cross section.

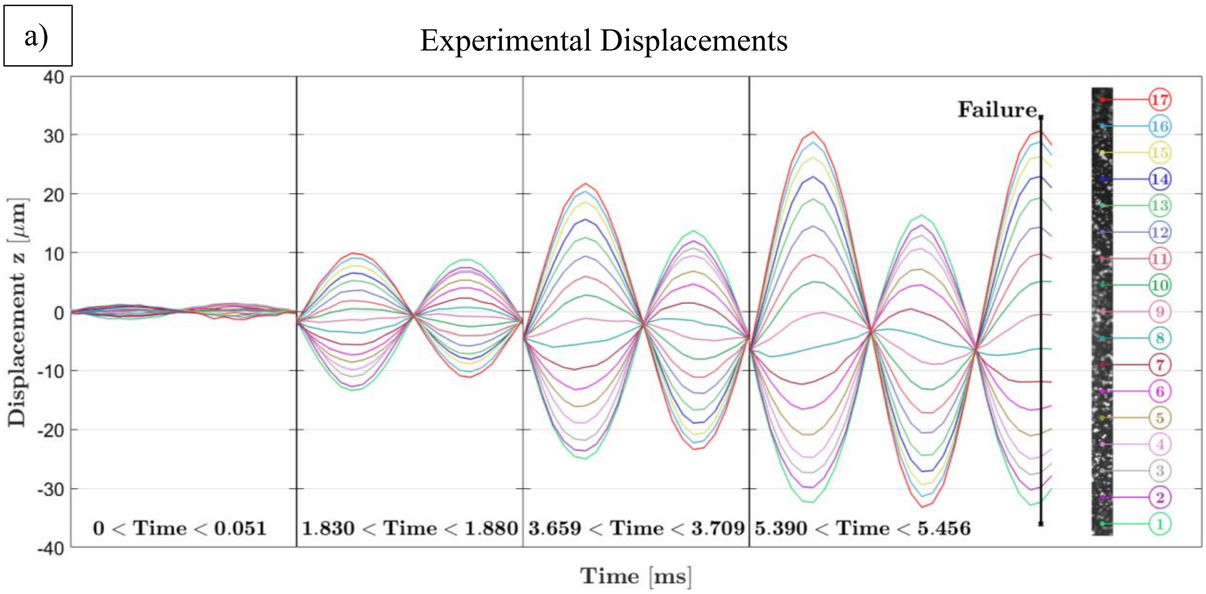
a) Experimental Displacements

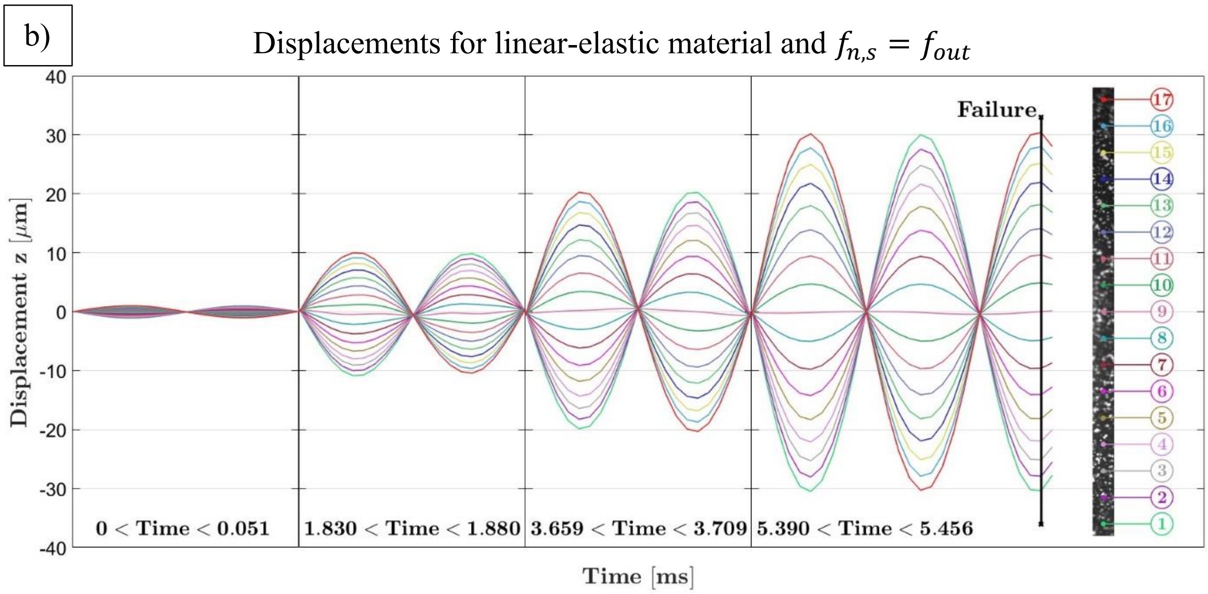
b) Displacements for linear-elastic material and $f_{n,s} = f_{out}$

Figure 7.6 Displacements for the tracked nodes of specimen 16 at different time ranges up to failure, being (a) the experimental curves and (b) the simulation closest to the ideal resonance condition using a linear-elastic material model.

Similarly, Fig. 7.6b plots the numerical results for the same nodes when adopting the same boundary conditions as in Fig. 7.6a, and defining graphite as linear-elastic. This material model uses the measured density value of $1830\ kg/m^3$, according to Section 7.1, while the adopted elastic modulus is $11.0\ GPa$, which corresponds to the value calculated so that the simulated specimen would have the same natural frequency as the machine output for specimen 16, i.e.,

$f_{n,s} = f_{out} = 20.23\ Hz$. Therefore, Fig. 7.6b is close to the ideal resonance condition, where the displacement node is located on the central cross-section, in this case on node 9, i.e., $u_{z,9}(t) = 0$, being $u_{z,i}(t)$ the displacement in z over time of node i, with curves 1 to 8 being in counterphase with respect to curves 10 to 17. Hence, for each cycle, all the FEM nodes located above the displacement node have their peaks at the same time as FEM nodes located below it have their valleys, and vice-versa.

Therefore, the ideal resonance condition, according to the analytical equations from Section 2.2, should result in $u_{z,1}(t) = -u_{z,17}(t)$, $u_{z,2}(t) = -u_{z,16}(t)$, $u_{z,3}(t) = -u_{z,15}(t)$, $u_{z,4}(t) = -u_{z,14}(t)$, $u_{z,5}(t) = -u_{z,13}(t)$, $u_{z,6}(t) = -u_{z,12}(t)$, $u_{z,7}(t) = -u_{z,11}(t)$, and $u_{z,8}(t) = -u_{z,10}(t)$, being $u_{z,i}(t)$ the displacement curve i. Although minor variations are expected on these equalities, e.g., $u_{z,9}(t)$ shows slight fluctuations, caused by the boundary condition consisting of a ramp instead of regime, and by numerical approximations used in the model, it is still true that $u_{z,9}(t) \cong 0$, as well as $u_{z,1}(t) \cong -u_{z,17}(t)$, and so on.

However, the tested specimens are expected to have $E > 11.0\ GPa$, which will result in $f_{n,s} > f_{out}$, causing the displacement node to be located slightly above point 9, more specifically between nodes 9 and 10 for linear-elastic specimens with natural frequencies up to 21.5 kHz. Although the difference between $f_{n,s}$ and f_{out} in a linear-elastic model is not enough to change the phases of the curves nor their individual symmetry to the zero abscissa, they do change the amplitudes of the curves, e.g., $U_{z,9} > 0$, $U_{z,1} > U_{z,17}$, and so on, being $U_{z,i}$ the amplitude of curve i.

Additionally, the experimental results in Fig. 7.6a show multiple characteristics that are likely caused by nonlinearities of the material. First of all, they do not suggest the existence of a displacement node, originally expected to be in correspondence to node 9 for the ideal resonance condition, or between nodes 9 and 10 in case of a linear-elastic material and a specimen with $f_{n,s} > f_{out}$, as previously explained. Among all observed results, node 8 was the one to have the lowest displacement amplitudes. Additionally, instead of having the curves above the displacement node in phase with each other, and, at the same time, in counterphase with those below the displacement node, as demonstrated by Fig. 7.6b, the phases in Fig. 7.6a seem to change slightly from one node to its neighbor, still amounting to curves 1 and 17 being almost in counterphase.

Furthermore, given the UST configuration, even in the case where $f_{n,s} \neq f_{out}$, each node displacement is expected to have the zero abscissa as axis of symmetry. However, it is observed that the curves do not actually have an axis of symmetry, since they seem to shift downwards as their amplitudes increase. Fig. 7.6a suggests that the curves axis of symmetry is at $0\ \mu m$ for the range $[0, 0.051]\ ms$, progressively decreasing until around $-5\ \mu m$ at the range $[5.390, 5.456]\ ms$.

Furthermore, ultrasonic tests apply alternated tension and compression on the specimen. This can be observed in Fig. 7.6a through points 1 and 17. When the former assumes negative values and the latter positive ones, the specimen is in tension, when the reverse happens, it means compression is applied. With this, it can be noticed that specimen 16 breaks while being submitted to tension, also verified to be true for all the remaining specimens, which is both expected and desired.

Finally, given the symmetry of the load caused by the longitudinal resonance condition, i.e., the magnitude of the load in tension and in compression is similar around the same instant of the ramp, resulting in $max\{u_{z,17}\} - min\{u_{z,1}\} \cong max\{u_{z,1}\} - min\{u_{z,17}\}$ within the same cycle, which is the case for Fig. 7.6b. However, the difference in displacement between nodes 1 and 17 in Fig. 7.6a is larger in tension than in compression, i.e., $max\{u_{z,17}\} - min\{u_{z,1}\} > max\{u_{z,1}\} - min\{u_{z,17}\}$. Consequently, if the same force is causing larger displacements in tension than in compression, it likely means that R4550 has a smaller elastic modulus in tension than in compression.

Through the experimental data calculation, it was also possible to obtain the results reported in Table 7.6. If R4550 were a linear-elastic material, in the ideal regime resonance condition, the laser should measure around $48\ \mu m$ of displacement amplitude with the zero abscissa as axis of symmetry. However, Table 7.6 demonstrates that the laser detected in all tests the same behavior noticed in Fig. 7.6a, where the displacement curves seem to progressively translate downwards as the amplitudes increase, causing the magnitude for minimum displacement to be considerably larger than that of maximum displacement. Nevertheless, even considering this nonlinearity, none of the tests seem to have reached the regime amplitude, which is further confirmed by the tests durations being all below $10\ ms$.

Table 7.6 UST test experimental results for graphite.

Specimen	Laser maximum $[\mu m]$	Laser minimum $[\mu m]$	Number of cycles	Test duration $[ms]$	Fracture surface position z $[mm]$

1	22.9	-36.1	110	5.4	15.08
2	26.8	-42.5	140	6.9	17.30
3	21.5	-43.6	114	5.6	13.66
4	24.5	-42.1	138	6.8	15.51
5	24.1	-42.5	139	6.9	15.28
6	24.0	-37.8	116	5.7	15.39
7	23.2	-36.7	87	4.3	15.29
8	27.7	-41.9	124	6.1	15.21
9	29.1	-40.4	113	5.6	15.74
10	23.8	-37.4	128	6.3	15.68
11	25.4	-36.8	106	5.2	16.45
12	25.1	-34.4	113	5.6	15.74
13	25.3	-39.7	98	4.9	16.12
14	23.1	-33.7	103	5.1	13.51
15	23.8	-37.4	129	6.4	14.85
16	26.9	-37.4	111	5.5	17.06

Furthermore, Table 7.6 also shows that the specimens withstood at most $140\ cycles$, which, added to low displacement amplitudes at the test beginning, makes it acceptable to assume fatigue damage is negligible. Finally, the fracture surface position is reported, being determined through the critical defect identification, considering $z = 0$ at the specimen free extremity, where the laser is located. Remarking that the specimen center is on $z = 15.45\ mm$, all of them failed close to that position, which is expected, since the hourglass geometry considerably reduces the risk-volume when compared to constant cross-section.

7.6. FEM Setup

As highlighted in Section 7.5, through the observation of the displacement curves as in Fig. 7.6, the material model to simulate graphite R4550 should be able to reproduce the phase behavior of the curves, the lack of a displacement node, the vertical translation of their supposed axis of symmetry, and the difference in response between tension and compression. The two first mentioned effects are likely due to viscoelasticity, also identified in split Hopkinson pressure bar tests from [3], following the shear relaxation described by [4]:

$$G(t) = G_{\infty} + (G_0 - G_{\infty})e^{-\beta t}, \tag{7.2}$$

being G the shear modulus at time t, G_0 the short-term or instantaneous shear modulus, G_{∞} the long-term or infinite shear modulus, and β is the decay constant. The delay caused by the relaxation was verified to alter the phases in the same way as in Fig. 7.6a, which also eliminates the existence of a node where displacements are always zero.

However, the model described by Eq. 7.2 alone should not be able to reproduce graphite asymmetrical behavior in tension and compression. For this reason, the application of a hyperelastic model was considered, having as defining features the increase in elastic modulus during compression, and its decrease during tension, also proving to be effective for compressed expanded graphite [5] and for graphene [6,7]. Nevertheless, these changes only start to happen once relatively high strains are involved, above 10%, both for tension and compression, as in [8], which is not the case for ultrasonic tests, whose largest strains produced on graphite specimens could be roughly estimated through the tracker results, producing values between 0.5% and 1%. To allow the reproduction of this effect at low strains, a material allowing the setup of linear-elasticity with two elastic moduli, one for tension (E_t) and one for compression (E_c), was chosen.

To illustrate the behavior of the adopted model, the stress-strain for the central cross-section of the specimen is plotted in Fig. 7.7, i.e., the section presenting the largest strain values. The graph corresponds to the results obtained in a simulation using the parameters of the adopted material model after optimization, with the displacement at the horn-specimen interface following the form $u_{z,int}(t) = A_{out} \cdot t \cdot 10^2 \cdot sin(2\pi \cdot f_{out} \cdot t)$, for $0 \leq t \leq 0.01\ s$, $f_{out} = 20250\ Hz$, and $A_{out} = 48\ \mu m$. Being $u_{z,int}(t)$ a similar but simplified version of $\alpha \cdot g(t)$, as defined in Section 5.1, resulting in the amplitude ramping from 0 to a maximum amplitude of $48\ \mu m$ (considering $\alpha = 1$), corresponding to the theoretical boundary motion curve for the machine output of $4\ V$, as defined in Section 7.4, by Table 7.5. Additionally, in Fig. 7.7, the stress-strain curve measured on the last cycle of this simulation was highlighted in red to show the hysteresis introduced by this material model, as well as its capability of generating lower strains in compression than in tension under a similar load magnitude.

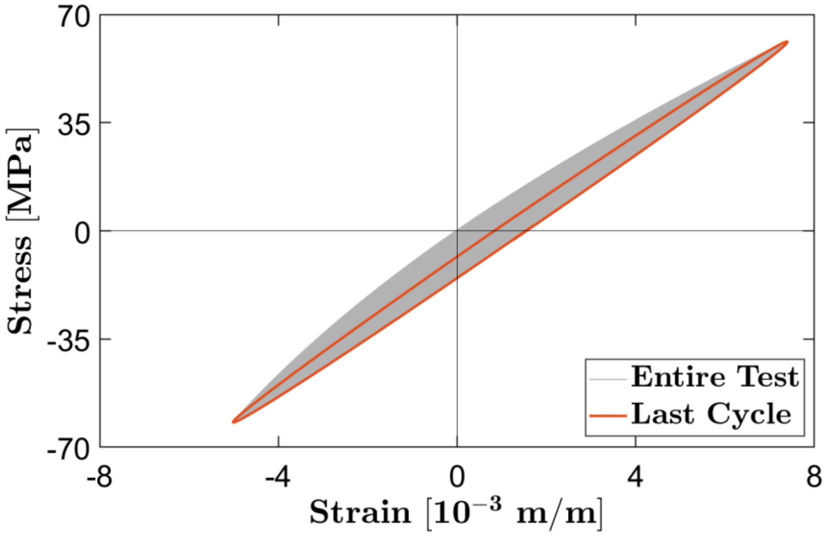

Figure 7.7 Illustration of the stress-strain curve on the cross-section considering the optimized FE model for the UST test on graphite R4550.

This same model also allows the addition of viscoelasticity, by setting up values for β, and $(G_0 - G_\infty)$, referred to as the shear relaxation modulus (G_1). With this, all the listed particularities in graphite behavior should be successfully simulated by the numerical model, through the optimization of 5 variables: factor α, from the boundary motion curve, E_t and E_c, from the linear-elastic part of the model, and G_1 and β, for the viscoelastic effect. Meanwhile, the Poisson ratio was used as 0.16, according to the literature on graphite R4550 [3], since changing its value within the acceptable range for this material does not significantly modify the results for uniaxial displacements, consequently making its optimization through the collected experimental data ineffective.

Finally, as optimization objectives, the displacement values measured through the tracker and the laser were used, with the laser result and each valid tracker result, with each objective curve given weight 1 when calculating the minimum square errors during optimization. Contrary to alumina case, the laser influence on the material properties is smaller this time, since the tension-compression asymmetry and viscoelasticity are also very pronounced on the tracker curves.

Furthermore, it was observed that optimization results improved by excluding all the curves from 6 to 10, according to Fig. 7.6, from the objectives. This improvement meant that the optimizaton variables that often did not converge were able to do so once the mentioned curves were eliminated from the procedure. This action was taken due to the displacements for the points closer to the specimen center being smaller, and therefore tending to present higher percentual error, which could incorrectly affect the calculated material properties even in the cases when optimization could otherwise find a convergence point.

7.7. FEM Results

Once the final material properties were established through the optimization in all specimens, the experimental displacements can be compared to the numerical ones, as presented in Fig 7.8, reporting specimen 16, with similar results achieved for all specimens. Fig. 7.8 indicates that the chosen material model and the optimized properties are capable of reliably reproducing graphite R4550 behavior in the UST test, simulating the effects of the tension-compression asymmetry and viscoelasticity.

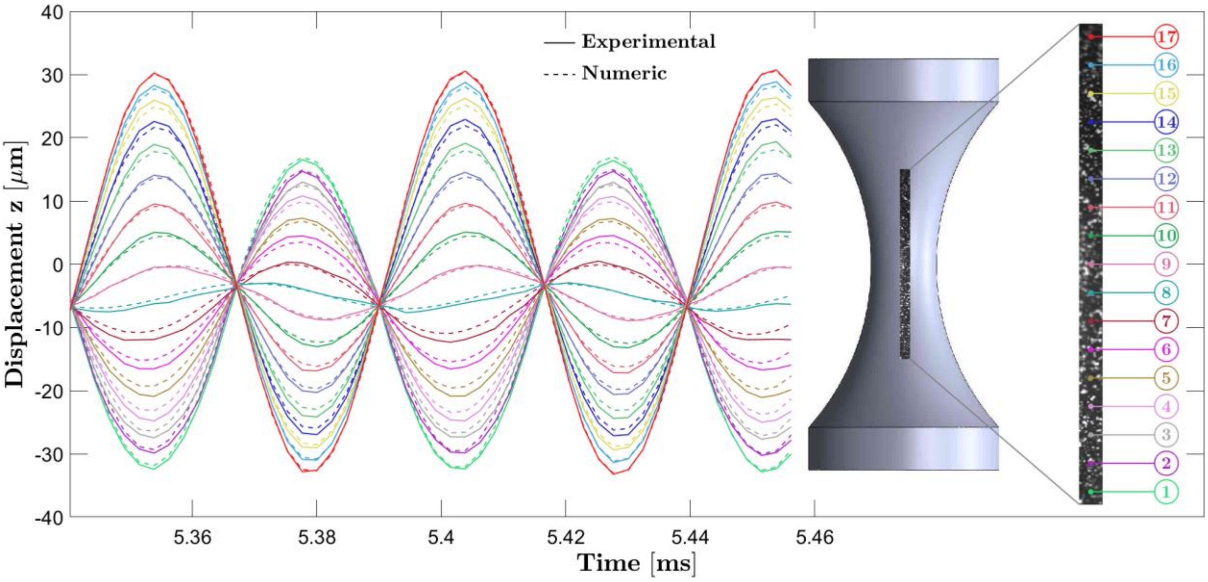

Figure 7.8 Comparison between the experimental displacement curves calculated through the tracker and those obtained through the numerical model for graphite.

The properties resulting from experimental measurements and the optimization process described in Chapter 5 and specified in Section 7.6 for graphite R4550 are reported in Table 7.7. The elastic moduli are 4.2% and 3.2% smaller, for tension and compression, respectively, than the 11.8 GPa calculated through IET, as in Section 7.1, which is expected given the nonlinearities concerning graphite behavior, also being in accordance with data from literature suggesting the progressive slight reduction in elastic modulus (E) with the increase in strain [9], whose experimental data from IET resulted in $E = 11.5\ GPa$.

Table 7.7 Graphite material properties.

Density $[kg/m^3]$	1830
Elastic modulus tension (E_t) $[GPa]$	11.31
Elastic modulus compression (E_c) $[GPa]$	11.42
Shear relaxation modulus (G_1) $[GPa]$	1.83
Decay constant (β) $[ms^{-1}]$	31.38

Furthermore, the results from Table 7.7 can be compared to those from the FEM of split Hopkinson pressure bar tests on R4550 [3], which used a viscoelastic material, having $E = 11.5\ GPa$, $G_1 = 1.22\ GPa$, and $\beta = 40\ ms^{-1}$. The large differences in shear relation modulus and decay constant values from the model in [3] and the model from the present work are likely due to the fact that no parameter optimization seems to have been conducted in the former, with its model also being purely viscoelastic, not considering graphite asymmetric tension-compression behavior.

To further demonstrate the effects of the choice in material model, the graphs in Fig. 7.9 were plotted to compare different simulation results with the experimental data, with Fig. 7.9a showing the exact same results as Fig. 7.8 excluding part of the nodes to facilitate visualization, presenting only the ones indicated on the corresponding camera reference frame. Fig. 7.9b and Fig. 7.9c both plot simulation results for purely viscoelastic material models, with the former considering the values for E, G_1, and β reported in [3], and the latter using the values for G_1 and β estimated in this work, as in Table 7.7, and $E = E_t$. Both viscoelastic simulations produce curves simetrically positioned according to the zero abscissa, since, in both cases, the numerical result for node 1 has roughly the same values for maximum and minimum displacements, i.e., $max\{u_{z,1}\} \cong min\{u_{z,1}\}$, within the same cycle, which is also true for all the other nodes. Additionally, unlike the experimental curves, there are no differences between tension and compression in the numerical results, with $max\{u_{z,17}\} - min\{u_{z,1}\} \cong max\{u_{z,1}\} - min\{u_{z,17}\}$ within the same cycle for both viscoelastic models.

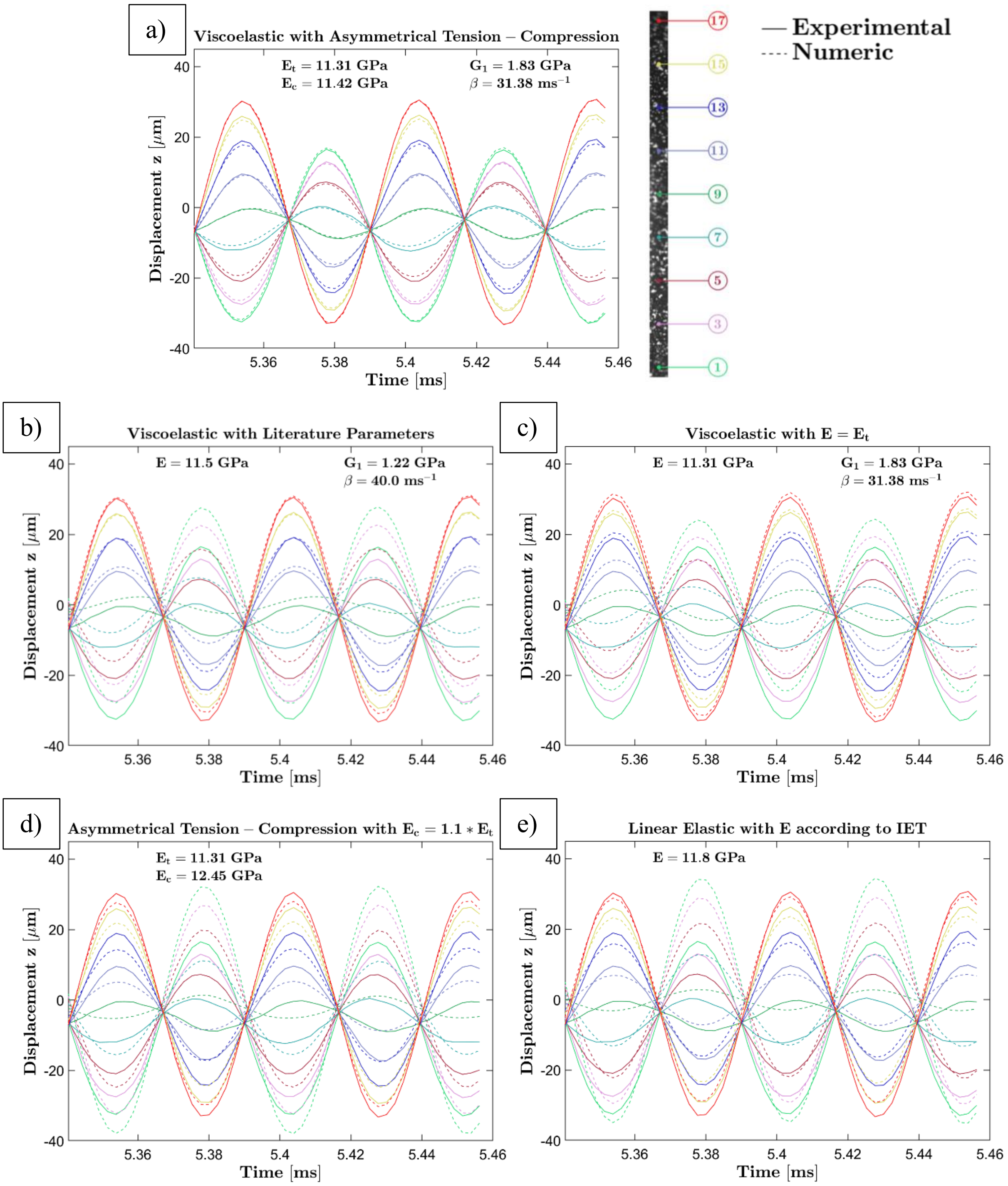

Figure 7.9 Comparison between different material models and the experimental data: (a) the model and parameters obtained in this work, (b) the purely viscoelastic model and parameters from [3], (c) a purely viscoelastic model with parameters obtained in this work, (d) the linear-elastic model with asymmetrical tension-compression considering E_c 10% larger than E_t, and (e) the linear-elastic model using E as calculated through IET.

The main difference between the two sets of parameters for the viscoelastic models is the phases of the curves. The phases in Fig. 7.9c seem to reproduce more accurately those of the experimental curves, which can be observed through node 9, whose numerical curve moves almost parallel to its experimental curve, lacking the downwards shift of the experimental curves identified in all tests, as pointed out in Fig. 7.6a, in Section 7.5. Meanwhile, the phases of the numerical curves in Fig. 7.9b seem to be less coherent with the experimental results, particularly for the nodes with lower amplitudes, such as number 9. These observations suggest the importance of properly estimating the viscoelastic parameters to improve the reproduction of the phases measured experimentally, and confirm that a purely viscoelastic model is not capable of generating the different responses in tension and compression, as well as the downwards shift of the curves.

Finally, Fig. 7.9d and Fig. 7.9e plot the numerical results for linear-elastic models. The former uses the asymmetrical tension-compression model with the tensile elastic modulus E_t estimated in this work, while E_c is recalculated to be 10% larger than E_t, increasing their difference to provide a better understanding of their effects on the results. Meanwhile, Fig. 7.9e uses the elastic modulus measured through IET, as indicated in Table 7.1, Section 7.1. Although the latter creates the condition $f_{n,s} > f_{out}$, where the displacement node is located slightly above node 9, more specifically, between points 9 and 10 from Fig. 7.6b, in Section 7.5, each displacement curve still maintains the symmetry with respect to the zero abscissa as well as the phases behavior, where the nodes located above the displacement node are in counterphase with those located below it.

Similarly, both elastic moduli employed in Fig. 7.9d would individually cause the condition $f_{n,s} > f_{out}$, also causing the displacement node to be above node 9, with the curves 9 and 11 being the ones with lowest amplitudes. Accordingly, nodes 1 to 9 are in counterphase with nodes 11 to 17. However, the curves display the same tendency of being shifted downwards with the increasing amplitude of the displacement on the horn-specimen interface, with the axis of symmetry shifting from 0, at the start of the simulation, to around $-3\ \mu m$ for the time range plotted in Fig. 7.9d. Additionally, it is observed that $max\{u_{z,17}\} - min\{u_{z,1}\} > max\{u_{z,1}\} - min\{u_{z,17}\}$ within the same cycle, however the inequality is almost imperceptible in the graph, since the quantity on the left is only larger by around 4 μm for the plotted cycles.

The observations on Fig. 7.9 confirm that the behavior of the phases observed in the experimental results can be properly simulated by using appropriate values for the viscoelastic parameters. However, it is necessary to add a small level of tension-compression asymmetry between the elastic moduli to achieve the measured shift in axis of symmetry as well as the difference in displacements observed in tension and compression. At the same time, the effects of E_c and E_t on the simulation of Fig. 7.9d are not as pronounced as in the experimental results despite the 10% imposed difference in their values, which suggests that the combination of hysteresis, creep, and dynamic relaxation caused by viscoelasticity greatly accentuate their effects. Indeed, despite the difference between the optimized values of E_c and E_t being only 1%, it is enough to reproduce the large experimental differences between the tension and compression stages of the cycles, while also increasing the downwards shift of the curves.

A plausible explanation for the small change in elastic moduli could be the presence of pores inside the material, which are likely filled with gas, according to the internal defect characterization in Section 7.3. The gas trapped within them during the isostatic pressing of graphite could pose an additional resistance to material deformation during compression, explaining the slightly larger value for E_c.

As for the observed drastic changes caused in the numerical results by increasing E_c in just 1%, i.e., from Fig. 7.9c to Fig. 7.9a, it is likely due to the sudden change in the longitudinal natural frequency of the specimen, corresponding to a sudden increase or decrease in $f_{n,s}$ of around $100\ Hz$ when the load goes from tension to compression, and vice-versa, respectively. Although Fig. 7.9d undergoes a considerably larger variation in $f_{n,s}$, of around $1100\ Hz$, it is possible that the application of Hooke's law in linear-elasticity causes the strain response to be less influenced by these differences in elastic modulus and natural frequency for tension and compression, instead being governed by the inertia of the FEM nodes that are already in resonance.

However, when viscous effects are added to the simulation, the movement of the nodes is severely damped by the time-dependent strain response, broadly observed as a lag between input (the load caused by resonance) and output (the nodes displacements). Since the influence of the inertia from Hooke's law is now undermined by viscosity, the continuous increase and decrease of $f_{n,s}$ plays a considerably larger role in the numerical response. Indeed, the stiffness matrix for a viscoelastic material is dependent on the strain rate, which, in the UST test's case, is dependent on the natural frequency due to the exploitation of the resonance condition. Hence the importance of considering slightly different values for E_t and E_c during this numerical simulation to reproduce the experimental displacements, despite it likely being unnecessary during most structural simulations, especially considering quasi-static conditions.

The determined material properties reported in Table 7.7 allow the calculation and extraction of results for each specimen, which are presented in Table 7.8. The determination coefficients were calculated from the experimental and numerical displacement curves for the laser and the tracker points, excluding points 6 to 10, as it was done for the objectives. Furthermore, each specimen factor α value is listed, all being within the range $[0.79, 0.89]$. The resulting maximum amplitude achieved by the boundary motion curve, corresponding to the amplitude effectively delivered to the specimen was also calculated from the optimized α, being symmetrical to the abscissa axis.

Table 7.8 Results for each graphite specimen extracted from the optimized FEM.

Specimen	Average R^2	Factor α	Achieved amplitude A_{out} $[\mu m]$	σ_f $[MPa]$	σ_f/σ_{max}
1	0.937	0.84	32.7	50.5	1.00
2	0.984	0.82	42.5	51.3	0.86
3	0.984	0.87	37.4	52.6	0.91
4	0.988	0.84	42.4	56.0	0.94
5	0.978	0.79	42.7	55.0	0.91
6	0.994	0.89	38.2	48.8	0.91
7	0.994	0.87	36.7	47.2	0.91
8	0.968	0.77	39.1	50.2	0.91
9	0.988	0.86	42.3	59.6	1.00
10	0.990	0.88	39.7	55.8	1.00
11	0.995	0.89	37.8	51.1	0.96
12	0.993	0.85	36.2	50.9	1.00
13	0.986	0.84	43.5	57.7	0.94
14	0.985	0.86	35.3	45.3	0.91
15	0.992	0.84	38.0	48.7	0.91
16	0.995	0.85	39.0	50.2	0.91

Finally, Table 7.8 also reports the fracture strength, i.e., the maximum nominal tensile strength identified in correspondence to the critical defect position, accompanied by its ratio to the maximum tensile strength globally achieved on the specimen, defined as σ_f/σ_{max}. In this case, the lowest ratio was 0.86, a result in agreement with the absence of severe defects, such as cracks and inclusions, as those identified in alumina 99.5%. Since graphite defects, as presented in Section 7.3, are comprised of porosities, it stands to reason that the variability in the results is considerably smaller than that of alumina. Indeed, the graphite specimens showed a mean strength of $51.9\ MPa$ with a standard deviation of $3.8\ MPa$.

To validate the obtained values of strength, they were compared to experimental values for 4-point bending on graphite R4550 bars conducted in [9], which considered rectangular cross-section bars of $5\ mm$ height, $10\ mm$ width, and $25\ mm$ length, with the test having a $20\ mm$ span between supports, and a $10\ mm$ load span. The mean fracture strengths for both tests, corresponding to 4-point bending ultimate strength and UST fracture strength σ_f, is presented. Table 7.9 also reports their respective risk-volumes considering the material being submitted to at least 90% of the maximum strength, as defined in [10], and the equivalent for 86%, being the minimum ratio σ_f/σ_{max} value obtained in the ultrasonic tests, according to Table 7.8.

Table 7.9 Comparison of strength data and risk-volumes for graphite submitted to UST test and 4-point bending.

Test configuration	Mean strength $[MPa]$	Risk-volume at $0.9 \cdot \sigma_{max}\ [mm^3]$	Risk-volume at $0.86 \cdot \sigma_{max}\ [mm^3]$
UST	51.9	99.8	101.0
4-point bending	61.2	26.3	37.6

The results in Table 7.9 indicate that the strength values obtained through the UST test can be validated. Indeed, the differences with respect to the experimental data from 4-point bending can be attributed to size effect, as detailed in Section 1.2, since the risk-volume is considerably larger in the ultrasonic test, even when the hourglass geometry is employed, which results in the lowest risk-volumes amongst the usual specimen geometries for ultrasonic tests [11]. Furthermore, the difference in testing configuration also affects the measured strength, often requiring more complex size effect models to properly evaluate it, such as the one in [12], which considers the stress distribution inside the specimen rather than only the critical defect size.

7.8. Stress Intensity Factors

Applying the SIF calculation methodology presented in Section 3.3, graphite specimens critical defect sizes were also correlated to their respective fracture strengths. Through Eq. 3.3, $\sigma_f\sqrt{\sqrt{A_c}}$ is again treated as a function of $\sqrt{A_c}/\emptyset$. However, given the hourglass geometry, $\emptyset$ indicates the diameter of the cross-section where the defect is located, at the specimen center being $\emptyset = 5\ mm$. The plot of $\sigma_f\sqrt{\sqrt{A_c}}$ in function of $\sqrt{A_c}/\emptyset$ is shown in Fig. 7.10a, with the fitting curve corresponding to $1/Y$. Once the values for $K_{I,d}$, following Eq. 3.2, are empirically calculated, Fig. 7.10b is obtained, with the SIF values that tend to be constant with the critical defect size, with $C = 0.436\ MPa \cdot m^{1/2}$.

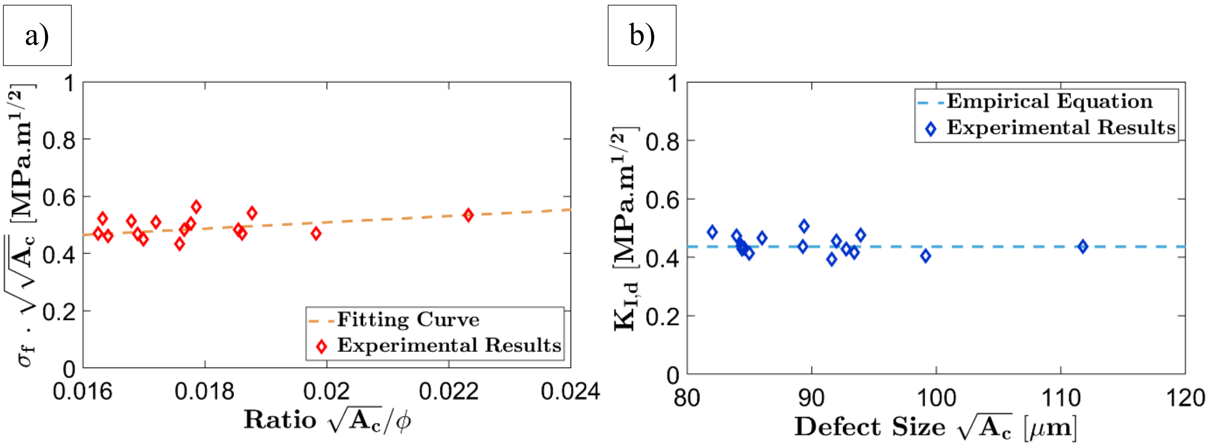

Figure 7.10 Graphical representation of correlation between σ_f and $\sqrt{A_c}$ for graphite, being (a) the raw data and the respective fitting, and (b) applied to the empirical formulation for the SIFs.

The empirical formulation for graphite specimens, resulting in Fig. 7.10b, is as follows:

$$K_{I,d} = 0.436 \cdot \frac{1}{11.0 \cdot \frac{\sqrt{A_c}}{\emptyset} + 0.289} \cdot \sigma_f\sqrt{\sqrt{A_c}} \qquad (7.3)$$

Contrary to alumina’s case, graphite specimens lower variability both in strength values and defect size allowed the use of the full set to calculate C, since they all respect Murakami conditions [13]. Moreover, the empirical fitting of $1/Y$ results in a linear equation instead of an exponential with two terms.

The entire set of graphite specimens, after applied to Eq. 7.3, resulted in a mean SIF of $0.443\, MPa \cdot m^{1/2}$, with a standard deviation of $0.032\, MPa \cdot m^{1/2}$. Like in the case of alumina, the obtained values of SIF, although calculated using the critical defect size, do not correspond to the fracture toughness K_{Ic}. Rather, the values calculated by this methodology relate fracture strength to defect size through an empirical formulation. This means that, if the data provided by this research should be used for component design, the obtained empirical formulation of $K_{I,d}$ should be applied along the calculated SIF values for the critical defects, as well as the fracture strength information, since Eq. 7.3 is not guaranteed to be applicable to all types of experimental data.

The SIFs of defects other than the critical were also calculated through Eq. 7.3. Specifically, the 400 largest defects of each specimen were applied to this analysis, whose objective is to evaluate if the maximum $K_{I,d}$ value achieved on each defect up to the failure moment. However, since graphite behaves nonlinearly, the phase variation created by viscoelasticity makes so that the local stresses are not necessarily at their maximum value at the moment when failure happens. Therefore, to calculate the $K_{I,d}$ values, the maximum nominal tensile stress produced on the respective defect location during the entirety of the test is extracted from the optimized numerical simulation, instead of considering only the one at failure, as in alumina's case.

The graphics resulting from this analysis are reported in Fig. 7.11, referring to each tested specimen, with their respective values concerning the critical defect plotted in red. Theoretically, the critical defect should produce the largest $K_{I,d}$ in each situation, which is not the case. For instance, specimen 2, showed a SIF value 14.3% larger than the one calculated on its critical defect, corresponding to the largest error, while specimen 10 presented the smallest error, at 0.3%.

On one hand, the results observed in Fig. 7.11 produce similar error values to those calculated for the alumina specimens that only presented pores as defects, giving evidence of the systematic execution of this research procedure. On the other hand, it also suggests the influence of factors other than defect size, such as shape, distance to the material surface and relative to other defects, and distribution within the specimen, whose addition to the formulation in Eq. 7.3 might not be possible or too complex to be applied to components design.

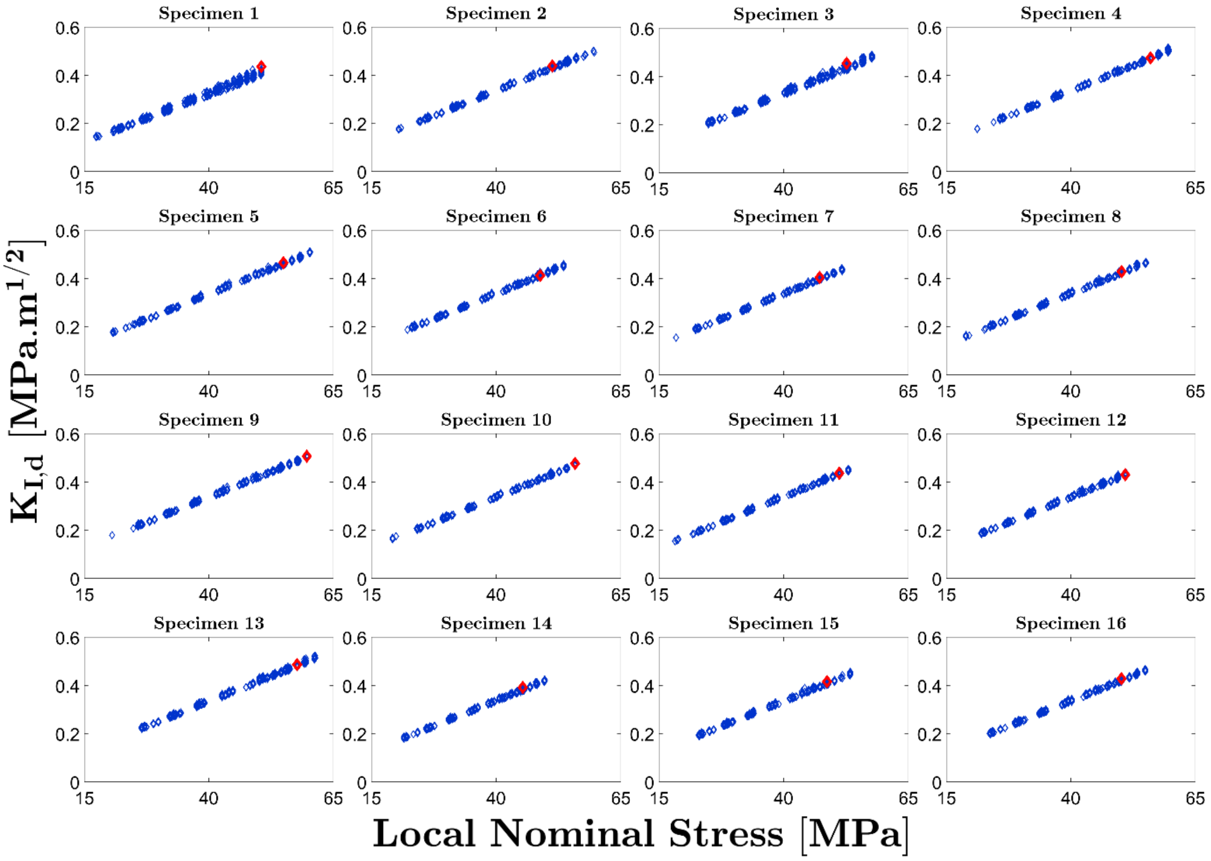

Figure 7.11 SIF at fracture on each graphite specimen 400 largest identified defects, highlighting the critical defect for each specimen in red.

7.9. References

[1] B. März *et al.*, “Mesoscopic structure features in synthetic graphite,” *Mater. Des.*, vol. 142, pp. 268–278, Mar. 2018, doi: 10.1016/j.matdes.2018.01.038.

[2] A. Karvatskii, S. Leleka, A. Pedchenko, and T. Lazarev, “Investigation of the current state of isostatic graphite production technology,” *Mater. Sci.*, vol. 2, no. 1(34), pp. 16–21, 2017, doi: 10.15587/2312-8372.2017.98125.

[3] L. Peroni, M. Scapin, F. Carra, and N. Mariani, “Investigation of dynamic fracture behavior of graphite,” *Key Eng. Mater.*, 2013, doi: 10.4028/www.scientific.net/KEM.569-570.103.

[4] L. R. Herrmann and F. E. Peterson, “A Numerical Procedure for Viscoelastic Stress Analysis,” in *ICRPG Mechanical Behavior Working Group*, 1968.

[5] P. Jaszak, “Modeling of the elastic properties of compressed expanded graphite - A material used in spiral wound gaskets,” *Int. J. Press. Vessel. Pip.*, vol. 187, Nov. 2020,

doi: 10.1016/j.ijpvp.2020.104158.

[6] M. Redzematovic and K. Kirane, “Homogenization of the Mooney-Rivlin coefficients of graphene-based soft sandwich nanocomposites,” *Mech. Soft Mater.*, vol. 3, no. 1, Dec. 2021, doi: 10.1007/s42558-021-00036-9.

[7] R. Ghaffari and R. A. Sauer, “A new efficient hyperelastic finite element model for graphene and its application to carbon nanotubes and nanocones,” *Finite Elem. Anal. Des.*, vol. 146, Jul. 2018, doi: 10.1016/j.finel.2018.04.001.

[8] R.W. Ogden, *Non-Linear Elastic Deformations*. Mineola, New York, USA: Ellis Horwood Ltd, 1984. doi: doi.org/10.1002/zamm.19850650903.

[9] J. Guardia Valenzuela, “Optimisation graphite-matrix composites for collimators in the LHC upgrade,” Universidad Zaragoza, 2019.

[10] A. Tridello, D. S. Paolino, and M. Rossetto, “Ultrasonic VHCF tests on very large specimens with risk-volume up to 5000 mm^3,” *Appl. Sci.*, vol. 10, no. 7, Apr. 2020, doi: 10.3390/app10072210.

[11] A. Tridello, “A novel experimental approach for the assessment of size effect in VHCF,” Politecnico Di Torino, Torino, TO, Italy, 2016.

[12] A. P. Pagnoncelli, A. Tridello, and D. S. Paolino, “Static strength of brittle materials under multiaxial nonuniform stress states: A novel statistical model for assessing size effects,” *Fatigue Fract. Eng. Mater. Struct.*, vol. 44, no. 4, pp. 997–1013, Apr. 2021, doi: 10.1111/ffe.13409.

[13] Y. Murakami, *Theory of elasticity and stress concentration*. 2016. doi: 10.1002/9781119274063.

Chapter 8

8. Final Considerations

In this chapter, a summary of the knowledge provided by this research is presented, consisting of a section identifying the potential sources of error, as well as the actions taken to minimize or avoid them, a section summarizing the conclusions brought by this work, and, finally, a section about potential future research projects.

8.1. Measures to Increase Reliability of Results

To concisely convey all the critical points of the research procedure described in this thesis, Table 8.1 was compiled, summarizing the most important sources of error in the experimental and numerical procedures, as well as the measures adopted to reduce their effect, increasing the reliability of the results. The mentioned points are separated among the three major described procedures, i.e., the micro-CT scans, the UST test, and FE modeling.

Table 8.1 Potential sources of error and measures taken to address them.

Source of errors	Measures to minimize or avoid it
Micro-CT defect analysis	

Scanning artifacts that could be mistaken as defects (either voids or inclusions). They are usually caused by the following: • presence of "dead pixels" (pixels that have stopped working) on the detector; • contrast variation between object and background among the different projections, caused by the object's geometry, positioning, and material characteristics; • improper choice of scanning parameters, e.g., power, filter, number of projections.	Following general guidelines to decrease the number of artifacts, e.g.: • conducting periodical dead pixel calibration on the detector, eventually replacing the detector when necessary; • finding out through initial test-runs the most effective way to place the object on the stage according to its geometry (centering it on the stage's axis of rotation, slightly tilting the object, etc.), as well as determining the most effective scanning parameters; • increasing the scanning resolution since the magnitude of most errors is that of the resolution; • using VGSTUDIO's artifact filters when necessary, i.e., for the situations in which artifacts cannot be avoided.
Improper spatial orientation of the scanned object in VGSTUDIO, which alters all defect analysis results related to positions and projected areas.	Use of a known geometrical element to improve the orientation of the scanned object according to the chosen global coordinate system, e.g., importing the 3D specimen geometry drawn on CAD into VGSTUDIO and using it as reference to position the scanned specimen.
Low sharpness in the reconstruction, which reduces the reliability of the identified defect contours, affecting their calculated sizes.	Reducing the contrast between object and background in the raw projections, often accomplished by simultaneously increasing the x-ray power and the filter capacity. Avoiding filters for noise reduction in VGSTUDIO.
Excessive noise in the reconstruction, which could cause the erroneous identification of noisy areas as defects. However, this source of error is considered less critical to the results than low sharpness, since noise mistakenly identified as defects have very	Increasing the contrast between object and background in the raw projections, often accomplished by simultaneously decreasing the x-ray power and the filter capacity. Only applying filters for noise reduction inside the defect analysis module,

small size, with a magnitude closer to that of the resolution. Meanwhile, the loss of sharpness translates into a loss of accuracy in the measurement of the largest defects.	preferably the median filtering option, to avoid loss of sharpness.
UST test	
Since the entire data acquisition process relies on proper generation and transmission of a trigger signal, hardware malfunctions will cause all data on that specimen to be lost.	Conduction of a test-run before the tests to ensure proper hardware functioning, including the main computer, controlling software, and acquisition devices.
Low acquisition rate of the measuring equipment could cause inaccuracies concerning the displacements amplitudes, since low number of datapoints per cycle are not guaranteed to capture their peaks and valleys.	While the laser and the DAQ system are set to their respective maximum acquisition rates, corresponding to around 20 and around 100 datapoints per cycle respectively, the camera needs to find a compromise between frame rate and resolution, being set at around 22 frames per cycle with resolution of 24 x 512 pixels.
The quality of the spray-painting products and the markings on the specimen surface greatly affect the tracking analysis results. Markings might be poorly distributed on certain regions, as a lack of marks prevents the displacements calculation, while excess of paint covering the specimen can prevent the proper assessment of the studied material displacements. The markings also could get detached from the surface due to the vibrations caused by the test.	The following points should be carefully observed: • proper cleaning of the surface before spraying; • uniform spraying of the specimen, avoiding large portions of surface with both lack or excess of paint; • observation of the sprayed surface with the camera to verify its uniformity before attaching the specimen to the machine; • eliminating from the tracking analysis the zones where paint markings were detached during the test, as well as any zone showing unreasonable results.
Specimens with curved surfaces prevent proper camera focus, such as for the	The results on the graphite specimens were improved by prioritizing camera focus on

graphite specimens used in this work, whose hourglass curvature provides variable specimen surface distance from the camera, not allowing the entire recorded zone to be on focus.	the zones with larger displacement amplitudes, corresponding to those more critical to the material parameter optimization. Uniformity of spray markings was carefully observed to improve the accuracy of even the zones of lower focus quality. For future tests, flat specimen designs should be prioritized whenever an hourglass profile is required. Constant cross-section specimens are allowed to have a circular cross-section, provided its radius is large enough so the recorded area is approximately flat, such was the case for the alumina specimens.
Specimens can present multiple fracture surfaces, such as most of the alumina specimens in this work, preventing the accurate identification of the first fracture surface and, hence, the critical defect and the fracture strength.	The adopted solution was to employ a second high-speed camera, capable of recording at least one frame per cycle, which was shown to be enough to identify in which order the fracture surfaces appeared.
Numerical modeling	
Identification of the material model best suited for the numerical simulation of the tested specimens could potentially be inaccurate while still accurately reproducing the experimental displacements. While the displacements and strains would still be properly calculated by the model, the resulting material properties and stresses would be unreliable.	Thoroughly researching the literature for possible explanations for the tested material behavior, properly justifying the potential choice in material model. Conducting simulations before optimization to select potential candidates for material models, always prioritizing the simpler models, e.g., linear-elastic, purely viscoelastic, etc. Increasing the complexity

	of the model only after ascertaining that optimization cannot find proper parameter values for the simpler models.

8.2. Conclusions

The goal of this research was to establish a new experimental and numerical procedure to collect experimental data on brittle materials that could avoid the shortcomings and difficulties usually encountered in traditional test methods. The described methodology was successfully performed on two materials – alumina 99.5% and graphite R4550 –, being subdivided into three major areas: defect characterization through micro-computed tomography (micro-CT), measurement of uniaxial experimental behavior through ultrasonic tensile (UST) testing, and estimation of mechanical properties through finite element (FE) modeling and optimization.

The analysis of the micro-CT scans provided experimental information on the population of internal flaws contained in the interest volume of each specimen before conducting the destructive test, e.g., their size, location, and probable origin. A method to identify the critical defect of each specimen was devised, consisting of scanning the fracture surfaces and their surroundings after the destructive test to select the largest defect located on the fracture zone. The devised method was proven to be applicable even when the fracture surfaces are missing fragments due to brittle materials catastrophic failure.

The critical defect sizes are ultimately correlated to the uniaxial fracture strengths allowing the estimation of a stress intensity factor (SIF) empirical formulation for each respective material. Although these formulations provide a quantification for the relationship between global strength and defect size, they are only valid for components design if employed alongside the SIF values and the fracture strengths obtained in this work, since they do not correspond to the values of fracture toughness usually contained in the literature or suppliers catalogs.

The proposed SIF formulations also represent an alternative to the often-applied size effect models, which solely rely on the statistical analysis of mechanical strength measured by varying risk-volumes of material. Moreover, while the UST test allows larger risk-volumes than those found in the literature for brittle materials, larger specimens require significantly more time for defect analysis, since multiple micro-CT scans and reconstructions are needed to maintain a good resolution. In contrast, defect analysis on a larger material volume also provides more information on the mechanisms causing these imperfections, potentially contributing to improving fabrication processes.

The defect analysis on alumina specimens showed a large variety of imperfection types, e.g., pores, cracks, and an inclusion, which greatly affected the UST results, with the highest estimated fracture strength value being four times larger than the lowest one. However, this also allowed the evaluation of the global resistance considering different circumstances. In future tests, more alumina specimens should be employed to increase the probability of collecting data on multiple critical defects from each category.

The defect analysis on graphite showed only one type of imperfection, being the pores, which also produced fracture strength results comprised into a narrower range, with the highest fracture strength value being 32% larger than the lowest one. On one hand, this increases the reliability of the calculated fracture strength values, on the other, it does not provide information on imperfections that are not pores. Therefore, in future tests, the risk-volume should be increased, to allow a more thorough investigation of the existence of other types of imperfections.

The SIF formulation for alumina was verified through its application on the 400 largest defects identified on each specimen, with the critical defect always generating a SIF value amongst the largest values achieved on that specimen. Although this formulation was more complex than that of graphite, it can potentially accommodate a larger variety of imperfections, since it was empirically obtained through the correlation between three types of imperfections and a wide range of fracture strengths. However, the small number of samples for each category of imperfection could decrease its efficiency.

The SIF formulation for graphite is considerably simpler, given the low variety of identified defects, being also able to adequately correlate the defects sizes with the local nominal stress, as verified by its application to the 400 largest defects encountered on each specimen, all of which had the critical defect SIF value among the highest. However, since this formulation was empirically obtained considering one type of defect (pores), it might not be applicable to other kinds of imperfections, such as cracks and inclusions, although it will likely show higher reliability for predicting pores effects on fracture strength than the alumina formulation, given the larger number of samples for this type of imperfection.

The second major area of this research was the novel ultrasonic tensile test designed as an alternative method to estimate the quasi-static tensile strength of brittle materials, eliminating, or mitigating, issues commonly found in traditional test methods. The UST test relies on the application of a longitudinal vibration close to the natural frequency of the specimen, causing a resonance condition that generates the uniaxial stress required for failure. In this configuration, only one end of the specimen is attached to the machine with a butt-joint adhesive and the other is free, avoiding both the possibility of failures on the interface with mechanical grips, and the introduction of spurious bending stresses caused even by slight machine misalignments. Meanwhile, the generation of a uniaxial stress field eliminates the need for indirect estimation of the tensile strength from a multiaxial stress state. Finally, since the operating limit of the ultrasonic device is determined by ranges of frequencies and amplitudes, it allows testing of high-resistance brittle materials with considerably larger risk-volumes than those found in the literature, such was the case for alumina, provided the specimen geometry allows the resonance condition to generate the necessary strains to cause failure.

The configuration of the test control and data acquisition was proven to be reliable, with only one sample discarded once the final configuration was established, having a total of 26 samples whose tests were considered valid, between graphite and alumina specimens. The UST test data analysis procedure was proven to be reliable and repeatable among different specimens and materials, estimating the number of cycles and performing the synchronization between different measurement devices.

Two devices were employed to measure the displacements of different points of the specimen during the UST test: a laser and a high-speed camera. The laser measures the uniaxial displacements at the specimen free extremity, also serving the purpose of identifying specimen failure. The camera is required to operate at very high acquisition speed, which reduces the size of the recording window, hence not allowing accurate strain analysis through digital image correlation. However, tracking analysis of the frames was consistently carried out among the different specimens, providing additional experimental displacement curves, required for accurate assessment of the material behavior, especially concerning the nonlinearities of graphite.

Additionally, a third type of measuring device, being the strain gauges on the horn, was employed to estimate the boundary conditions applied to the specimen, consisting of the so-called boundary motion curve. Although the strain gauges were not able to accurately measure the strains generated during the ramp, they were useful to reproduce the ramp envelope, as well as the frequency output of the testing machine, providing the necessary boundary conditions for the FE model of the test. Therefore, during the numerical model optimization, a factor multiplying the boundary motion curve was introduced and estimated, properly adjusting the magnitudes of the displacements. This, however, does not invalidate the possibility of implementing another measuring device in the future to directly detect the displacements on the specimen near the interface with the horn, eliminating one variable from the optimization process, since the boundary motion curve would already correspond to the real magnitudes of the movement delivered to the specimen.

As a consequence of the ultrasonic testing machine operating characteristics, some materials require specimens with complex geometries to be designed, e.g., hourglass, which can substantially increase their cost, especially concerning advanced ceramics that would need to be machined to achieve this geometry. However, many materials were shown to be capable of reaching their ultimate strength within the ultrasonic machine output range through constant cross-section specimens, such as alumina and silicon carbide, often available in suppliers catalogs in the form of bars and rods of variable length. Meanwhile, other brittle materials can be manufactured at low costs in the desired geometry through additive manufacturing, while a few of them are easily machinable, like isostatically pressed graphites.

Fatigue damage caused by the UST test can be discarded after several experimental evidence. Firstly, the number of cycles from each test, for both graphite and alumina, was below the minimum necessary number to achieve regime condition, which should be around 200 cycles, being very low numbers when referring to fatigue tests. Moreover, since these cycles start being counted around the start of the ramp, a lot of them correspond to low stress levels applied to the specimen, being less likely to cause fatigue damage. Finally, two verifications of defect propagation were conducted: the field electron scanning microscope search for fatigue signs on graphite specimens fracture surfaces, and the comparison between alumina non-critical defects in the fracture surfaces vicinities before and after the destructive test. Both experimental observations supported the absence of fatigue damage, given the absence of defects propagation.

The ultrasonic tensile test was successful in its goal of acquiring data on tensile strength data, with the studied materials being confirmed to have been submitted only to uniaxial loads, and all tested specimens failing under tensile loads. Moreover, the absence of fatigue damage is an indication that the estimated values of tensile strength are comparable to values that would be measured in quasi-static uniaxial tensile tests with the same risk-volume of material. These two observations support the claim that the name “ultrasonic tensile test” was properly attributed.

The third and last major area of this work was numerical modeling, consisting of a FE model of the conducted tests, simulating the specimen geometry and boundary conditions, whose goal is to reproduce the measured experimental displacement curves by varying material property values through an optimization process. This method allows the assessment of material behavior, that includes the numerical material model, uniaxial mechanical properties pertaining to the model, and estimation of the uniaxial strength of each tested specimen. Moreover, it also allows the optimization of the multiplying factor of the boundary motion curve, incorporating the difference in magnitude between the theoretical machine output and the movement being delivered to the specimen.

The choice of linear-elastic material model to simulate alumina was proven accurate, with the parameter optimization estimating an elastic modulus within the expected. Although very simple, requiring the optimization of only one property, the application of this material model was shown to reproduce the experimentally measured displacements with high accuracy. Meanwhile, the calculated fracture strength data is considerably smaller than that provided by the supplier. Nevertheless, the large difference in their respective considered risk-volumes, can potentially cause this disparity in strength, according to literature information on size effect.

In contrast to alumina, the graphite material model needed to be more complex to reproduce the asymmetrical tension-compression and the viscoelastic behavior, requiring the optimization of four properties. Nevertheless, it estimated values within the expected range for the tension and compression elastic moduli, considering the impulse excitation technique measurements and literature values for R4550. Although the difference between the two estimated elastic moduli is very small, at only 1%, and could be negligible in most simulations, it is required for the simulation of the ultrasonic test, since its combination with the rate-dependency of viscoelasticity is necessary for reproducing the large difference in tensile and compression displacements observed in the experimental resonance condition. Meanwhile, the values obtained for the shear relaxation modulus and the decay constant were verified to better reproduce the experimental displacements phases than non-optimized values found in the literature. However, these values were able to successfully reproduce the material experimental behavior, indicating their reliability for strains up to 1%, while producing narrower fracture strength data range than that of alumina, in line with the lower variation in identified defect sizes.

8.3. Suggestions for Future Research Works

Suggestions for potential research projects following the work developed on this thesis can be divided in three main points:

1. With the research procedure and equipment configuration being well established, new tests and analyses should be conducted on the two materials addressed here, i.e., graphite R4550 and alumina 99.5%, but with different specimen geometries, or even machine output (provided the number of cycles is kept below 200). Adopting different specimen geometries could contribute to the evaluation of datasets of different risk-volumes, allowing statistical evaluation of material size effect on the tensile strength data of the UST test, also potentially providing a correlation between critical defect size and risk-volume. Meanwhile, the changes in machine output could slightly change the shape of the boundary motion curve applied to the specimen, and the resulting measured displacement curves, which would further confirm the obtained material models. Another direct consequence of increasing experimental information on the tested materials is the improved reliability of the SIF formulation, since its empirical nature implies that the larger the dataset the higher its reliability, which includes its capability of properly accounting for all types of internal defects and material geometries.
2. Since it was established that the described procedure can properly characterize two brittle materials that present widely different behaviors, i.e., alumina and graphite, it should be applicable to other materials, such as those whose specimen designs are presented in this work, as well as any other material that shows brittle behavior. The introduction of a new testing methodology can enrich literature information on a wide range of materials whose tensile testing is difficult, also potentially providing data for statistical size effect analysis and SIF formulation, as mentioned in point 1.
3. Considering that many brittle materials are employed in high temperature environments, it would be an interesting route to design modifications to the UST system, for now only applicable to ambient conditions. It would certainly be a challenge considering that a high temperature system would potentially require: a new attachment method of the specimen to the horn, since the adhesive employed here resists only up to 80° C; the design of a heating system; the addition of temperature measuring devices; the addition of a controlled atmosphere system for materials susceptible to oxygen, such

as graphite; the design of a cooling system for the horn, which would otherwise be heated through conduction.